

THÈSE PRÉSENTÉE
POUR OBTENIR LE GRADE DE
DOCTEUR
DE L'UNIVERSITÉ DE BORDEAUX
ECOLE DOCTORALE SCIENCES PHYSIQUES ET DE
L'INGÉNIEUR
LASERS, MATIÈRE, NANOSCIENCES

Par **Maxime Lavaud**

Confined Brownian Motion

Sous la direction de : **Thomas Salez**
Co-directrion : **Yacine Amarouchene**

Soutenue le 25 décembre 2019

Membres du jury :

Mme. Aude ALPHA	Directrice de Recherche	Université	Rapporteur
M. Bernard BETA	Directeur de Recherche	Université	Rapporteur
M. Georges GAMMA	Directeur de Recherche	Université	Président
Mme. Dominique DELTA	Chargée de Recherche	Université	Examinateuse
M. Eric EPSILON	Ingénieur de Recherche	Université	Examinateur
Mme. Jane DOE	Directrice de Recherche	Université	Directrice
Mme. Simone UNTEL	Ingénieure de Recherche	Université	Invitée

Abstract

Lorem ipsum dolor sit amet, consectetuer adipiscing elit. Ut purus elit, vestibulum ut, placerat ac, adipiscing vitae, felis. Curabitur dictum gravida mauris. Nam arcu libero, nonummy eget, consectetuer id, vulputate a, magna. Donec vehicula augue eu neque. Pellentesque habitant morbi tristique senectus et netus et malesuada fames ac turpis egestas. Mauris ut leo. Cras viverra metus rhoncus sem. Nulla et lectus vestibulum urna fringilla ultrices. Phasellus eu tellus sit amet tortor gravida placerat. Integer sapien est, iaculis in, pretium quis, viverra ac, nunc. Praesent eget sem vel leo ultrices bibendum. Aenean faucibus. Morbi dolor nulla, malesuada eu, pulvinar at, mollis ac, nulla. Curabitur auctor semper nulla. Donec varius orci eget risus. Duis nibh mi, congue eu, accumsan eleifend, sagittis quis, diam. Duis eget orci sit amet orci dignissim rutrum.

Table of Contents

Abstract	i
Table of Contents	iii
List of Figures	xii
List of Abbreviations	xii
1 Brownian Motion	1
1.1 The Brownian motion discovery	1
1.2 Einstein's Brownian theory	2
1.3 The Langevin Equation	6
1.4 Numerical simulation of bulk Brownian motion	11
1.4.1 The numerical Langevin Equation	11
1.4.2 Simulating Brownian Motion Using Python	13
1.4.3 Speedup using Cython	16
1.5 Conclusion	17
2 Particle Characterization and Tracking Using Optical Interferences	18
2.1 Introduction	18
2.2 Reflection Interference Contrast Microscopy	18
2.3 Lorenz-Mie theory	21
2.3.1 Hologram dependence on the particle's characteristics	25
2.3.2 Summary on the Lorenz-Mie method	29
2.4 Rayleigh-Sommerfeld back propagation	33
2.4.1 Numerical Rayleigh-Sommerfeld back propagation	34
2.5 The experimental setup	35
2.6 Optical forces	37
2.7 The experimental procedure	40
2.7.1 Recording the holograms	40
2.7.2 Fitting the holograms	41
2.7.3 Radius and optical index characterization	42
2.7.4 Conclusion	44
3 Stochastic Inference of Surface-Induced Effects Using Brownian Motion	45
3.1 Confined Brownian motion theory	45
3.1.1 Gravitational potential	45
3.1.2 Sphere-wall interactions	46
3.1.2.1 Double layer interactions	47

3.1.2.2	van der Waals interactions	52
3.1.2.3	Total potential and equilibrium distribution	53
3.1.3	Local diffusion coefficient	55
3.1.4	Langevin equation for confined Brownian motion	63
3.1.5	Spurious drift	63
3.1.6	Fokker-Plank equation	66
3.1.7	Numerical simulations of confined Brownian motion	69
3.2	Experimental study	73
3.2.1	Equilibrium distribution	75
3.2.2	Mean Square Displacement	77
3.2.3	Non-Gaussian dynamics - displacement distribution	78
3.2.4	Local diffusion coefficient inference	82
3.2.5	Precise potential inference using multi-fitting technique	85
3.2.6	Measuring external forces using the local drifts	86
3.3	Conclusion	88
4	Work in progress and observations	89
4.1	Elastohydrodynamic lift at soft wall	89
4.1.1	PDMS	90
4.1.2	Measuring non-conservative forces	91
4.2	Close wall stuck motion	93
4.3	Direct relative distance measurement using Mie	96
4.4	Long time 4th cumulent	99
4.5	Sample ageing	102
5	Conclusion	104
6	Conclusion en français	105
References		108

List of Figures

Fig. 1.1.1: Brownian motion of $1 \mu\text{m}$ particles in water tracked manually by Jean Perrin and his colleagues. The points are spaced in time by 30 seconds, and 16 divisions represent $50 \mu\text{m}$	2
Fig. 1.2.1: Simulation of over-damped Brownian motion in the bulk (see Eq. (1.4.9)) of $1 \mu\text{m}$ particles in water. On the top each line represents the trajectory of a Brownian particle over 100 seconds. A total of 100 trajectories are shown. On the bottom, bullets represent the Mean Square Displacement (MSD) computed from the simulated trajectories. The plain black line represents Einstein's theory, which is computed from the square of Eq. (1.2.11).	5
Fig. 1.4.1: Bullets represents the probability density function of w_i , a Gaussian-distributed number with a mean value $\langle w_i \rangle$ and a variance $\langle w_i^2 \rangle = \tau$. The plain black line is a Gaussian distribution of zero mean and a τ variance (see Eq. (1.4.3)). On the first line, the simulation is done with $\tau = 10^{-3} \text{ s}$ and $\tau = 1 \text{ s}$ on the second one. Each column corresponds to a number N of draws. From the left to the right: $N = 10^2$, 10^3 and 10^4	11
Fig. 1.4.2: Mean Relative Squared Error (MRSE) of the Probability Density Function PDF measured from a generation of N Gaussian random numbers w_i and the actual Gaussian (see Eq. (1.4.3)) from which the generation is done. The generation is done over a Gaussian which has a mean value $\langle w_i \rangle = 0$ and variance $\langle w_i^2 \rangle = \tau$. We explore parameter ranges from $N = 10$ to 10^7 and $\tau = 10^{-2}$ to 10 s	13
Fig. 1.4.3: a) Set of 100 trajectories simulated using the full-Langevin equation (see Eq. (1.4.5)) for particles of a radius $a = 1 \mu\text{m}$ and mass $m = 10 \mu\text{g}$ in water, with viscosity $\eta = 0.001 \text{ Pa.s}$. The simulations are done with a time step $\tau = 0.01 \text{ s}$. b) Bullets represent the measured Mean Squared Displacements (MSD) of the simulated trajectories. The plain black line represents the characteristic inertial timescale, $\tau_B = m/\gamma = 0.53 \text{ s}$. The dotted line represents the MSD in the ballistic regime (see Eq. (1.3.26)), when $t \ll \tau_B$. The dashed line represents the MSD in the diffusive regime (see Eq. (1.3.27)), when $t \gg \tau_B$, $\text{MSD} = 2D\tau$. A detailed explanation of the simulation process can be found in appendix.??.	16

Fig. 2.2.1: Figure from [21] representing RICM with two wavelengths. (a) Left: interference patterns created with a wavelength $\lambda_1 = 532$ nm (scale bar 5 μm). Right: radial intensity profile (black dots) extracted from the image, azimuthally averaged (magenta line) and fitted with Eq. (2.2.8) to measure the height of the particle (here noted h). (b) Same as (a) with a wavelength $\lambda_2 = 635$ nm. (c) Time series of the height h of a particle (green: λ_1 , purple: λ_2) and the particle velocity measured along the flow (in blue).	19
Fig. 2.3.1: a) Raw hologram of a 2.5 μm polystyrene particle measured experimentally with the setup detailed in the section 2.5. b) Background obtained by taking the median value of an image time series. c) Normalized hologram given by dividing a) by b). d) Result of the fit of c) using Eq. (2.3.4), from which the particle is found to be at a height $z = 14.77$ μm . e) Comparison of the normalized radial intensities, obtained experimentally from c) and theoretically from d).	25
Fig. 2.3.2: Hologram intensity map in the (r, z) -plan, calculated (see. Eq. (2.3.4)) for a particle of radius $a = 1.5$ μm and optical index $n = 1.59$	26
Fig. 2.3.3: Hologram intensity map in the (r, a) -plan, calculated (see. Eq. (2.3.4)) for a particle of optical index $n = 1.59$, and a distance $z = 15$ μm between the particle center and the focal plane of the objective lens.	27
Fig. 2.3.4: Radial intensity profile for particle radius $a \ll \lambda$, and an optical index $n_p = 1.59$ with a distance $z = 15$ μm between the particle center and the focal plane of the objective lens, and for a wavelength $\lambda = 532$ nm.	27
Fig. 2.3.5: Hologram intensity map in the (r, a) -plan, calculated (see. Eq. (2.3.4)) for a particle of optical index $n = 1.59$, and a distance $z = 15$ μm between the particle center and the focal plane of the objective lens.	28
Fig. 2.3.6: Hologram intensity map in the (r, z) -plan, calculated (see. Eq. (2.3.4)) for a particle of optical index $n = 1.59$, and radius $a = 1.51$ μm using the experimental setup presented in the section 2.5. On the right, the corresponding theoretical intensity using the result of each individual hologram's fit to Eq. (2.3.5).	30
Fig. 2.3.7: Holograms calculated (see. Eq. (2.3.4)) for different set of parameters (a, n_p) , and for a distance $z = 15$ μm between the particle center and the focal plane of the objective lens.	31
Fig. 2.3.8: Holograms calculated (see. Eq. (2.3.4)) for different set of parameters (a, z) , and for an optical index $n_p = 1.59$	32

Fig. 2.4.1: On the left: the original hologram on the top and propagated along $15 \mu\text{m}$ on the bottom. On the right: reconstruction using Eq. (2.4.5) of the scattered intensity by a single colloidal sphere of radius $a = 0.1 \mu\text{m}$, with optical index $n_p = 1.59$ in water whose index is $n_m = 1.59$, and for a height of $15 \mu\text{m}$	35
Fig. 2.5.1: Photo of the custom-built microscope developed in my thesis. It is composed of a Thorlabs cage system. The camera used is a Basler acA1920-155um. We use a x60 magnification and 1.30 numerical aperture oil-immersion objective lens. The light source is a collimated 521 nm wavelength laser.	36
Fig. 2.5.2: Schematic of the experimental setup. A laser plane wave of intensity I_0 illuminates the chamber containing a dilute suspension of microspheres in water. The light scattered by a particle interferes with the incident beam onto the focal plane of an objective lens, which magnifies the interference pattern and relays it to a camera.	37
Fig. 2.6.1: Real (left axis) and imaginary (right axis) part of the refractive index of polystyrene as a function of the incident wavelength. Data obtained from [45]	38
Fig. 2.6.2: Optical force F_{opt} (see Eq. (2.6.1)) exerted on a spherical particle of radius a by a plane wave of wavelength $\lambda = 532 \text{ nm}$, and of irradiance $I_r = 467.7 \text{ W.m}^{-2}$. The force is calculated employing the <code>miepython</code> python's module and the refractive index of polystyrene [45].	39
Fig. 2.7.1: 2D Probability density function of the measurements of the optical index n_p and radius a . Black lines indicate iso-probability. Taking the 10% top probability, we measure $n_p = 1.585 \pm 0.002$ and $a = 1.514 \pm 0.003 \mu\text{m}$	43
Fig. 2.7.2: 3D plot of an experimental trajectory measured in water for a particle of optical index $n_p = 1.585$ and radius $a = 1.514 \mu\text{m}$	43
Fig. 3.1.1: Experimental trajectory of a polystyrene particle of radius $a = 1.5 \mu\text{m}$ in water near a glass wall ($z = 0$) along the z -axis — <i>i.e</i> perpendicular to the wall.	45
Fig. 3.1.2: A colloid diffusing near a wall. Both the wall and colloid surfaces charge negatively. As a consequence, a layer of positively-charged ions is attracted towards each surface, forming a double layer.	48
Fig. 3.1.3: A colloid of radius a is located at a distance z from the wall. The dielectric constants of the sphere, wall and liquid are respectively ϵ_1 , ϵ_2 , and ϵ_3	52

Fig. 3.1.4: a) In orange potential energy U_g (see Eq. (3.1.3)) of a colloid with a Boltzmann length $\ell_B = 500$ nm. In blue, the electrostatic potential energy U_{elec} (see Eq. (3.1.22)) is characterized by a dimensionless magnitude $B = 4$ and a Debye length $\ell_D = 50$ nm. The dashed line corresponds to the total potential U , see Eq. (3.1.27). b) Corresponding Gibbs-Boltzmann equilibrium distribution of position calculated using the energy potential of panel a).	55
Fig. 3.1.5: Figure extracted from [52]. On the left is the experimental setup. It is an inverted microscope used in order to track micrometric particles of diameter $2R$ inside a liquid cell of thickness t . On the right is the final result, where the authors measure the diffusion parallel (<i>i.e.</i> along x or y) coefficient D_{\parallel} (see Eqs. (3.1.47) and (3.1.45)), normalized by the bulk diffusion coefficient D_0 , as a function the confinement parameter $\gamma = \langle z \rangle_t / a$, with $\langle z \rangle_t$ time-averaged particle-wall distance.	56
Fig. 3.1.6: Schematic representation of a spherical object of radius a moving towards a wall at velocity V_{sphere} and inducing a fluid velocity V_{fluid}	58
Fig. 3.1.7: a) Parallel and perpendicular normalized diffusion coefficients for a colloidal particle of radius $a = 1.5 \mu\text{m}$. b) Perpendicular normalized diffusion coefficient at a distance z from a wall. The solid black line is the exact solution given by the infinite sum of Eq. (3.1.46). The green dashed line is the Padé approximation of Eq. (3.1.48). The blue dashed line is the near-wall asymptotic expression of Eq. (3.1.49). c) Relative errors between the two approximations (dashed lines of panel b), same color code) and the exact result (solid line of panel b)).	62
Fig. 3.1.8: Theoretical drift velocity for a colloidal particle of radius $a = 1.5 \mu\text{m}$ in water and at a distance z from the wall. The physical parameters $\ell_D = 50$ nm, $B = 4 k_B T$ and $\ell_B = 500$ nm.	66
Fig. 3.1.9: a) Theoretical computation of the relative variation of the drift velocity \bar{v}_d and perpendicular diffusion coefficient D_{\perp} as a function particle-wall distance z . The parameters are $\ell_D = 50$, $B = 4$ and $\ell_B = 500$ nm b) Optimal numerical integration time step τ_{\max} as a function of the particle-wall distance z for a particle of radius $a = 1.5 \mu\text{m}$, with $\ell_B = 500$ nm, $B = 4$, and for different Debye lengths as indicated. The black line connects the minima.	72
Fig. 3.1.10: Simulated trajectory along the direction normal to the wall, using Eq. (3.1.77) with $\alpha = 1$ (isothermal convention), of radius $a = 1.5 \mu\text{m}$, density $\rho_p = 1050 \text{ kg.m}^{-3}$, placed in water near a wall. The particle-wall interaction is characterized by $\ell_D = 50$ nm and $B = 4$	72

Fig. 3.1.11: Simulated, Long-term Probability Density Function of the height of the particle for different convention as indicated. The solid black line represents the expected Gibbs-Boltzmann distribution. The physical parameters are: $a = 1.5 \mu\text{m}$, $\rho_p = 1050 \text{ kg.m}^{-3}$, $\ell_D = 50 \text{ nm}$, $B = 4$ and $\ell_B = 577 \text{ nm}$	74
Fig. 3.2.1: Raw trajectory measured using the Mie tracking technique, and it's rescaled value using moving minimum algorithm with a window of 10000 points.	75
Fig. 3.2.2: Measured equilibrium probability density function P_{eq} of the distance z between the particle and the wall. The solid line represents the best fit to the normalized Gibbs-Boltzmann distribution in position, using the total potential energy $U(z)$ of Eq. (3.1.28), with $B = 4.8$, $\ell_D = 21 \text{ nm}$, and $\ell_B = 530 \text{ nm}$	76
Fig. 3.2.3: In blue, left axis, measured Debye length ℓ_D as a function of salt concentration [NaCl]. The solid line is the expected Debye relation $\ell_D = 0.304/\sqrt{[\text{NaCl}]}$, for a single monovalent salt in water at room temperature. In green, right axis, measured B as a function of salt concentration [NaCl]. The dashed line represents the mean value of the measured B values.	76
Fig. 3.2.4: Measured mean-squared displacements (MSD, see Eq. (3.2.1)) as functions of the time increment Δt , for the three spatial directions, x , y , and z . The solid lines are best fits to Eq. (3.2.2), using Eqs. (3.1.28), (3.1.46) and (3.1.47), with $B = 4.8$, $\ell_D = 21 \text{ nm}$, and $\ell_B = 530 \text{ nm}$, providing the average diffusion coefficients $\langle D_{\parallel} \rangle = \langle D_x \rangle = \langle D_y \rangle = 0.52 D_0$ and $\langle D_z \rangle = 0.24 D_0$. The dashed line is the best fit to Eq. (3.2.9), using Eq. (3.1.28), with $B = 4.8$, $\ell_D = 21 \text{ nm}$, and $\ell_B = 530 \text{ nm}$	78

Fig. 3.2.8: Total normal conservative force F_z exerted on the particle as a function of the distance z to the wall, reconstructed from Eq. (3.2.19), using Eq. (3.1.48) in circles and using Eq. (3.2.18) in squares. The solid line corresponds to Eq. (3.2.21), with $B = 4.8$, $\ell_D = 21 \text{ nm}$ and $\ell_B = 530 \text{ nm}$. The black dashed lines and gray area indicate the amplitude of the thermal noise computed from Eq. (3.2.20). The horizontal red dashed line indicates the buoyant weight $F_g = -7 \text{ fN}$ of the particle.	87
Fig. 4.1.1: Schema of a spherical colloid of radius a immersed in a fluid of viscosity η sliding at a velocity V above an incompressible and linear-elastic substrate of shear elastic modulus G . From the elastohydrodynamic interactions between the particle and the soft wall arises a net lift force F_{lift} (see Eq. (4.1.1)).	89
Fig. 4.1.2: Figure taken from [90]. Examples of crosslinking reaction between the PDMS chains and a curing agent containing hydrosilane groups.	91
Fig. 4.1.3: Non-conservative forces measured experimentally for colloidal particles of radius $a = 1.5 \mu\text{m}$ diffusing above an incompressible and linear-elastic substrate of shear elastic modulus $G = 15$ and 28 kPa . Plain line corresponds to the Brownian model of the EHD lift force $F_{\text{lift},\text{Brown}}$ (see Eq. (4.1.2)) with an added noise-level of 10 fN	92
Fig. 4.1.4: Non-conservative forces normalized $G\sqrt{a}$ by measured experimentally for colloidal particles of radius $a = 1.5 \mu\text{m}$ diffusing above an incompressible and linear-elastic substrate of shear elastic modulus $G = 15$ and 28 kPa . Plain line corresponds to the Brownian model of the EHD lift force $F_{\text{lift},\text{Brown}}$ (see Eq. (4.1.2)) with an added noise-level of 10 fN	93
Fig. 4.2.1: Median image of a stuck particle. The median is calculated over 120 images taken every 30 s.	93
Fig. 4.2.2: Raw trajectory measured using the Mie tracking technique for the x -, y - and z - axis of a particle of radius $a = 1.5 \mu\text{m}$. The time between each frame is $1/200 \text{ s}$	94
Fig. 4.2.3: Measured mean-squared displacements of a stuck particle (MSD, see Eq. (3.2.1)) as functions of the time increment Δt , for the three spatial directions, x , y , and z . The solid line is the best fit to Eq. (3.2.2), having $\langle D_i \rangle$ as a free parameter, providing the average diffusion coefficient $\langle D_{\parallel} \rangle = \langle D_x \rangle = \langle D_y \rangle = 0.14 D_0$. The plain gray line is the average value of the plateau of the MSD along the x - and y -axis, providing $\lim_{\Delta t \rightarrow \infty} \langle \Delta x^2 \rangle = 4.3 \times 10^{-15} \text{ m}^2$	95

Fig. 4.2.4: Normalized probability density functions $P_i \sigma$ of the normalized displacements $\Delta x/\sigma$ and $\Delta z/\sigma$, at short times, with σ^2 the corresponding MSD (see Fig. 4.2.3), for different time increments Δt ranging from 0.01 s to 0.05 s, as indicated with different colors. The gray dashed lines are normalized Gaussian distributions, with zero means and unit variances. .	96
Fig. 4.3.1: Scheme of a particle immersed in a fluid of index n_1 above a glass substrate of optical index n_2 . The particle is at a distance z_w above the glass substrate, and the objective focal plane z_g below the interface. Due to the Snell-Descartes's law, light with an incident angle θ_1 is refracted with an angle β	97
Fig. 4.4.1: Trajectory of 300 particles of commercial radius $a = 2.5 \mu\text{m}$. The trajectories are composed of 10000 points with a time step $\tau = 0.05 \text{ s}$	101
Fig. 4.4.2: Bullets corresponds to the experimentally measured 4th cumulant, see Eq. (4.4.2). The plain line is a linear regime indicator. The images are 45 μm wide and 50 μm tall.	101
Fig. 4.5.1: Image of a particle diffusing above a soft surface ($G = 1.5 \text{ kPa}$). The image on the right has been taken 3 hours after the one on the left. The images are 45 μm wide and 50 μm tall.	102
Fig. 4.5.2: Image of the glass-PDMS ($G = 1.5 \text{ kPa}$) interface, three hours after that water has been introduced in the sample. The images are 45 μm wide and 50 μm tall.	103

List of Abbreviations

fps	Frames per second
MRSE	Mean Relative Squared Error
MSD	Mean Squared Displacement
PDF	Probability Density Function
RICM	Reflection Interference Contrast Microscopy
ROI	Region Of Interest
SDE	Stochastic Differential Equations

1 Brownian Motion

1.1 The Brownian motion discovery

In 1827 the Scottish botanist Robert Brown published an article [1] on his observation on the pollen of *Clarkia pulchella* with a lot of details on his reflection processes. His experiments were made to understand the flower reproduction, but, as he was looking through the microscope he observed some minute particles ejected from the pollen grains. At first, he thought the goal of this agitation was to test the presence of a male organ. To test this theory, he extended his observations to Mosses and *Equiseta*, which were drying for a hundred years. However, the fact that this peculiar motion was still observable made him invalidate his theory. Interestingly, each time that he encountered a material that he could reduce to a fine enough powder to be suspended in water, he observed the same type of motion, although, he never understood its particle's movement.

The difficulty at this time to observe and capture such a movement made the study of what we call contemporarily Brownian motion difficult and the first theoretical work was done by Louis Bachelier in his PhD thesis “The theory of speculation,” where he described a stochastic analysis of the stock and option market. Nowadays, the mathematical description of random movement is still used in the modern financial industry.

It is finally in 1905 that Albert Einstein theoretically state that “bodies of microscopically visible size suspended in a liquid will perform movements of such a magnitude that they can be easily observed in a microscope” [2]. A remark to make here is that in 1948 Einstein wrote a letter to one of his friends where he stated having deduced the Brownian motion “from mechanics, without knowing that anyone had already observed anything of the kind” [3].

It is in 1908 that Jean Perrin published his experimental work on Brownian motion. That way he could measure the Avogadro number and prove the kinetic theory that Einstein developed. I would also cite Chaudesaigues and Dabrowski, who helped Perrin to track the particles manually, half-minutes by half-minutes, for more than 3000 displacements (25 hours) and several particles. This impressive and daunting work is highly detailed in “*Mouvement brownien et molécules*” [4]. This is partly due to the results this work that Perrin received the Nobel award in 1926.

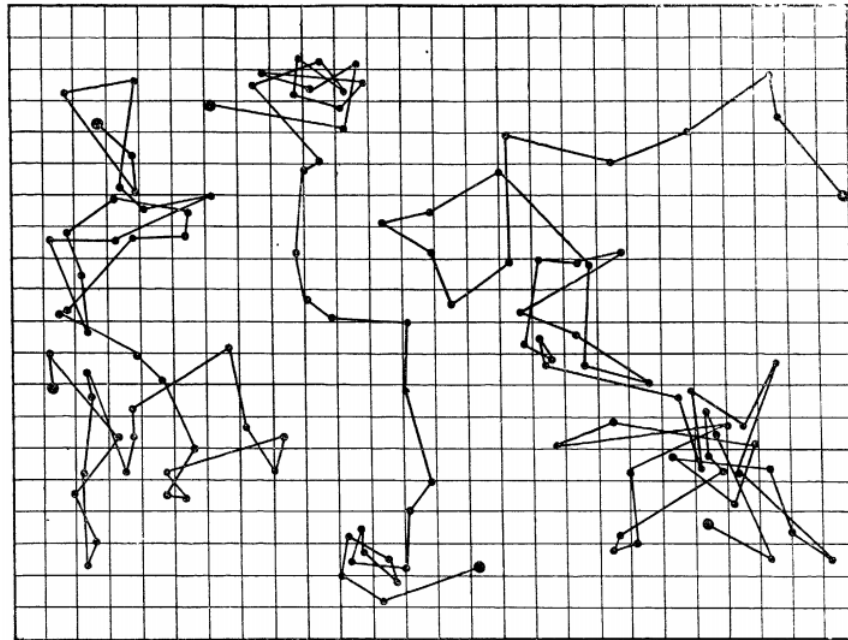


Figure 1.1.1: Brownian motion of $1 \mu\text{m}$ particles in water tracked manually by Jean Perrin and his colleagues. The points are spaced in time by 30 seconds, and 16 divisions represent $50 \mu\text{m}$.

1.2 Einstein's Brownian theory

In this section we will derive the main characteristics of bulk Brownian motion in the manner of Einstein in 1905 by summarizing the section 4 of [2]. We will then examine the random motion of particles suspended in a liquid and its relation to diffusion, caused by thermal molecular motion. We assume that each particle motion is independent of other particles; also the motions of one particle at different times are assumed to be independent of one another provided that the time interval is not too small. Furthermore, we now introduce a time interval τ which is small compared to the observation time but large enough so that the displacements in two consecutive time intervals τ may be taken as independent events.

For simplicity, we will here look only at the Brownian motion of n particles in 1D along the x axis. In a time interval τ the position of each particle will increase by a displacement Δ , positive or negative. The number of particles dn experiencing a displacement lying between Δ and $\Delta + d\Delta$ in a time interval τ is written as:

$$dn = n\varphi(\Delta)d\Delta , \quad (1.2.1)$$

where

$$\int_{-\infty}^{\infty} \varphi(\Delta) d\Delta = 1 , \quad (1.2.2)$$

and φ is the probability distribution of displacement. We assume for now, that φ is a Gaussian distribution, with a variance scaling linearly with τ . Additionally, since such a distribution is even, it satisfies: $\varphi(\Delta) = \varphi(-\Delta)$.

Let $f(x, t)$ be the number of particles per unit volume. From the definition of the function $\varphi(\Delta)$ we can obtain the distribution of particles found at time $t + \tau$ from their distribution at a time t , through:

$$f(x, t + \tau) = \int_{-\infty}^{+\infty} f(x - \Delta, t) \varphi(\Delta) d\Delta . \quad (1.2.3)$$

Since we suppose that τ is very small with respect to t , we have at first order in time:

$$f(x, t + \tau) \simeq f(x, t) + \tau \frac{\partial f}{\partial t} . \quad (1.2.4)$$

Besides, we can Taylor expand $f(x + \Delta, t)$ in powers of Δ since only small values of Δ contribute. We obtain:

$$f(x - \Delta, t) = f(x, t) - \Delta \frac{\partial f(x, t)}{\partial x} + \frac{\Delta^2}{2!} \frac{\partial^2 f(x, t)}{\partial x^2} . \quad (1.2.5)$$

Combining Eqs. 1.2.4, 1.2.5 and 1.2.3 we obtain:

$$f + \frac{\partial f}{\partial t} \tau = f \int_{-\infty}^{+\infty} \varphi(\Delta) d\Delta + \frac{\partial f}{\partial x} \int_{-\infty}^{+\infty} \Delta \varphi(\Delta) d\Delta + \frac{\partial^2 f}{\partial x^2} \int_{-\infty}^{+\infty} \frac{\Delta^2}{2} \varphi(\Delta) d\Delta . \quad (1.2.6)$$

On the right-hand side, since $\varphi(x)$ is an even function, the second term vanishes. Considering Eq. (1.2.2) and invoking the definition:

$$\frac{1}{\tau} \int_{-\infty}^{+\infty} \frac{\Delta^2}{2} \varphi(\Delta) d\Delta = D , \quad (1.2.7)$$

Eq. (1.2.6) finally becomes:

$$\frac{\partial f}{\partial t} = D \frac{\partial^2 f}{\partial x^2}. \quad (1.2.8)$$

We can here recognize a partial equation of diffusion with D the diffusion coefficient. We will now initiate the same position $x = 0$ for all the particles at $t = 0$ as in Fig.1.2.1. $f(x, t)dx$ denotes the number of particles whose positions have increased between the times 0 and t by a quantity lying between x and $x + dx$ such that we must have:

$$f(x \neq 0, t = 0) = 0 \text{ and } \int_{-\infty}^{+\infty} f(x, t)dx = n. \quad (1.2.9)$$

The solution Eq. (1.2.8) is then the Green's function of the heat equation in the bulk:

$$f(x, t) = \frac{1}{\sqrt{4\pi D}} \frac{\exp\left(\frac{-x^2}{4Dt}\right)}{\sqrt{t}}. \quad (1.2.10)$$

From this solution we can see that the mean value of the displacement along the x axis is equal to 0 and the square root of the arithmetic mean of the squares of displacements (that we commonly call the Root Mean Square Displacement (RMSD)) is given by:

$$\lambda_x = \sqrt{\langle \Delta^2 \rangle} = \sqrt{2Dt}. \quad (1.2.11)$$

The mean displacement is thus proportional to the square root of time. This result is generally the first behavior that we check when we study Brownian motion. In 3D, the square root of the MSD is given by $\lambda_x\sqrt{3}$.

Previously in his article [2], Einstein had found by writing the thermodynamic equilibrium of a suspension of particles that the diffusion coefficient of a particle should read:

$$D = \frac{RT}{N_A} \frac{1}{6\pi\eta a} = \frac{k_B T}{6\pi\eta a}, \quad (1.2.12)$$

with R the gas constant, T the temperature, N_A the Avogadro number, η the fluid viscosity and k_B the Boltzmann constant. Thus, an experimental measurement of D could lead to a measurement of the Avogadro number since:

$$N_A = \frac{t}{\lambda_x^2} \frac{RT}{3\pi\eta a} . \quad (1.2.13)$$

Furthermore, measuring N_A also gives us the mass of atoms and molecules since the mass of a mole is known; as an example the mass of an oxygen atom will be given by $\frac{16}{N_A}$ and the mass a water molecule by $\frac{18}{N_A}$. Finally, Einstein ends up in article [2] by writing, “*Let us hope that a researcher will soon succeed in solving the problem posed here, which is of such importance in the theory of heat!*” I would like here to emphasize the importance of solving this problem at the very beginning of the 20th century. At this time two hypotheses about the fundamental matter components existed, one involving energy and a continuum description in terms of field, and the other one, discrete atoms, especially supported by Boltzmann and his kinetic theory of gases, used by Einstein. Due to a lot of conceptual misunderstandings and experimental error scientist such as Svedberg or Henri thought that Einstein’s theory was false [5] by even suggesting that the statistical properties of Brownian motion were changing with the pH of the solution. It is finally in 1908 that Chaudesaigues and Perrin published all the evidence to prove Einstein’s theory mainly by their ability to create particle emulsions of well-controlled radii.

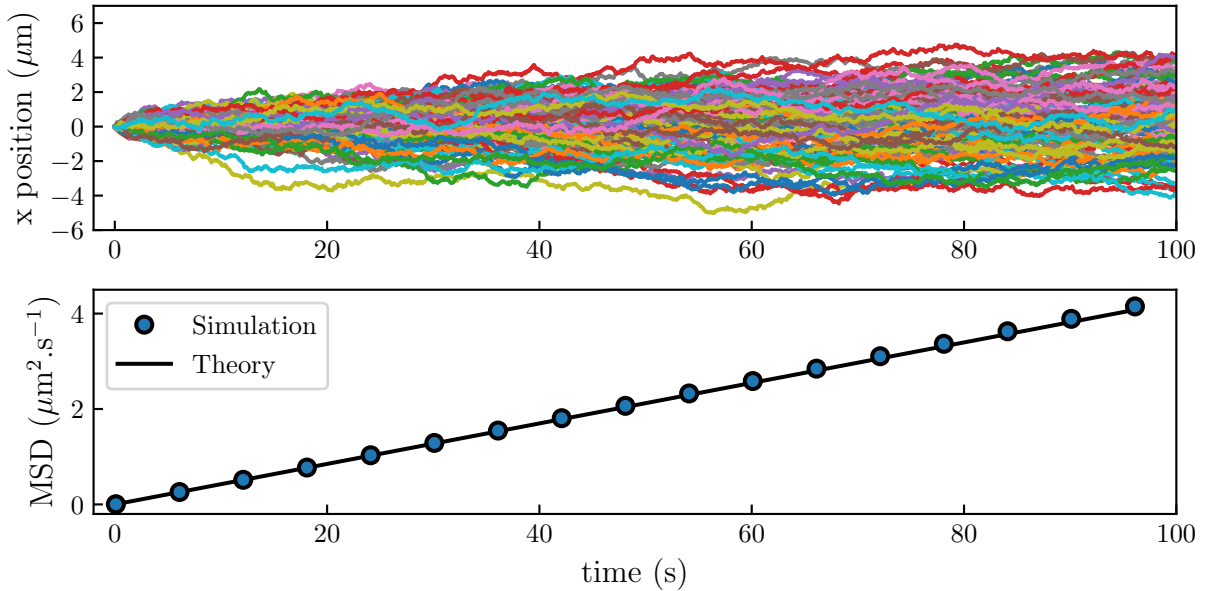


Figure 1.2.1: Simulation of over-damped Brownian motion in the bulk (see Eq. (1.4.9)) of $1 \mu\text{m}$ particles in water. On the top each line represents the trajectory of a Brownian particle over 100 seconds. A total of 100 trajectories are shown. On the bottom, bullets represent the Mean Square Displacement (MSD) computed from the simulated trajectories. The plain black line represents Einstein’s theory, which is computed from the square of Eq. (1.2.11).

1.3 The Langevin Equation

in physics we generally describe Brownian motion through a particular Stochastic Differential Equations (SDE). This model was introduced in 1908 by Langevin [6], this model is now used by the major part of physicists working on random processes. The Langevin equation for a free colloid reads:

$$m dV_t = -\gamma V_t dt + \alpha dB_t , \quad (1.3.1)$$

with m the mass and V_t the velocity of the particle. This SDE is the Newton's second law, relating the particle momentum change on the left-hand side of the equation to forces on the right-hand side. We see that the total force applied on the particle is given by two terms: a friction term, with a Stokes-like fluid friction coefficient γ , a random force with α that we will detail for a spherical particle, dB_t a random noise which has a Gaussian distribution of zero mean thus:

$$\langle dB_t \rangle = 0 , \quad (1.3.2)$$

and variance equal to:

$$\langle dB_t^2 \rangle = dt . \quad (1.3.3)$$

For a spherical particle, the friction term is given by the Stoke's formula: $\gamma = 6\pi\eta a$ with η the fluid viscosity and a the particle radius. Thus, we can derive the mean value of the particle velocity as:

$$\left\langle \frac{dV_t}{dt} \right\rangle = -\frac{\gamma}{m} \langle V_t \rangle dt + \frac{\alpha}{m} \langle dB_t \rangle , \quad (1.3.4)$$

with the properties of dB_t given by Eq. (1.3.2), it becomes:

$$\langle dV_t \rangle = -\frac{\gamma}{m} \langle V_t \rangle dt . \quad (1.3.5)$$

Moreover, without a loss of generality, the average of a variable x , $\langle x \rangle$, is done over a set

of N observations $\{x_i\}$ such as:

$$\langle x \rangle = \frac{1}{N} \sum_{i=1}^N x_i , \quad (1.3.6)$$

one can then show that:

$$\frac{d}{dt} \langle x \rangle = \frac{d}{dt} \left[\frac{1}{N} \sum_{i=1}^N x_i \right] = \frac{1}{N} \sum_{i=1}^N \frac{d}{dt} x_i = \langle \frac{d}{dt} x \rangle . \quad (1.3.7)$$

The latter thus shows that it is possible to invert average value $\langle \cdot \rangle$ and a derivative. Therefore, Eq. (1.3.5) becomes:

$$\frac{d}{dt} \langle V_t \rangle = -\frac{\gamma}{m} \langle V_t \rangle , \quad (1.3.8)$$

which has a familiar solution:

$$\langle V_t(t) \rangle = V_0 e^{-\frac{\gamma}{m} t} , \quad (1.3.9)$$

with V_0 an initial velocity. This result shows that the average of the velocity should decay to zero with a characteristic time $\tau_B = \frac{m}{\gamma}$. For instance, the polystyrene particles used during my experiments which are micrometric we have $\tau_B \approx 10^{-7}$ s. This signifies that if we measure the displacements of a particle with a time interval $\tau \gg \tau_B$ the displacement can be taken as independent events as it was stated by Einstein. In physical terms, this means that we are in the over-damped regime, in this case the Langevin equation reads:

$$-\gamma V_t dt + \alpha dB_t = 0 . \quad (1.3.10)$$

The experiments done during my thesis used a video camera that can reach a maximum of hundreds frames per second (fps) reaching time steps of $\approx 10^{-2}$ s. Therefore, all my work falls into the over-damped regime. Before focusing definitely on Eq. (1.3.10), we can use Eq. (1.3.4) to characterize further the unknown coefficient α . To do so we compute the mean square value of Eq. (1.3.4), starting by taking the second order Taylor expansion:

$$\begin{aligned} d(V_t^2) &\simeq \frac{\partial V_t^2}{\partial V_t} dV_t + \frac{1}{2} \frac{\partial^2 V_t^2}{\partial V_t^2} (dV_t)^2 \\ &= 2V_t dV_t + (dV_t)^2 \end{aligned} \quad (1.3.11)$$

combining Eqs. (1.3.1) and (1.3.11), we obtain by only keeping the terms of order dt :

$$d(V_t^2) = 2V_t \left(-\frac{\gamma}{m} V_t dt + \frac{\alpha}{m} dB_t \right) + \frac{\alpha^2}{m^2} dB_t^2 . \quad (1.3.12)$$

Thus, the average value of $d(V_t^2)$ reads:

$$\langle d(V_t^2) \rangle = -2 \frac{\gamma}{m} \langle V_t^2 \rangle dt + 2 \frac{\alpha}{m} \langle V_t dB_t \rangle + \frac{\alpha^2}{m^2} \langle dB_t^2 \rangle . \quad (1.3.13)$$

Moreover, since dB_t is chosen independently of the velocity V_t , one can write $\langle V_t dB_t \rangle = \langle V_t \rangle \langle dB_t \rangle = 0$. Taking the latter remark into account and the fact that $\langle dB_t^2 \rangle = dt$, Eq. (1.3.13) becomes:

$$\langle d(V_t^2) \rangle = \left[-2 \frac{\gamma}{m} \langle V_t^2 \rangle + \frac{\alpha^2}{m^2} \right] dt . \quad (1.3.14)$$

Since equilibrium averages in thermodynamics must become time independent, we have $\langle d(V_t^2) \rangle = 0$, thus:

$$\langle V_t^2 \rangle = \frac{\alpha^2}{2\gamma m} . \quad (1.3.15)$$

Besides, from the equipartition of energy we also know that:

$$\langle \frac{1}{2} m V_t^2 \rangle = \frac{1}{2} k_B T . \quad (1.3.16)$$

The latter equation permits a direct determination of the amplitude of the noise α :

$$\alpha = \sqrt{2k_B T \gamma} . \quad (1.3.17)$$

The latter result permits computing the amplitude of the random force in the Langevin equation. Taking the over-damped Langevin equation, it reads:

$$V_t dt = \sqrt{2 \frac{k_B T}{\gamma}} dB_t \quad (1.3.18)$$

Furthermore, one can write the position of the particle X_t at a time t , such as:

$$X_t = \int_0^t V_{t'} dt' , \quad (1.3.19)$$

where we can suppose at the initial time $t = 0$ that $X_0 = 0$. Computing $\langle X_t^2 \rangle$ using Eqs. (1.3.18), (1.3.19) and (1.3.3) thus gives:

$$\langle X_t^2 \rangle = 2 \frac{k_B T}{\gamma} t = 2 D t \quad (1.3.20)$$

By relating $\langle X_t^2 \rangle$ to the Mean Square Displacement (MSD) to the initial position such as:

$$\text{MSD} = \langle (X_0 - X_t)^2 \rangle = \langle X_t^2 \rangle , \quad (1.3.21)$$

we obtain that the MSD should be linear with the time. This result confirms that using the over-damped Langevin equation, leads to the Einstein's result Eq. (1.2.11). Where one can identify the diffusion coefficient of the particle to be $D = k_B T / \gamma$. Additionally, the latter identity is called the Stokes-Einstein relation.

Additionally, the Langevin equation is great to compute correlator such as the velocity correlator $\langle V_t' V_{t''} \rangle$ which the simplest to compute and the one that we will detail below. Indeed, if we use the full-Langevin equation, $\langle X_t^2 \rangle$ can't be that easily computed since $m dV_t$ does not vanish. We would thus need to rewrite Eq. (1.3.20) using the velocity correletor such as:

$$\langle X_t^2 \rangle = \int_0^t \int_0^t \langle V_{t'} V_{t''} \rangle dt' dt'' . \quad (1.3.22)$$

Let us now study how the two-point correlator function $\langle V_t' V_{t''} \rangle$, using the full-Langevin

equation multiplied by V_0 and following the same steps as for Eq. (1.3.9), one has:

$$\langle V_t V_0 \rangle = \langle V_0^2 \rangle e^{-t/\tau_B} . \quad (1.3.23)$$

As the equilibrium state is invariant under temporal translation and assuming that V_0 has an equilibrium steady-state distribution with $\langle V_0^2 \rangle = k_B T / m$ we have:

$$\langle V_t V'_t \rangle = \frac{k_B T}{m} e^{-|t-t'|/\tau_B} . \quad (1.3.24)$$

One can solve Eq. (1.3.22) by splitting the integral in two parts, where $t' > t''$ and $t' < t''$:

$$\begin{aligned} \langle X_t^2 \rangle &= \frac{k_B T}{m} \int_0^t dt' \int_0^{t'} dt'' e^{-|t'-t''|/\tau_B} = 2 \frac{k_B T}{\gamma} \left(\int_0^t dt' \left[1 - e^{-t'/\tau_B} \right] \right) \\ &= 2 \frac{k_B T}{\gamma} \left(t - \tau_B \left[1 - e^{-t/\tau_B} \right] \right) . \end{aligned} \quad (1.3.25)$$

We can extract two results from that equation. At a short time $t \ll \tau_B$, one has:

$$\begin{aligned} \langle X_t^2 \rangle &\simeq 2 \frac{k_B T}{\gamma} \left(t - \tau_B \left[1 - 1 + \frac{t}{\tau_B} - \frac{t^2}{2\tau_B^2} \right] \right) \\ &= \frac{k_B T}{m} t^2 . \end{aligned} \quad (1.3.26)$$

This is the ballistic regime. If one can experimentally explore times shorter than τ_B one will then measure the real velocity of the particle. At longer times, $t \gg \tau_B$, the MSD is given by:

$$\langle X_t^2 \rangle \simeq 2 \frac{k_B T}{\gamma} t = 2 D t . \quad (1.3.27)$$

This is the diffusive regime where the MSD, as found earlier, Eq. (1.3.20) with the over-damped Langevin equation. To study this different result, it can be interesting to simulate the Brownian motion.

1.4 Numerical simulation of bulk Brownian motion

1.4.1 The numerical Langevin Equation

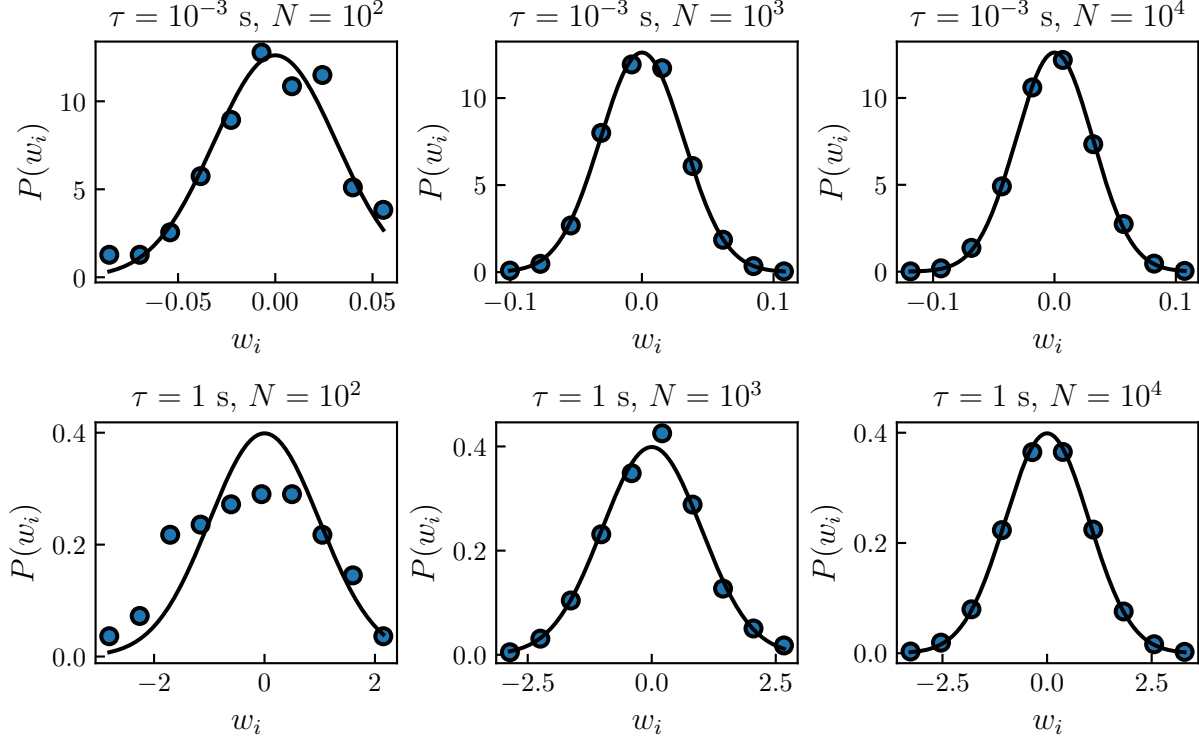


Figure 1.4.1: Bullets represents the probability density function of w_i , a Gaussian-distributed number with a mean value $\langle w_i \rangle$ and a variance $\langle w_i^2 \rangle = \tau$. The plain black line is a Gaussian distribution of zero mean and a τ variance (see Eq. (1.4.3)). On the first line, the simulation is done with $\tau = 10^{-3}$ s and $\tau = 1$ s on the second one. Each column corresponds to a number N of draws. From the left to the right: $N = 10^2$, 10^3 and 10^4 .

The Langevin equation is an ordinary differential equation that can easily be numerically simulated in the bulk case. One approximates the continuous position X_t of a particle at a time t by a discrete-time sequence x_i which is the solution of the equation at a time $t_i = i\tau$, τ being the time step of the simulation. One can then use the Euler method to numerically write V_t as:

$$V_t \simeq \frac{x_i - x_{i-1}}{\tau}, \quad (1.4.1)$$

and dV_t/dt as

$$\begin{aligned}\frac{dV_t}{dt} &\simeq \frac{\frac{x_i - x_{i-1}}{\tau} - \frac{x_{i-1} - x_{i-2}}{\tau}}{\tau} \\ &= \frac{x_i - 2x_{i-1} + x_{i-2}}{\tau^2}.\end{aligned}\quad (1.4.2)$$

The only term remaining to be computed numerically is the random term dB_t . One can thus replace dB_t/dt by w_i/τ ¹ a Gaussian distributed random number generated with a mean $\langle w_i \rangle = 0$ and a variance $\langle w_i^2 \rangle = \tau$. The Probability Density function (PDF) of the Gaussian distribution is thus given by:

$$P(w_i) = \frac{1}{\sqrt{2\pi\tau}} e^{-\frac{w_i^2}{2\tau}}. \quad (1.4.3)$$

The random number w_i can be generated with the following Python snippet.

```

1 import numpy as np
2
3 tau = 0.5 # time step in seconds
4 wi = np.random.normal(0, np.sqrt(tau))

```

In the latter, `random.normal()` is a built-in Numpy module that permits the generation of Gaussian-distributed random numbers. Finally, by combining Eqs. (1.4.1) and (1.4.2), the full-Langevin equation becomes:

$$m \frac{x_i - 2x_{i-1} + x_{i-2}}{\tau^2} = -\gamma \frac{x_i - x_{i-1}}{\tau} + \sqrt{2k_B T \gamma} \frac{w_i}{\tau}. \quad (1.4.4)$$

From the latter, one can write x_i as:

$$x_i = \frac{2 + \tau/\tau_B}{1 + \tau/\tau_B} x_{i-1} - \frac{1}{1 + \tau/\tau_B} x_{i-2} + \frac{\sqrt{2k_B T \gamma}}{m(1 + \tau/\tau_B)} \tau w_i, \quad (1.4.5)$$

where we can observe that two initial conditions are needed, the first two positions of the particle. Numerically, these positions could be randomly generated or set to 0. If enough statics are generated, it will not affect the results.

¹ The notation w was chosen since in mathematical terms, a real-valued continuous-time stochastic process such as dB_t is called a Wiener process in honor of Norbert Wiener [7].

1.4.2 Simulating Brownian Motion Using Python

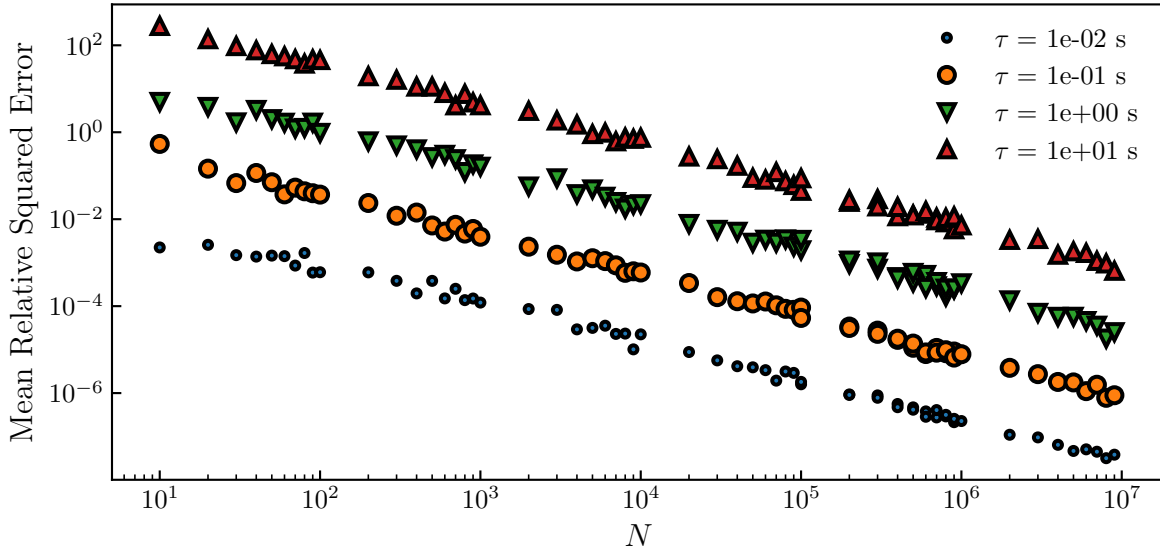


Figure 1.4.2: Mean Relative Squared Error (MRSE) of the Probability Density Function PDF measured from a generation of N Gaussian random numbers w_i and the actual Gaussian (see Eq. (1.4.3)) from which the generation is done. The generation is done over a Gaussian which has a mean value $\langle w_i \rangle = 0$ and variance $\langle w_i^2 \rangle = \tau$. We explore parameter ranges from $N = 10$ to 10^7 and $\tau = 10^{-2}$ to 10 s.

Before, diving into the simulation, it could be interesting to ask ourselves how long the simulation should be. Indeed, at equilibrium, the different observables' mean values to remain constant we should wait a sufficient amount of time. It is possible to follow a qualitative approach by generating N numbers w_i , measuring the resulting PDF $P_c(w_i)$ and looking for how much we need to increase N to have $P_c(w_i) \approx P(w_i)$, under some given small-error criterion. As we can see in Fig. 1.4.1, for simulations made with $\tau = 10^{-3}$ s and $\tau = 1$ s, we observe that as we increase N , the measured PDF, gets closer to the real one given by Eq. (1.4.3).

To have a more quantitative approach, one can compute the Mean Relative Squared Error (MRSE) between the measured PDF $P_c(w_i)$ and the nominal function $P(w_i)$ as a function of the number N of generated numbers, as:

$$\text{MRSE} = \left\langle \frac{(P_c(w_i) - P(w_i))^2}{P(w_i)^2} \right\rangle_N \quad (1.4.6)$$

where the notation $|_N$ denotes the average over N realizations. Additionally, since we measure $P_c(w_i)$ by doing a histogram, the question of how many bins are used should

be answered. It is possible to use the optimal Freedan-Diaconis rule [8] to compute the width of the bins to be used in a histogram. This rule reads:

$$\text{Bin width} = 2 \frac{\text{IQR}(\{w_i\})}{\sqrt[3]{N}}, \quad (1.4.7)$$

where IQR is the interquartile range, and $\{w_i\}$ a sample of N random numbers w_i . Moreover, one should at least take 2 bins as a minimum. The optimal number of bins can be computed using the following Python snippet.

```

1 import numpy as np
2
3
4 def _iqr(wi):
5     """Function to compute interquartile range."""
6     return np.subtract(*np.percentile(x, [75, 25]))
7
8 def optimal_bins(wi):
9     """
10     Function to compute the optimal number of bins using Freedan-Diaconis rule.
11     Input: list of random numbers / Output: optimal bins number
12     """
13
14     n = int(diff(wi) / (2 * _iqr(wi) * np.power(len(wi), -1 / 3)))
15
16     if n <= 2:
17         return 2
18     else:
19         return n

```

As we can see in Fig.1.4.2, for τ varying between 10^{-2} and 10 seconds, and N between 10 and 10^6 , the MRSE decreases as N increases. Moreover, it is interesting to observe that the MRSE is greater as τ increases for a fixed N value. As an example, we would need to only generate $N = 10^{-3}$ numbers to obtain an MRSE of 10^{-4} for $\tau = 0.1$ s, while we would need to $N = 10^6$ for $\tau = 1$ s.

Now that the Langevin equation has been numerically implemented, one could use it to simulate Brownian trajectories. A simple way to do the simulation using Python is provided in appendix.???. A set of trajectories simulated for a fictive particle of radius $a = 1 \mu\text{m}$ and mass $m = 10 \mu\text{g}$ in water is shown in Fig.1.4.3-a). For such a particle, the diffusive characteristic time is $\tau_B = 0.53$ s. Moreover, as one can see in Fig.1.4.3-b), the

MSD is correctly modeled by Eq. (1.3.26) for $\tau \ll \tau_B$, and by Eq. (1.3.27) for $\tau \gg \tau_B$. Note that for non-continuous data such as the simulation data presented here or sampled experimental trajectories, and for a given time increment Δt , the MSD is generally defined by:

$$\langle \Delta x^2 \rangle_t = \langle (x_i(t + \Delta t) - x_i(t))^2 \rangle_t , \quad (1.4.8)$$

where the average $\langle \rangle|_t$ is performed over time t . The following Python function can be used to numerically compute the MSD Eq. (1.4.8).

```

1 def msd(x, Dt):
2     """Function that returns the MSD for a list of time indices Dt for a trajectory x"""
3     _msd = lambda x, t: np.mean((x[:-Dt] - x[Dt:]) ** 2)
4     return [_msd(x, i) for i in t]

```

Additionally, as we have seen earlier, the Langevin Equation can be simplified to it is over-damped version of Eq. (1.3.10). In this case, the time step τ of the simulation should be greater than the characteristic time τ_B . Thus, if one is interested in the long-time statistical properties of Brownian motion one can use the over-damped Langevin equation. In this case, by putting $m = 0$ into Eq. (1.4.5), one can write x_i as:

$$x_i = x_{i-1} + \sqrt{2D}w_i . \quad (1.4.9)$$

The statistical properties at a long time could be retrieved by simulating Brownian motion using the full-Langevin equation. But, since the integration scheme used for Eq. (1.4.5) requires $\tau \ll \tau_B$, long simulation runs are necessary to retrieve the over-damped properties. A simulation of the over-damped Brownian motion trajectories using Eq. (1.4.9) is shown in Fig.1.2.1 and is realized using the following Python Snippet.

```

1 import numpy as np
2
3 N = 1000 # trajectory length
4 D = 1 # diffusion coefficient
5 tau = 0.5 # time step
6 trajectory = np.cumsum(np.sqrt(2 * D) * np.random.normal(0, np.sqrt(tau), N))

```

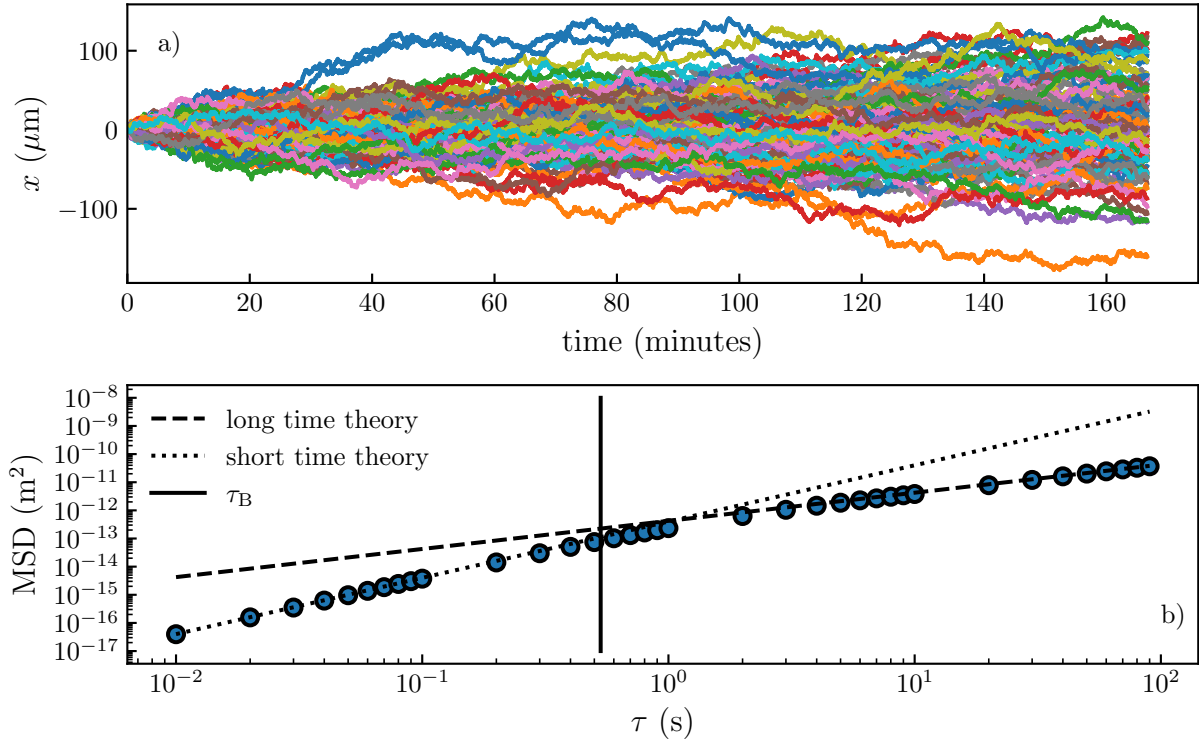


Figure 1.4.3: a) Set of 100 trajectories simulated using the full-Langevin equation (see Eq. (1.4.5)) for particles of a radius $a = 1 \mu\text{m}$ and mass $m = 10 \mu\text{g}$ in water, with viscosity $\eta = 0.001 \text{ Pa.s}$. The simulations are done with a time step $\tau = 0.01 \text{ s}$. b) Bullets represent the measured Mean Squared Displacements (MSD) of the simulated trajectories. The plain black line represents the characteristic inertial timescale, $\tau_B = m/\gamma = 0.53 \text{ s}$. The dotted line represents the MSD in the ballistic regime (see Eq. (1.3.26)), when $t \ll \tau_B$. The dashed line represents the MSD in the diffusive regime (see Eq. (1.3.27)), when $t \gg \tau_B$, $MSD = 2D\tau$. A detailed explanation of the simulation process can be found in appendix.??.

1.4.3 Speedup using Cython

I would like to point out that the optimization of a simple simulation of a Brownian trajectory can be interesting. Indeed, using a pure Python code as presented in the first part of appendix.??, the simulation of one trajectory of 10^6 steps, needs 6 s to be computed. Thus, more than 10 minutes are required to compute the 100 trajectories shown in Fig.1.4.3. This is long and due to how Python systematically verifies what we do is allowed. Indeed, it verifies at each step of the `for` loop the object type of each variable and if the mathematical operation are possible. This is generally the main drawback [9] of interpreted language, and the only solution is to use a compiled language (*e.g.* C or Fortran).

The difference between an interpreted (*e.g.* Python) and compiled language (*e.g.* C) lies in the result of the process of interpreting or compiling. A compiler (*e.g.* gcc for

the C language  translate the source code into the computer native language, and create an executable file. The execution of compiled language does not require any more translations, and hence run significantly faster. Contrariwise, an interpreted language is not translated in advance, but is done at the execution, line by line, and each time the program is executed. This process is done by the interpreter, such as Python, Matlab or Perl for their eponymous language. At each execution, the time taken by the interpreter to read and execute each line slow the process, causing execution to take more time.

To overcome this problem with Python, the `cython` package has been developed to translate in C and compile the part of the code that is long to execute, especially the `for` loops. Thus, one can transform is Python source code into a hybrid Python-C code. As presented in appendix.??, compiling the `for` loop using `cython` in the full-Langevin simulations reduces the time to generate a 10^6 -step trajectory from 6 s to 30 ms thus achieving a speedup factor of 200. Moreover, in the hybrid version, the execution time is limited by the random number generation. Indeed, it takes $\approx 24.0\text{ms}$ using `numpy` to generate $10^6 w_i$ numbers and $\approx 6\text{ ms}$ for the trajectory computation. Additionally, as shown at the end of appendix.??, even a pure C implementation of the random generation can be slower than the `numpy` one, thanks to `numpy`'s memory optimization. Thus, by using the above mixed-language strategy, the simulation is optimal with the current tools and language at hand.

1.5 Conclusion

In this chapter, we have covered the history of Brownian motion, from the first observation by Robert Brown in the middle of the 19th century to its mathematical and experimental proofs in the early 20th century. We have then described mathematically the bulk Brownian motion and its important statistical properties. Finally, we have used the latter description to simulate Brownian motion using both the full-Langevin equation, and its over-damped version.

2 Particle Characterization and Tracking Using Optical Interferences

2.1 Introduction

Properties of coherent light to produce interference has been widely deployed in metrology for a long time as illustrated by, for example, the famous Fabry-Pérot [10, 11] and Michelson interferometers [12]. The latter was initially employed to evaluate the rotation of the Earth and is still deployed today for the recent measurement of gravitational waves [13]. Since the beginning of the century, interest on tracking and characterizing colloidal particles risen thanks to the democratization of micro fluidics and lab-on-a-chip technologies. In the following, I will provide some insights on the three most used tracking methods:

- Reflection Interference Contrast Microscopy (RICM)
- Lorenz-Mie theory
- Rayleigh-Sommerfeld back propagation

The first one, RICM, uses the principle of optical-path difference in a Michelson interferometer. The other two, use the interferences between the light scattered by the colloid and the incident light. Generally, both sources are collinear, so that we speak of in-line holography.

2.2 Reflection Interference Contrast Microscopy

RICM was first introduced in cell biology by Curtis to study embryonic chick heart fibroblasts [14] in 1964. RICM gained in popularity 40 years after both in biology and physics [15–20]. It was also used recently in soft matter physics to study the elastohydrodynamic lift at a soft wall [21].

When we illuminate a colloid with a plane wave from the bottom, a part of the light is reflected at the surface of the glass substrate and another part, at the colloid surface. The difference of optical paths between two reflections creates an interference pattern. Let us focus on the mathematical description of this phenomenon. In the far field, we can describe two one-dimensional electric field vectors with same angular frequency ω [22] as propagative waves, through:

$$\vec{E}_1(\vec{r}, t) = \vec{E}_{01} \cos(\vec{k}_1 \cdot \vec{r} - \omega t + \epsilon_1), \quad (2.2.1)$$

and:

$$\vec{E}_2(\vec{r}, t) = \vec{E}_{02} \cos(\vec{k}_2 \cdot \vec{r} - \omega t + \epsilon_2), \quad (2.2.2)$$

where the k_i are the wave vector satisfying $|\vec{k}_i| = k = 2\pi n_m / \lambda$, the angular wavenumber, λ being the illumination wavelength, n_m the optical index of the medium, $\epsilon_{1,2}$ the initial phases of each wave and \vec{r} the position. Here, the origin ($\vec{r} = \vec{0}$) is taken at the position of the first reflection (*i.e.* the glass slide). Thus, on the particle, \vec{r} is given by the particle's height such that $|r| = z$.

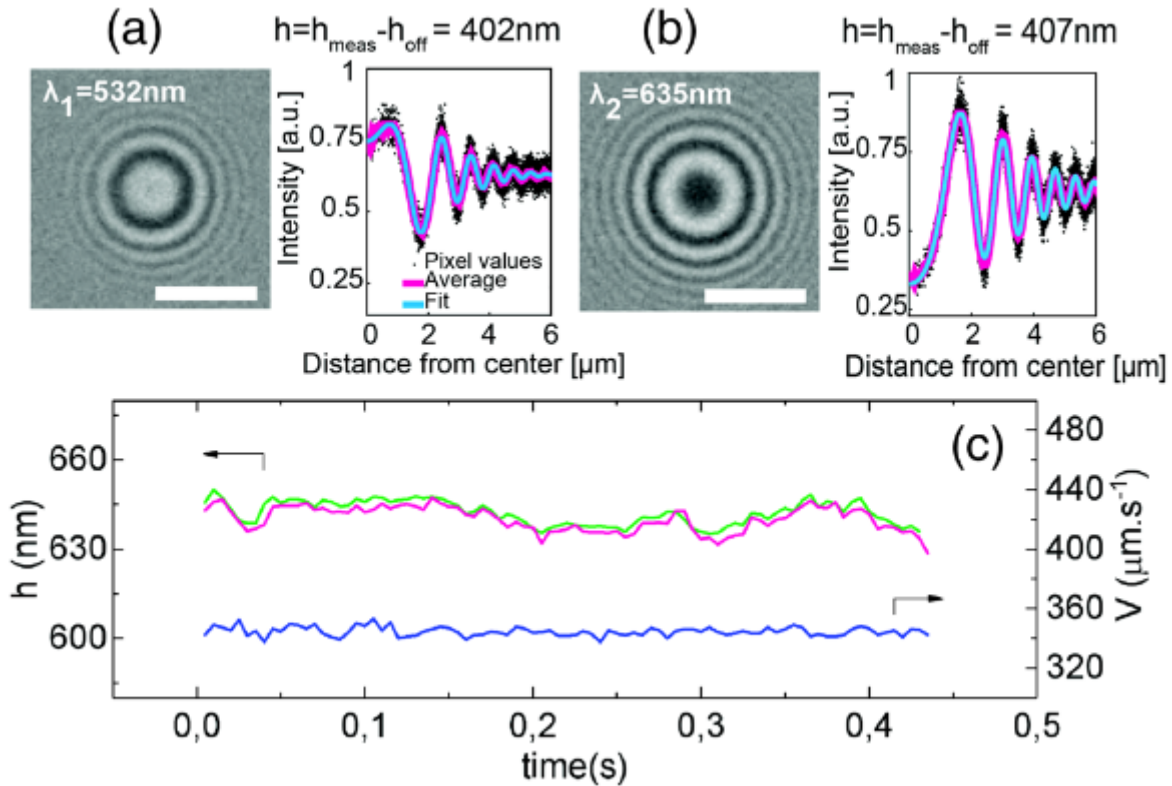


Figure 2.2.1: Figure from [21] representing RICM with two wavelengths. (a) Left: interference patterns created with a wavelength $\lambda_1 = 532\text{ nm}$ (scale bar $5\text{ }\mu\text{m}$). Right: radial intensity profile (black dots) extracted from the image, azimuthally averaged (magenta line) and fitted with Eq. (2.2.8) to measure the height of the particle (here noted h). (b) Same as (a) with a wavelength $\lambda_2 = 635\text{ nm}$. (c) Time series of the height h of a particle (green: λ_1 , purple: λ_2) and the particle velocity measured along the flow (in blue).

Experimentally, one measures the intensity of the interference patterns. They can be computed from the time-averaged squared total electric field $\vec{E} = \vec{E}_1 + \vec{E}_2$. The measured intensity is thus given by:

$$I = \langle \vec{E}^2 \rangle = \langle \vec{E}_1^2 + \vec{E}_2^2 + 2\vec{E}_1 \cdot \vec{E}_2 \rangle = \langle \vec{E}_1^2 \rangle + \langle \vec{E}_2^2 \rangle + 2 \langle \vec{E}_1 \cdot \vec{E}_2 \rangle , \quad (2.2.3)$$

where $\langle \vec{E}_1^2 \rangle$ and $\langle \vec{E}_2^2 \rangle$ are respectively given by I_1 and I_2 , the incident intensities. Using trigonometry, we have:

$$\langle \vec{E}_1 \cdot \vec{E}_2 \rangle = \left\langle \frac{1}{2} \vec{E}_{01} \vec{E}_{02} \left[\cos(\vec{k}_1 \cdot \vec{r} - \vec{k}_1 \cdot \vec{r} + \phi) + \cos(2\omega t + \phi') \right] \right\rangle_t . \quad (2.2.4)$$

As we average over time, the second cosine vanishes. Thus one has:

$$\langle \vec{E}_1 \cdot \vec{E}_2 \rangle = \frac{1}{2} \langle \vec{E}_{01} \vec{E}_{02} \rangle \cos(\vec{k}_1 \cdot \vec{r} - \vec{k}_2 \cdot \vec{r} + \phi) , \quad (2.2.5)$$

with ϕ the phase difference between the two fields, which is usually equal to π due to the reflection properties on a higher optical index. Indeed, a colloid has generally a greater optical index than the dilution medium. Finally, the total intensity can be read as:

$$I = I_1 + I_2 + 2\sqrt{I_1 I_2} \cos(\vec{k}_1 \cdot \vec{r} - \vec{k}_2 \cdot \vec{r} + \phi) . \quad (2.2.6)$$

By taking $k_1 = -k_2$ due to the reflection properties, we have:

$$I = I_1 + I_2 + 2\sqrt{I_1 I_2} \cos\left(\frac{4\pi n_m}{\lambda} z + \phi\right) . \quad (2.2.7)$$

So far we supposed that the reflection occurs at a unique point; however, we would likely be using spherical colloids. Therefore, illuminating from the bottom, the reflection happens on half of the sphere surface. Moreover, thanks to the spherical geometry the holograms exhibit a radial symmetry, we thus write one can write the radial interference intensity $I(x)$, with x the distance from the pattern center, through [20]:

$$I(x) = A_0 + A_1 e^{-b_1 x^2} + A_2 e^{-b_2 x^2} \cos\left[\frac{4\pi n_m}{\lambda} (g(x) + z) + \phi\right] , \quad (2.2.8)$$

Where A_1 and b_1 are parameters [20] that fit the slightly bent background that arises from diffuse reflection on the upper part of the sphere, A_2 and b_2 the decaying contrast

of the higher order maxima, A_0 background intensity, and

$$g(x) = a - \sqrt{a^2 - x^2} , \quad (2.2.9)$$

is the sphere profile, to consider the increase sphere-wall as x increases. Finally, this method benefits from equations that are computationally light and enable a quick tracking of particles. However, as we can see in Eq. (2.2.8), because of the periodicity of the cosine, the interference pattern is the same for all heights z separated by a distance $\lambda/(2n_m) \approx 200$ nm for $\lambda = 532$ nm and $n_m = 1.33$.

It is possible to extend this separation to $\simeq 1.2 \mu\text{m}$ as used in [21] length by using two different wavelengths. Despite the spatial resolution of this method which can attain 10 nm, the measurement ambiguity is not compatible with the study of Brownian motion due to the periodicity above. Hence RICM it is not usable in our context. As a matter of fact, we experimentally reach height spans of a few microns.

2.3 Lorenz-Mie theory

When a colloid is illuminated with a plane wave, a part of the light is scattered. In consequence, the incident field \vec{E}_0 and scattered field \vec{E}_s interferes. The interference patterns thus obtained are called holograms. If the particle is not smaller than the illumination wavelength, it is not possible to use Rayleigh's approximations [23] to describe the scattering. Instead, one needs to use the Lorenz-Mie theory for dielectric spheres. This theory was developed by Lorenz and independently by Mie in 1880 and 1908, respectively [24, 25].

It is in the early 2000s that the Lorenz-Mie theory was first used in order to track and characterize particles [26, 27]. Since then, a lot of studies have been realized with this technique [28]. In the following, I will describe the Lorenz-Mie method. In this part, the height z of the particle is the distance between the particle's center and the focal plane of the objective lens.

Let the incident field be a plane wave uniformly polarized along an axis \hat{e} , with an amplitude E_0 and propagating along the \hat{z} direction :

$$\vec{E}_0(\vec{r}, z) = E_0(\vec{r}) e^{ikz} \hat{e} \quad (2.3.1)$$

Let us consider a particle of radius a at a position \vec{r}_p . In such case, the scattered field can be written using the Lorenz-Mie theory [22], as:

$$\vec{E}_s(\vec{r}, z) = \vec{f}_s(k(\vec{r} - \vec{r}_p)) E_0(\vec{r}) \exp(-ikz) , \quad (2.3.2)$$

with \vec{f}_s , the Lorenz-Mie scattering function. The intensity I that we measure at \vec{r} is given by the intensity of superimposition of the incident and scattered amplitudes. Since the measurements are done at the focal plane, i.e. $z = 0$, I is given by:

$$\begin{aligned} I(\vec{r}) &= |\vec{E}_s(\vec{r}, 0) + \vec{E}_0(\vec{r}, 0)|^2 \\ &= E_0^2(\vec{r}) + 2E_0^2 \Re \left(\vec{f}_s(k(\vec{r} - \vec{r}_p)) \hat{e} \right) + |\vec{f}_s(k(\vec{r} - \vec{r}_p))|^2 . \end{aligned} \quad (2.3.3)$$

Most of the experimental defects on the images are due to spacial illumination variations caused by dust particles. They can be corrected by normalizing the image by the background. In another word, we normalize $I(\vec{r})$ by the intensity of the incident field $I_0 = E_0(\vec{r})^2$ which corresponds the experimental background.

Experimentally, the background can be measured by different methods. One is to have an empty field of view and the other one, which is more convenient, is to compute the median of a stack of images. Additionally, for the latter to work, the video should be long enough for the particle to diffuse sufficiently. If this condition is not satisfied, a ghost of the particle will appear on the background. Moreover, this process permits getting rid of any immobile particles that could generate any additional noise. Examples of hologram before and after the normalization are shown in Figs.2.3.1 a-c).

Finally, we write the normalized intensity as:

$$\frac{I(\vec{r})}{I_0(\vec{r})} = 1 + 2\Re \left(\vec{f}_s(k(\vec{r} - \vec{r}_p)) \hat{e} \right) + |\vec{f}_s(k(\vec{r} - \vec{r}_p))|^2 \quad (2.3.4)$$

Now that we have the analytical form of the holograms' intensity, it is possible to fit an experimental one to Eq. (2.3.4) as shown in Figs.2.3.1 d-e). For the sake of completeness, I will detail the Lorenz-Mie scattering function $\vec{f}_s(k\vec{r})$, which is given by the series:

$$\vec{f}_s(k\vec{r}) = \sum_{n=1}^{n_c} \frac{i^n (2n+1)}{n(n+1)} \left(ia_n \vec{N}_{\text{eln}}^{(3)}(k\vec{r}) - b_n \vec{M}_{\text{ohn}}^{(3)}(k\vec{r}) \right) \quad (2.3.5)$$

where $\vec{N}_{eln}^{(3)}(k\vec{r})$ and $\vec{M}_{oln}^{(3)}(k\vec{r})$ are the vectorial spherical harmonics, and a_n and b_n are coefficients depending on the particle and illumination properties. For a spherical and isotropic particle of radius a and refractive index n_p , which is illuminated by a linearly polarized plane wave, the a_n and b_n coefficients are expressed in terms of spherical Bessel functions j_n and Hankel functions h_n , as [22]:

$$a_n = \frac{\zeta^2 j_n(\zeta ka) k a j'_n(ka) - j_n(ka) [\zeta k a j_n(\zeta ka)]'}{\zeta^2 j_n(\zeta ka) k a h_n^{(1)'}(ka) - h_n^{(1)}(ka) \zeta k a j'_n(\zeta ka)}, \quad (2.3.6)$$

and:

$$b_n = \frac{j_n(\zeta ka) k a j'_n(ka) - j_n(ka) \zeta k a j'_n(mka)}{j_n(\zeta ka) k a h_n^{(1)'}(ka) - h_n^{(1)}(ka) \zeta k a j'_n(mka)}, \quad (2.3.7)$$

where $\zeta = n_p/n_m$, and where the prime notation denotes differentiation with respect to the argument.

Finally, a hologram is mainly given by the Lorenz-Mie scattering function of Eq. (2.3.5). Moreover, as we can observe in Eqs. (2.3.6) and (2.3.7), a hologram depends on a lot of parameters and variables (λ , n_m , n_p , a and \vec{r}_p). The parameters can be fitted by comparison to experimental data. In general, the illumination wavelength λ and medium index n_m are known and do not need to be fitted. From only one hologram, one can measure the position \vec{r}_p precisely of the particle and simultaneously characterize the radius and optical index of the colloid. As a side note, it is even possible to characterize a particle without aprioristic knowledge of its characteristics using a Bayesian approach [29, 30].

Computing Eq. (2.3.5) numerically brings another interesting question, as it is analytically written as a sum over n . One could ask after which number n_c of terms the series converges. It has actually been found that the series converges after a number of terms given by [31]:

$$n_c = ka + 4.05(ka)^{1/3} + 2. \quad (2.3.8)$$

Consequently, the holograms of bigger particles require more terms to converge and, hence, are longer to fit. As an example, the largest particles used during my thesis have a radius $a = 2.5 \mu\text{m}$ leading to $n_c = 55$ in water and for an illumination wavelength $\lambda = 532 \text{ nm}$. For the smallest ones, where $a = 0.5 \mu\text{m}$ we find $n_c = 18$ which makes a huge difference in practice. Indeed, if each of the terms of the sum takes the same time to be computed; a $2.5 \mu\text{m}$ particle's hologram is $55/18 \simeq 3$ times longer to be fitted compared to the

hologram of a $0.5 \mu\text{m}$ particle.

If a reader wants to evaluate a hologram given by the Lorenz-Mie theory for a peculiar particle and position, it can be done in a few lines with the `holopy` module utilizing the following Python snippet which was employed to make Fig.2.3.7 and 2.3.8:

```
1 import holopy as hp
2 from holopy.scattering import calc_holo, Sphere
3
4 sphere = Sphere(n=1.59, r=1.5, center=(4/0.1, 4/0.1, 10))
5 # n is the optical index of the particle, r its radius in microns
6 # center is its center position in microns.
7
8 medium_index = 1.33
9 illum_wavelen = 0.532
10 illum_polarization = (1, 0)
11 detector = hp.detector_grid(shape=100, spacing=0.1)
12 # shape is the size in pixels of the camera and the spacing is the pixel's size in microns.
13
14 holo = calc_holo(
15     detector, sphere, medium_index, illum_wavelen, illum_polarization, theory="auto"
16 )
17 #the hologram can directly be plotted using:
18 hp.show(holo)
```

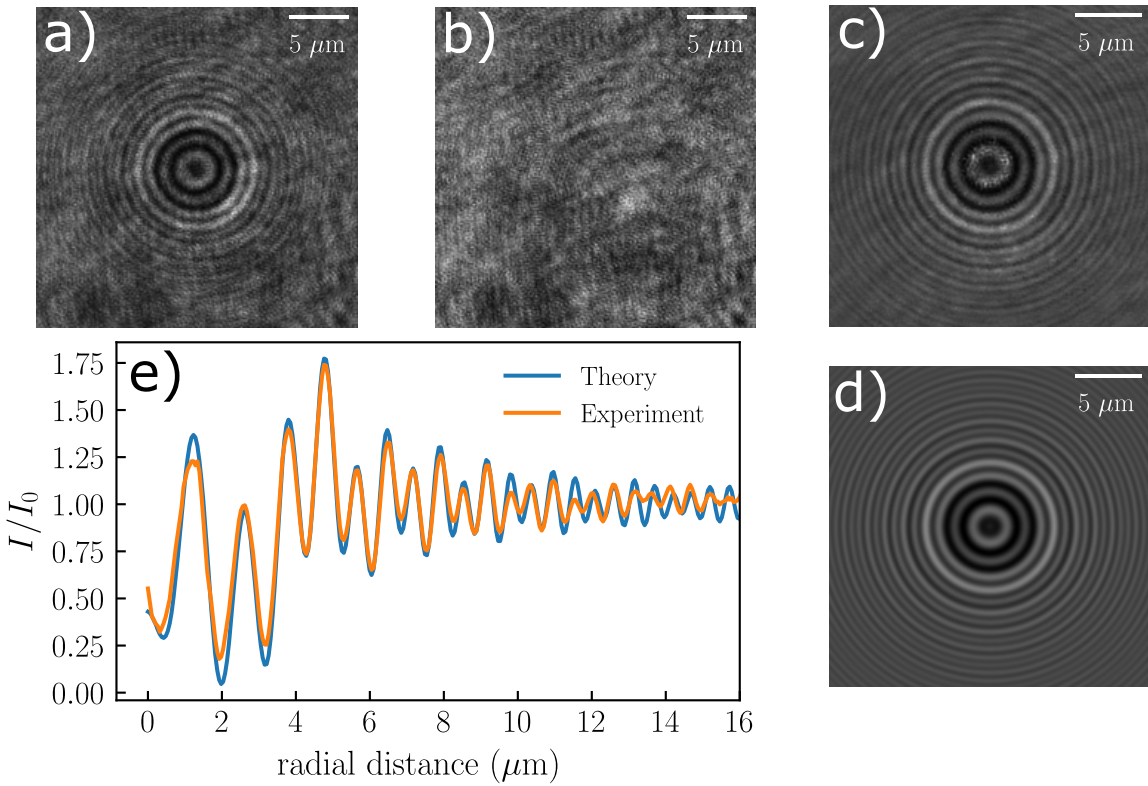


Figure 2.3.1: a) Raw hologram of a $2.5 \mu\text{m}$ polystyrene particle measured experimentally with the setup detailed in the section 2.5. b) Background obtained by taking the median value of an image time series. c) Normalized hologram given by dividing a) by b). d) Result of the fit of c) using Eq. (2.3.4), from which the particle is found to be at a height $z = 14.77 \mu\text{m}$. e) Comparison of the normalized radial intensities, obtained experimentally from c) and theoretically from d).

2.3.1 Hologram dependence on the particle's characteristics

As we can see with the Eq. (2.3.5), the in-line holograms vary with the position, radius and optical index of the particle. For in-line holograms, as both incident and scattered field are collinear, the x and y positions of the particle are given by the center of the hologram. Thus, it is possible to track the motion of a colloid only in two dimensions by using algorithms such as the Hough transforms to find the center. As a side note, in that case, it would be optimal to place the particle just above the focal plane to have an Airy disk-like hologram, as shown in Fig.2.3.8 for $a = 2.5 \mu\text{m}$ and $z = 5 \mu\text{m}$.

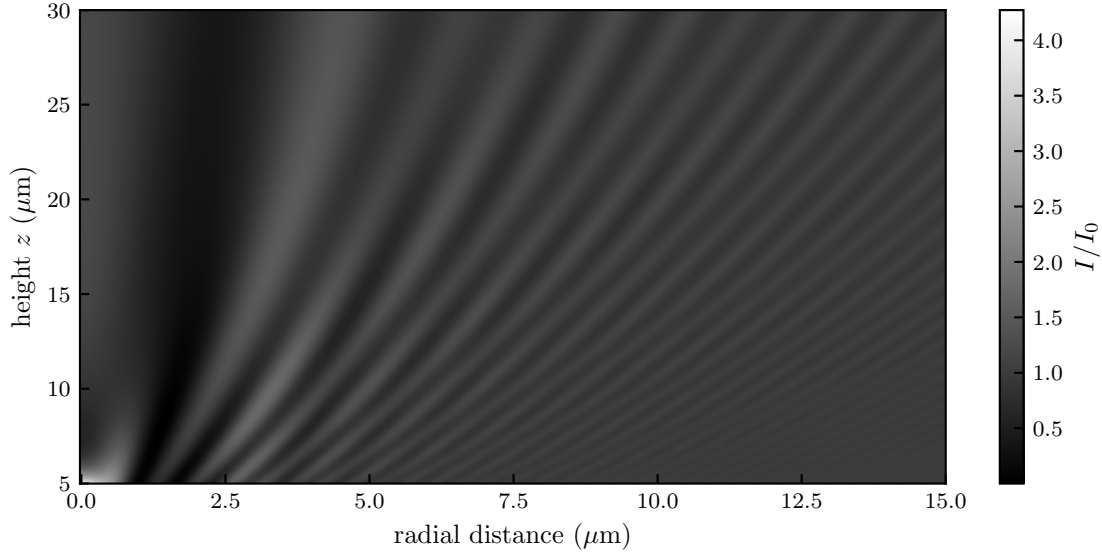


Figure 2.3.2: Hologram intensity map in the (r, z) -plan, calculated (see. Eq. (2.3.4)) for a particle of radius $a = 1.5 \mu\text{m}$ and optical index $n = 1.59$.

In order to gain some insights on how the holograms vary with the various parameters, one can compute theoretical (see. Eq. (2.3.4)) holograms for particles of different sizes and heights. We start by considering a particle of radius $a = 1.5 \mu\text{m}$, and optical index $n_p = 1.59$ as shown in Fig.2.3.2. In this case, one can observe that as the distance z between the particle and the focal plane increases, the hologram's rings get wider.

Additionally, this thickening of the rings can also be observed in the Fig.2.3.6, where hologram intensity profiles are plotted as a function of the height z both theoretically and experimentally for a polystyrene colloidal particle of radius $a = 1.5 \mu\text{m}$, and for different couples of parameters in Fig.2.3.8.

Also, we note that if z is not large enough compared to the radius of the particle, the center of a hologram can be so bright that the rings could not be seen if the camera does not have a large enough dynamic range. Thus, for having an optimal condition for the fits, one should take care of defocusing enough the objective lens to have $z \gg a$.

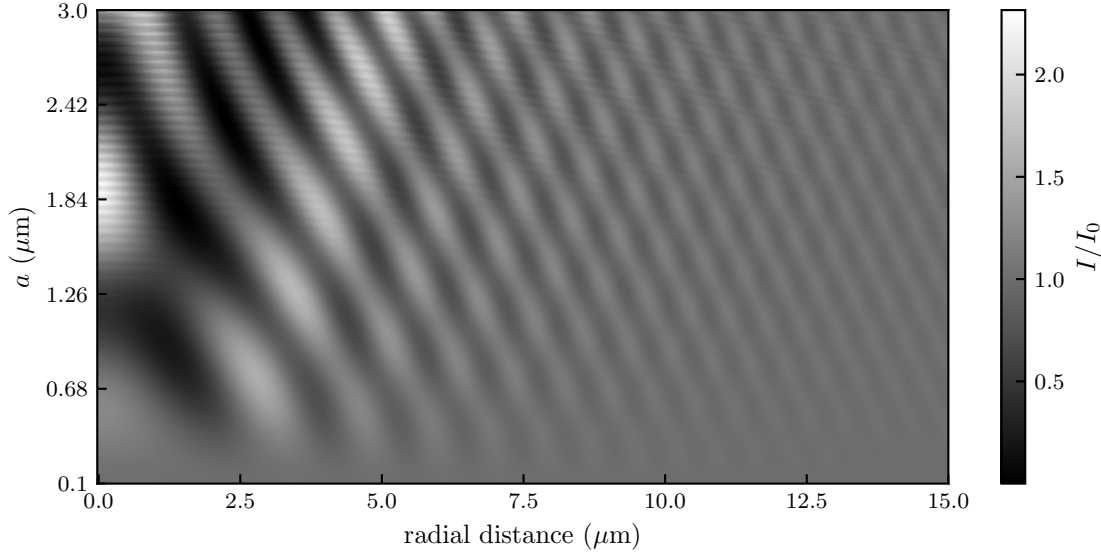


Figure 2.3.3: Hologram intensity map in the (r, a) -plan, calculated (see. Eq. (2.3.4)) for a particle of optical index $n = 1.59$, and a distance $z = 15 \mu\text{m}$ between the particle center and the focal plane of the objective lens.

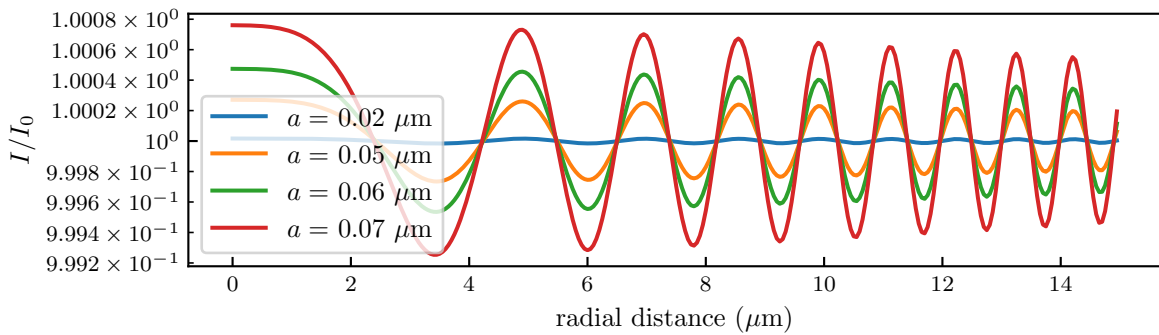


Figure 2.3.4: Radial intensity profile for particle radius $a \ll \lambda$, and an optical index $n_p = 1.59$ with a distance $z = 15 \mu\text{m}$ between the particle center and the focal plane of the objective lens, and for a wavelength $\lambda = 532 \text{ nm}$.

We can now look at the holograms variation with respect to the radius of the particle as shown in Fig.2.3.3 for a particle of optical index $n = 1.59$ and at a distance $z = 15 \mu\text{m}$. One can observe that for small particles compared to the wavelength, *i.e.* $a \ll \lambda$, we do not observe the rings. This is due to the fact that for the small particles, the scattering can be approximated using the Rayleigh theory in which the scattering is isotropic. Thus, the variation of intensity around I_0 will be smaller for smaller particles.

Also, in this small-particle regime, the particle size does not affect the general shape of the hologram but just its intensity as shown in Fig.2.3.4, for particles of radii between $a = 0.02 \mu\text{m}$ and $a = 0.07 \mu\text{m}$, and for a wavelength $\lambda = 532 \text{ nm}$.

Additionally, since the signal-to-noise ratio is lower than for larger particles, it is less precise to characterize small colloids compared to the wavelength.

As the particle gets bigger, the scattering becomes anisotropic and is mostly oriented towards the incident plane-wave direction. This effect leads to an increase of the amplitude I/I_0 of the rings, as one can see in Fig.2.3.3. Thus, the signal-to-noise ratio is high enough to easily discern the hologram on top of the noise as one can see on the experimental picture of Fig.2.3.1-a). One who wants to employ this method should thus use large enough particles for the hologram intensity to be greater than the camera noise level.

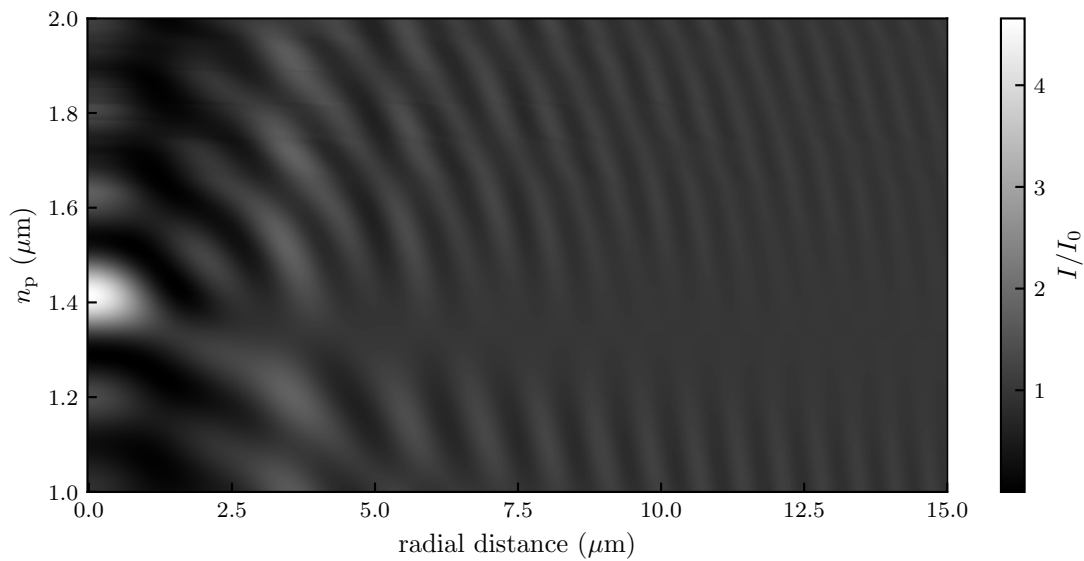


Figure 2.3.5: Hologram intensity map in the (r, a) -plan, calculated (see. Eq. (2.3.4)) for a particle of optical index $n = 1.59$, and a distance $z = 15 \mu\text{m}$ between the particle center and the focal plane of the objective lens.

Finally, one can check how the holograms are varying with the optical index of a particle. In this case, it is not the particle's optical index n_p which matters the most but the ratio $\zeta = n_p/n_m$ which can be found in the a_n and b_n formulas, in Eqs.2.3.6 and 2.3.7. Indeed, for the scattering to happen, the optical index n_p of the colloid needs to be different from the optical index n_m of the surrounding medium. Additionally, the numerical solution of the Lorenz-Mie framework is not stable for $n_p \simeq n_m$. In Fig.2.3.5, we can observe holograms of a particle of radius $a = 1.5 \mu\text{m}$ at fixed distance $z = 15 \mu\text{m}$ between the particle and the focal plane of the objective lens with a varying colloid's optical index, in water where $n_m = 1.33$. In Fig.2.3.5, one can thus observe that for $n_p \simeq n_m$ we do not see any holograms. Additionally, one can observe that the signal-to-noise ratio gradually increases as n_p becomes different from n_m . One who wants to use this technique should thus have n_m different enough from n_p for the hologram intensity to be greater than the

camera noise level.

2.3.2 Summary on the Lorenz-Mie method

A given set of height, optical index and radius of a colloid thus gives unique holograms. Conversely, this uniqueness of the holograms permits precise extraction of the position, optical index and radius of a colloid. Holograms for different sets of parameters are shown in Figs. 2.3.7 and 2.3.8. Additionally, the interested reader can use the Jupyter Notebook on my Github repository in order to plot any hologram [Q](#).

Finally, the Lorenz-Mie framework provides the most versatile in-line holographic method. Indeed, it permits tracking and characterizing unique particles even without a priori knowledge on its characteristics. Besides, it is possible to write the Lorenz-Mie function \vec{f}_s for particular cases such as anisotropic particles [32, 33] or particle clusters [32, 34] to name a few. Such possibilities pave the way to a lot of experimental studies. Additionally, the method allows reaching a really high precision as the tenth of nanometers on the position and radius as well as 10^{-3} on the optical index [27].

Unfortunately, the Lorenz-Mie framework suffers from a major drawback which is the time needed to fit one image. For example, a 200 by 200 pixels image, of a $2.5 \mu\text{m}$ particle's hologram, can take up to two minutes to be fitted using a pure and straightforward Python algorithm. A lot of work has been done to permit faster tracking, such as random-subset fitting [35], GPU (graphical processing units) acceleration, machine learning [36, 37] and deep neural networks [38].

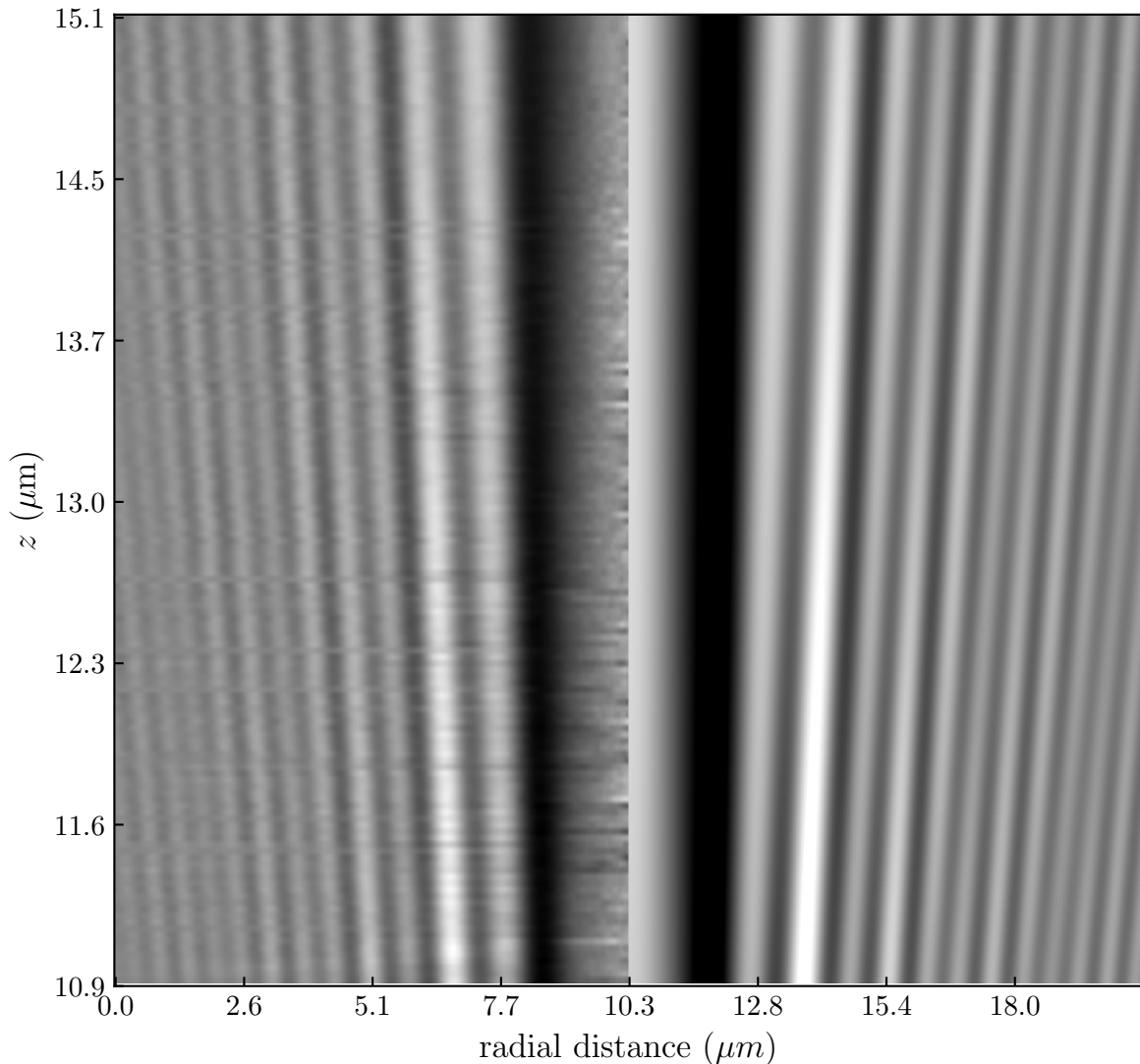


Figure 2.3.6: Hologram intensity map in the (r, z) -plan, calculated (see. Eq. (2.3.4)) for a particle of optical index $n = 1.59$, and radius $a = 1.51 \mu m$ using the experimental setup presented in the section 2.5. On the right, the corresponding theoretical intensity using the result of each individual hologram's fit to Eq. (2.3.5).

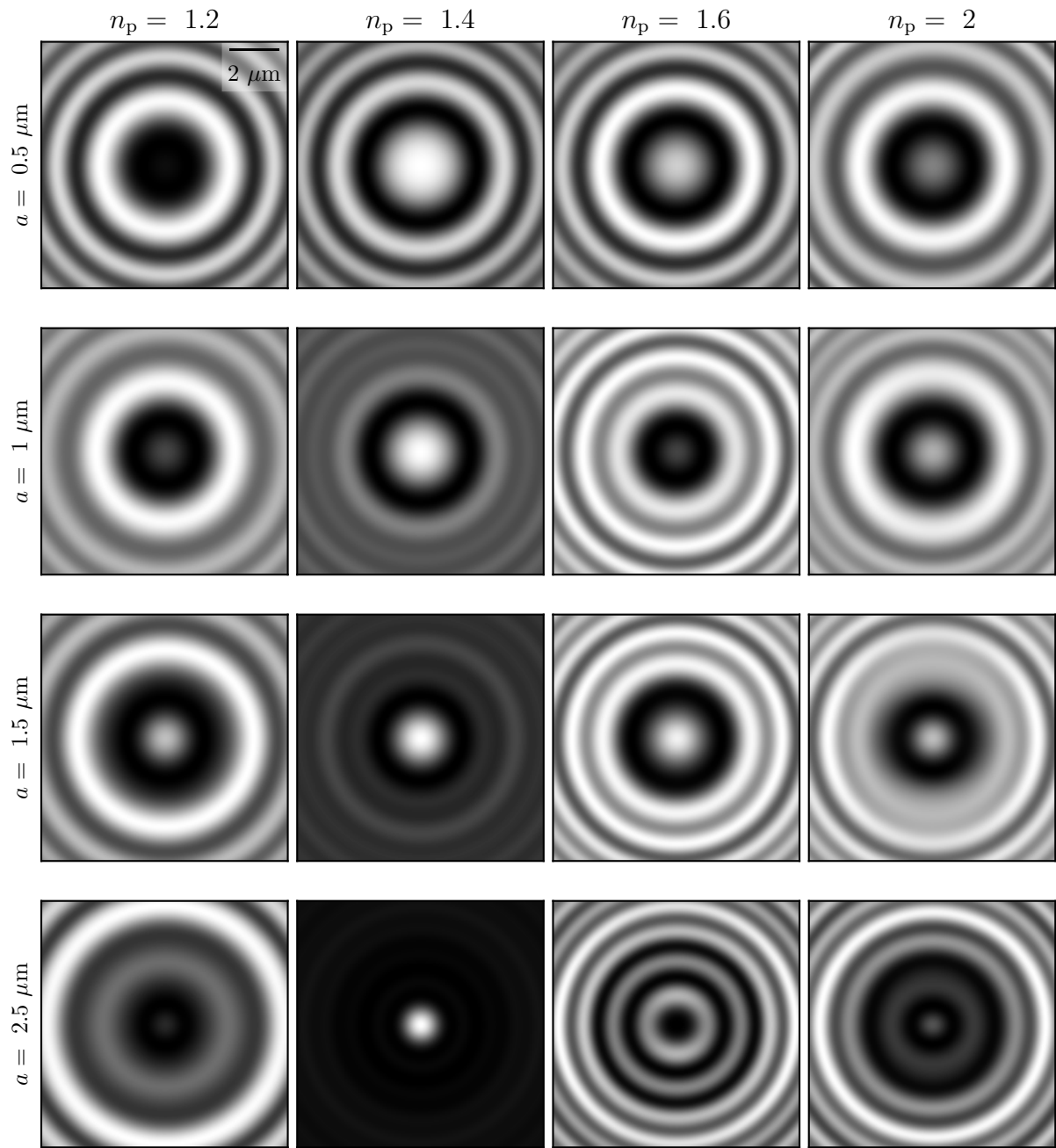


Figure 2.3.7: Holograms calculated (see. Eq. (2.3.4)) for different set of parameters (a , n_p), and for a distance $z = 15 \mu\text{m}$ between the particle center and the focal plane of the objective lens.

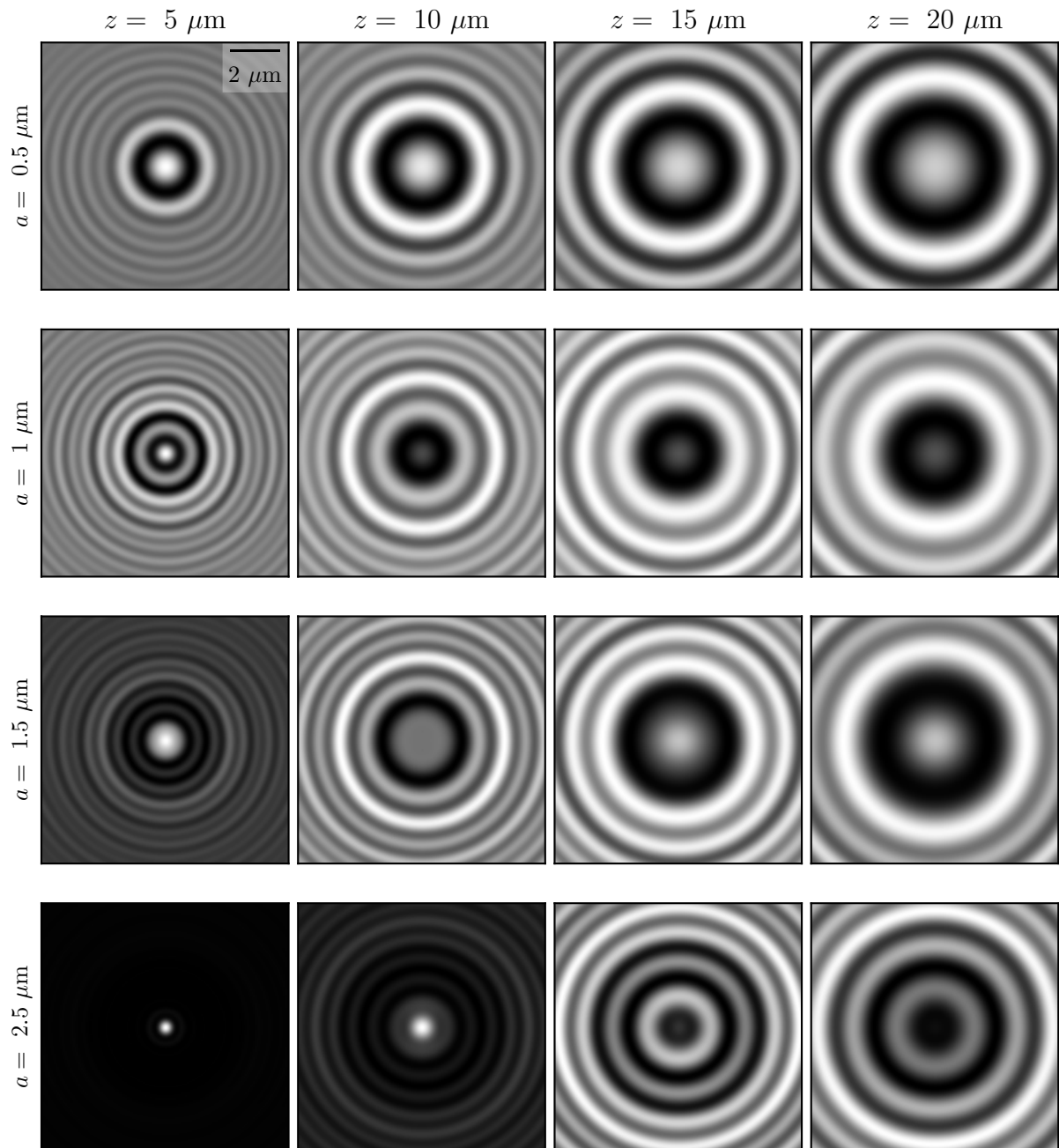


Figure 2.3.8: Holograms calculated (see. Eq. (2.3.4)) for different set of parameters (a , z), and for an optical index $n_p = 1.59$

2.4 Rayleigh-Sommerfeld back propagation

Rayleigh-Sommerfeld back propagation [39] works on the same principle as the Lorenz-Mie scattering but assumes small scatterers, and, a low difference of optical indices, such that:

$$|\zeta - 1| \ll 1 \text{ and } ka|\zeta - 1| \ll 1 . \quad (2.4.1)$$

In this case, at the focal plane, the intensity of the scattered field is smaller than the intensity of the incident field, hence, the term $|\vec{E}_s|^2$ can be ignored. Thus, the Eq. (2.3.4) can be rewritten as:

$$\frac{I(\vec{r})}{I_0(\vec{r})} = 1 + 2\Re \left(\frac{E_s(\vec{r}, 0)}{E_0(\vec{r})} \right) . \quad (2.4.2)$$

If one can retrieve the scattered field completely from an image, it is possible to reconstruct it above the focal plane by convolution using the Rayleigh-Sommerfeld propagator [40]:

$$h_{-z}(\vec{r}) = \frac{1}{2\pi} \frac{\partial}{\partial z} \frac{e^{ikR}}{R} , \quad (2.4.3)$$

where $R^2 = r^2 + z^2$ and the sign convention on the propagator indicates that the particle is above the focal plane. Using this propagator we have:

$$E_s(\vec{r}, z) = E_z(\vec{r}, 0) \otimes h_{-z}(\vec{r}) . \quad (2.4.4)$$

By using the convolution theorem [40–43] and supposing a uniform illumination, one can approximately reconstruct the scattered field at height z as:

$$E_s(\vec{r}, z) \approx f r a c e^{ikz} 4\pi^2 \int_{-\infty}^{\infty} B(\vec{q}) H(\vec{q}, -z) e^{i\vec{q}\cdot\vec{r}} d^2 q , \quad (2.4.5)$$

where $B(\vec{q})$ is the Fourier transform of I/I_0 and where:

$$H(\vec{q}, -z) = e^{iz\sqrt{k^2 - q^2}} . \quad (2.4.6)$$

Finally, using Eq. (2.4.5) one can reconstruct the scattered field and intensity since $I(\vec{r}) = |E_s(\vec{r})|^2$, as shown in Fig.2.4.1. Moreover, by finding the position where we have an inversion of the center from bright to dark in Fig.2.4.1, we measure the position of the particle. These equations are way less computationally expensive than Eq. (2.3.5). Thus tracking can be faster.

Additionally, as Eq. (2.4.5) takes only into account the intensity of the image, this method does not require any information on the particle and number of particles. As a matter of fact, to write Eq. (2.4.5), one just needs to assume that we have spherical colloids. Thus, this method is powerful to reconstruct the 3D position of a lot of particles or clusters. However, the Rayleigh-Sommerfeld back propagation suffers from being less precise of the presented methods and we cannot use it to characterize the particles generating the holograms.

2.4.1 Numerical Rayleigh-Sommerfeld back propagation

The `holopy` Python module provides a set of methods that permit implementing the Rayleigh-Sommerfeld back propagation. Given the `hologram` variable containing all the needed metadata about the hologram such as the pixel size, medium index n_n , illumination wavelength λ . Then, one can use the `propagate` method to back propagate a hologram over a set `zstack` of height using the following Python snippet.

```

1 import holopy as hp
2 import numpy as np
3
4 zstack = np.linspace(0, 20, 11)
5 rec_vol = hp.propagate(holo, zstack)
```

Note that using the `propagate` function, each propagation is done by performing a convolution of the reference hologram over the distance to be propagated. However, better reconstruction can be obtained iteratively by propagating holograms over several short distances. The latter method is called Cascaded Free Space Propagation, and is particularly useful when the reconstructions have fine features or when propagating over large distances [44]. It can be done by specifying the argument `cfsp` to the `propagate` method. For example, to change the source of the propagation every three steps, one can use `hp.propagate(holo, zstack, cfsp=3)`.

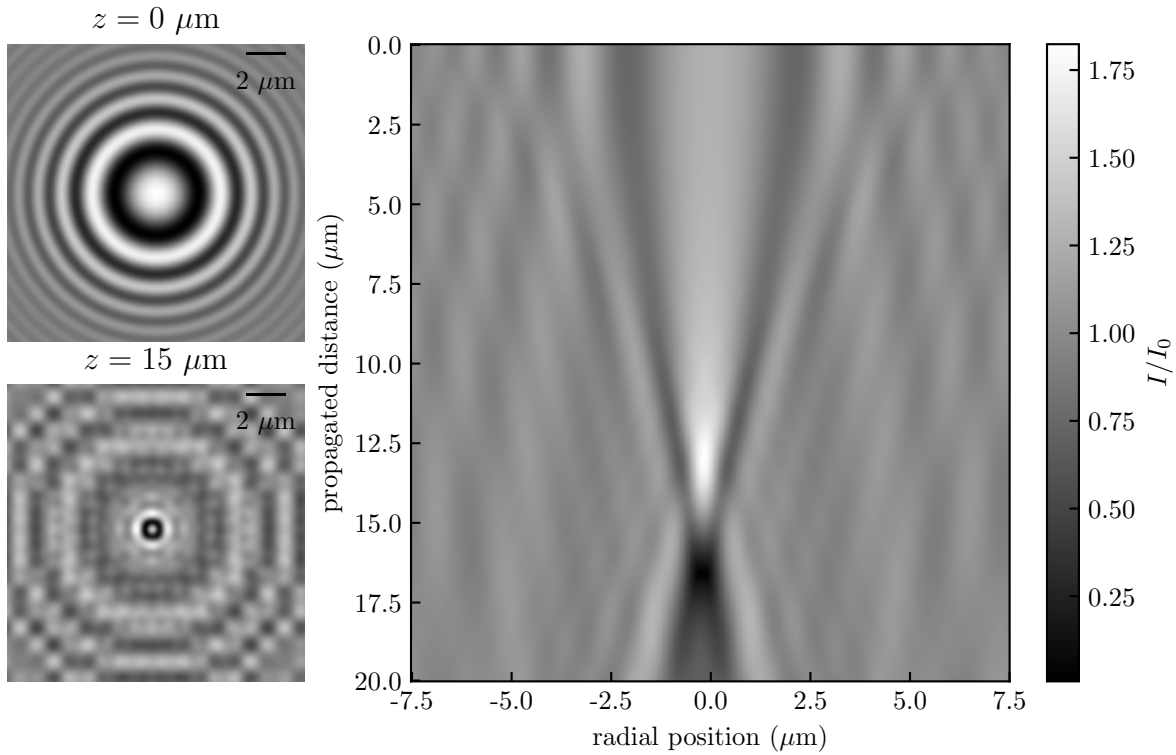


Figure 2.4.1: On the left: the original hologram on the top and propagated along $15 \mu\text{m}$ on the bottom. On the right: reconstruction using Eq. (2.4.5) of the scattered intensity by a single colloidal sphere of radius $a = 0.1 \mu\text{m}$, with optical index $n_p = 1.59$ in water whose index is $n_m = 1.59$, and for a height of $15 \mu\text{m}$.

2.5 The experimental setup

The experimental setup I developed during my PhD can be employed to implement both the Lorenz-Mie and Rayleigh-Sommerfeld back propagation methods. In order to observe the holograms, we use a homemade inverted microscope as shown in Fig.2.5.1 and schematized in Fig.2.5.2. This microscope is built using a ThorLabs cage system. Using the microscope, we observe the holograms resulting from the interactions between a laser source and the beads present in a sample.

A sample consists of a parallelepipedic chamber ($1.5 \text{ cm} \times 1.5 \text{ cm} \times 150 \mu\text{m}$), made from two glass covers, a parafilm spacer, and sealed with vacuum grease, containing a dilute suspension of spherical polystyrene beads. Sealing the sample with vacuum grease permits to drastically decrease evaporation, which reduces the possible evaporation driven-flow in the sample.

We used 3 different colloidal sizes, of nominal radii $0.56 \mu\text{m}$, $1.5 \mu\text{m}$ and $2.5 \mu\text{m}$, at room temperature T , in distilled water (type 1, MilliQ device) of dynamic shear viscosity $\eta = 1 \text{ mPa.s}$. The particles are made of polystyrene of density $\rho = 1050 \text{ kg.m}^{-3}$ and

optical index $n_p = 1.598$ at a wavelength of 532 nm.

The sample is illuminated by a collimated laser beam with a 532 nm wavelength. The laser used delivers a power of 4 W and has a centimetric waist. Since the laser is collimated, it has a near-zero exentricity so that it can be seen as a plane wave. As presented in the section 2.3, the light scattered, by one colloidal particle at a given time t , interferes with the incident beam.

An oil-immersion objective lens (x60 magnification, 1.30 numerical aperture) collects the resulting instantaneous interference pattern, and relays it to a camera (Basler acA1920-155um) with a 51.6 nm/pixel resolution (see Fig.2.3.1-a)). The exposure time of the camera is set to $\tau_{\text{expo}} = 3$ ms to avoid motion-induced blurring of the image. As a general rule, the particle should not diffuse more than the pixel size during that time, such that $\sqrt{2D\tau_{\text{expo}}} < 51.6$ nm.

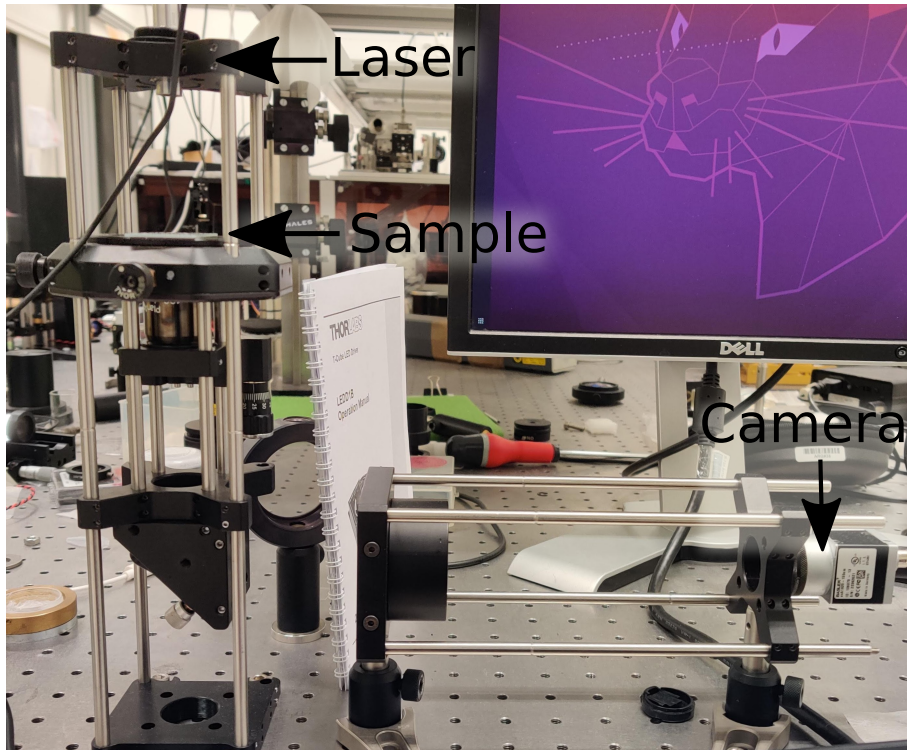


Figure 2.5.1: Photo of the custom-built microscope developed in my thesis. It is composed of a Thorlabs cage system. The camera used is a Basler acA1920-155um. We use a x60 magnification and 1.30 numerical aperture oil-immersion objective lens. The light source is a collimated 521 nm wavelength laser.

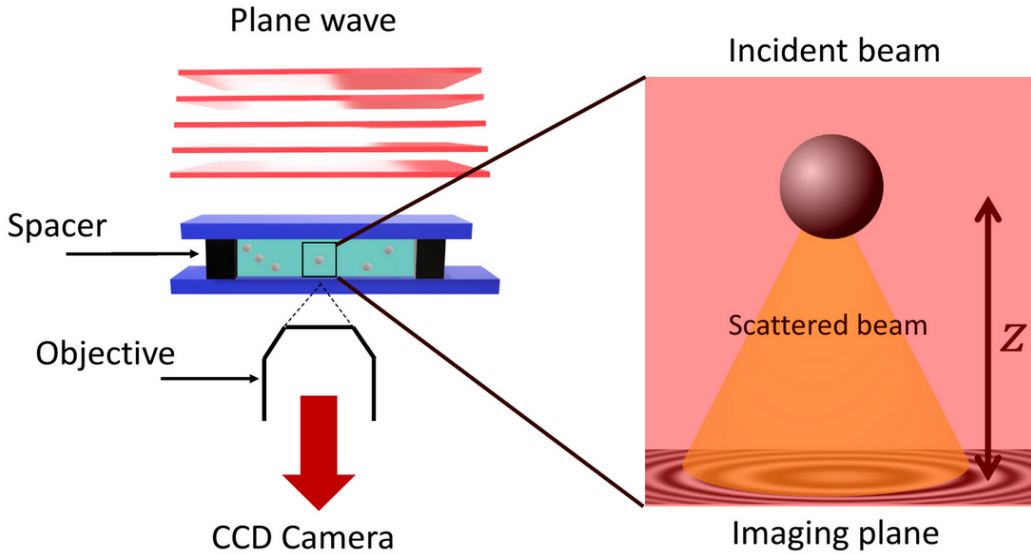


Figure 2.5.2: Schematic of the experimental setup. A laser plane wave of intensity I_0 illuminates the chamber containing a dilute suspension of microspheres in water. The light scattered by a particle interferes with the incident beam onto the focal plane of an objective lens, which magnifies the interference pattern and relays it to a camera.

2.6 Optical forces

As we illuminate particles with a laser, it is important to know if the optical forces that arise from the interactions between the light and the particle need to be taken into account. When a plane wave is incident on a sphere, it scatters and absorbs light. This process depends both on the light wavelength λ and on the sphere properties, its radius a and refractive index $n_p = n_r - jn_i$. For polystyrene $n_i \ll 1$, as shown in Fig.2.6.1 such that we neglect it in the Lorenz-Mie framework. However, computing the optical forces, and hence, the light quantity which is absorbed requires n_i , so we consider it this section. Additionally, in the Mie theory, the particle is characterized by the size parameter $\tilde{x} = 2\pi a/\lambda$. The optical force F_{opt} is given by [22]

$$F_{\text{opt}} = \frac{I_r n_m \pi a^2}{c} (Q_{\text{ext}} - g Q_{\text{sca}}) , \quad (2.6.1)$$

where I_r is the irradiance in W.m^{-2} on the sphere, c is the speed of light in vacuum, $g = \pi r^2$ the sphere cross section and Q_{ext} and Q_{sca} being respectively the extinction and scattering efficiency given by:

$$Q_{\text{ext}} = \frac{2}{k^2 a^2} = \sum_{n=1}^{\infty} (2n+1)(|a_n|^2 + |b_n|^2) , \quad (2.6.2)$$

and,

$$Q_{\text{ext}} = \frac{2}{k^2 a^2} = \sum_{n=1}^{\infty} (2n+1)\Re(a_n + b_n) , \quad (2.6.3)$$

where the a_n and b_n coefficient are given by the Eqs.2.3.6 and 2.3.7 respectively.

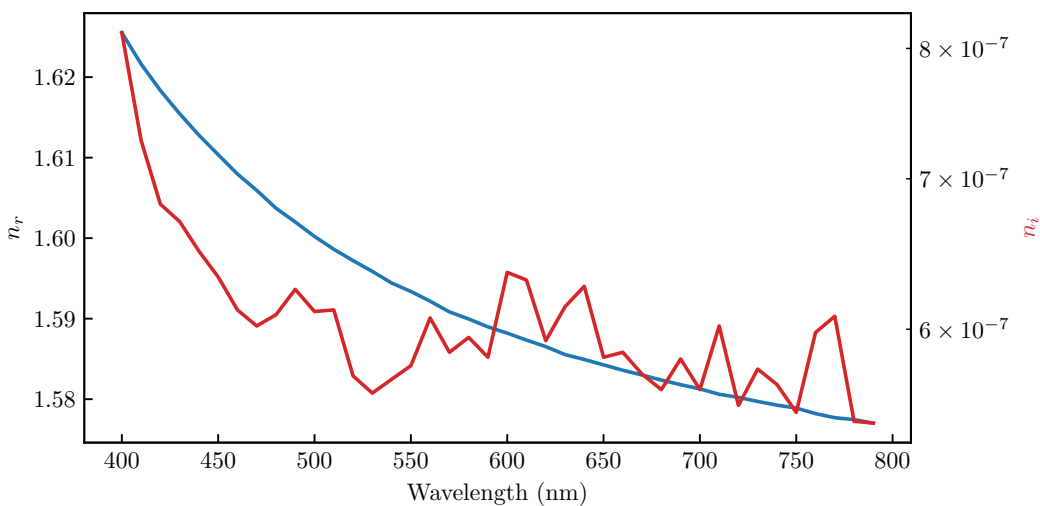


Figure 2.6.1: Real (left axis) and imaginary (right axis) part of the refractive index of polystyrene as a function of the incident wavelength. Data obtained from [45]

To compute the optical force I personally employ the `miepython` python's module and retrieving the optical index data from the refractiveindex.info website, using the following Python snippet.

```

1 import miepython as mp
2 import numpy as np
3
4 # Download the data on the refractiveindex.info website
5 poly = np.genfromtxt(
6     r"https://refractiveindex.info/tmp/data/organic/(C8H8)n%20-%20polystyren/Zhang.txt",
7     delimiter="\t",
8 )
9 N = len(poly) // 2

```

```

10 poly_lam = poly[1:N, 0] # wavelength
11 poly_nre = poly[1:N, 1] # real part
12 poly_nim = poly[N + 1 :, 1] # imaginary part
13
14 x = 2 * np.pi * a / poly_lam
15 n = poly_nre - 1.0j * poly_nim
16 qext, qsca, qback, g = mp mie(n, x) # compute the efficiencies
17 E0 = 4.5e-3 / (np.pi * 1.75e-3 ** 2) # compute the irradiience
18 c = 299792458 / 1.33 # light velocity in the medium
19
20 F = E0 * np.pi * r0 ** 2 * (qext - g * qsca) / c # compute the optical force

```

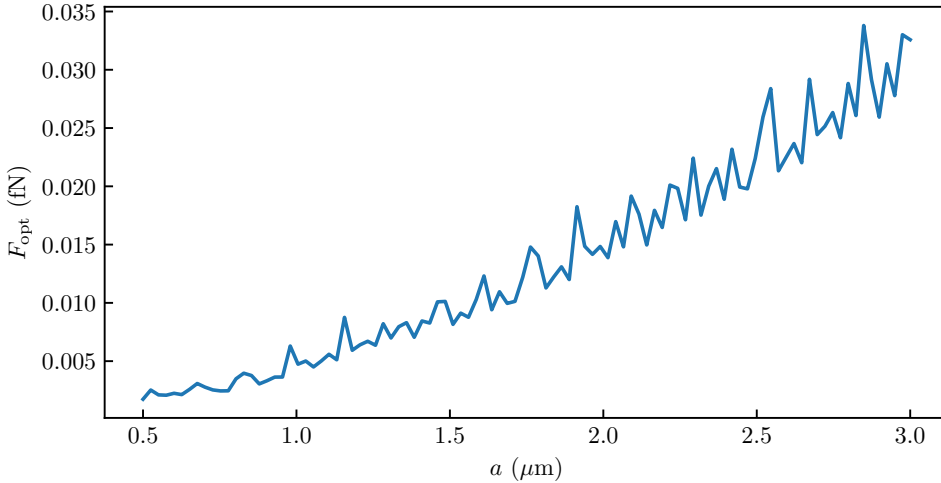


Figure 2.6.2: Optical force F_{opt} (see Eq. (2.6.1)) exerted on a spherical particle of radius a by a plane wave of wavelength $\lambda = 532$ nm, and of irradiance $I_r = 467.7 \text{ W.m}^{-2}$. The force is calculated employing the `miepython` python's module and the refractive index of polystyrene [45].

Using Python, one can thus compute the optical force F_{opt} as a function of the particle radius. As shown on Fig.2.6.2 the optical exerted on the colloidal particle from the microscope's illumination source is of the order of magnitude $F_{\text{opt}} \simeq 10^{-2}$ fN. By comparing this result with the buoyant of a colloidal particle F_g :

$$F_g = \frac{4}{3}\pi(\rho_m - \rho_p)g , \quad (2.6.4)$$

we found that for a particle of radius $a = 0.5 \mu\text{m}$, $F_g = -0.3 \text{ fN}$ and for $a = 1.5 \mu\text{m}$, $F_g = -7 \text{ fN}$. Thus, we can conclude that $F_{\text{opt}} \ll F_g$, hence, in the following of the manuscript we neglect the optical force as it is lower than the other external forces acting

on the colloids. However, experiments with a controlled irradiance (up to 10^6 W.cm^{-2}) and they were able to measure the optical force from the motion statistics [46].

2.7 The experimental procedure

We implement here the Lorenz-Mie fitting method, since it permits the characterization of single particles. Indeed, since we are interested in fine effects near surfaces, we require to know perfectly the radius of the tracked particle. This feature also makes our whole procedure calibration-free, as we do not need to assume any physical properties. An example of the procedure that permits tracking a single-particle trajectory is provided in appendix ???. In the following, the different steps of the procedure are described.

2.7.1 Recording the holograms

Since we use a Basler camera, we use the provided computer program (Pylon) by the manufacturer in order to record the holograms. The software permits adjusting the parameters of the camera, such as the region of interest (ROI), number of frames per second (fps) or the opturation time to name a few. Also, video can be recorded as a time series of images, in AVI or MP4 formats. AVI files or times series are a great way to save the video since it is lossless. However, in general, we use a ROI of 1000×1000 pixels to record the particle during a long-enough time.

Additionally, since the recording is done using 8 bits per pixel (or 256 gray levels), an image of 1000×1000 pixels needs a disk space of 1 MB². One can see that image sequences and AVI files are not suitable for our case because i) at 100 fps one would need 108 GB to store a 30-minute film, which would lead to several TB of data per experiment which is not manageable; ii) it would require a sequential writing speed of 60 MB/s, which is just below the limit of the better Hard Drive Disks. iii) AVI files are bound to 2 GB maximum thus dramatically reducing the length of the experiments.

To conclude, for all of these reasons, we chose to use the MP4 file format (MPEG-4 encoding) for the video recording. Using the lowest compression, we did not observe any impact on the fitting process due to quality loss. Finally, a video of 30 minutes has an approximate size of 3 GB.

² An uppercase B denotes Byte which is equivalent to 8 bits denoted by b , *i.e.* $1 \text{ B} = 8 \text{ b}$. For storage indications, Bytes are generally used, since historically a set of 8 bits encodes a single text character, and are for this reason the smallest addressable memory units in most computer architectures. As an example, in binary “LOMA” would be encoded by “01001100 01001111 01001101 01000001.”

2.7.2 Fitting the holograms

Once the holograms are recorded, we fit all of the images to retrieve the trajectory of the particle. To do so, we chose to use the `pylorenzmie` module developed by the Grier's lab at New York University. Although this module presents a lot of capabilities, it is not adapted to MP4 input. Thus, I developed a wrapper³ around `pylorenzmie` that I called Wraplorenzmie which can be found on my Github repository [Q](#).

This wrapper permits to directly load the MP4 files, compute the background and choose if what parameters should be fitted. Also, it manages the process fitting a time series of images by using results of previous image as initial fit parameters.

However, as presented in the section 2.3, the main drawback is the time to fit an image. Indeed, using a Python algorithm, one needs 30 seconds to fit images of 100×100 pixels and a few minutes for a 500×500 pixels hologram. We can directly see a bottleneck, if one wants to track one trajectory made of 100 000 images .In such case, one would need to typically 70 days for a series of images that needs only a few minutes to be recorded experimentally.

When I started my PhD, two groups, the Grier's lab and the Manoharan's lab, had already created Python packages, respectively Pylorenzmie and Holopy, in order to inverse holograms. They had introduced ways to only fit a set of randomly chosen pixels, and demonstrated that taking only 1 % of the image pixels, could lead to similar precision thus improving considerably the fit's execution time [35].

Unfortunately, even if fitting a random subset of pixels is faster, it leads to a few images per second, and is still too long for the amount of data we want to have. This part of my thesis is certainly the one where I spent the longest time, and I learned a lot about code optimization and computer cluster usage.

In the middle of my thesis, `pylorenzmie` got a new commit⁴ on the authors' Github repository which was saying that the authors succeeded in using GPU acceleration with CUDA⁵. This was not an easy task since they needed to reconstruct the Bessel functions

³ A wrapper is a code that encapsulates or “wraps” another code to make it easier to use. For example, it is particularly useful to adapt a program to a particular type of input data. Creating wrapping function is a commonly done by developers add some abstraction to the source codes and readability.

⁴ A commit is an update of the files on a Git repository.

⁵ CUDA is the acronym of Compute Unified Device Architecture. It is a parallel computing platform, and programming model made to permit an easier use of the GPU for general purposes. CUDA is developed by NVIDIA since 2012, thus all recent NVIDIA's GPUs are CUDA-enable. It is possible to use CUDA with every language as long as a library has been developed, such as `cupy`for Python [Q](#).

in an understandable way for the GPU. Fortunately, it is possible to do so by using continued fractions [31]. This appreciable update permits fitting whole images with a speed improvement of 20 fps. At this speed, we precisely extract the tridimensional position of the particle, as well as the radius and optical index.

As a remark, the fits are done by solving a least-squares problem using the Levenberg-Marquardt algorithm [47]. This algorithm is largely used in curve-fitting applications due to its capabilities to find a minimum even by starting far from it. As mentioned, it is also possible to use various models of Machine Learning or Deep Learning to do the fits [38]. However, since we can write analytically the holograms, the Deep Learning's models cannot be more accurate than a standard least-square-fitting process. Deep Learning, however, could be a great option if one wanted to prioritize the computation time over the fit's precision.

Finally, to have a more reliable and fast-tracking, we begin by fitting the first 10 000 images with \vec{r}_p , a and n_p as free parameters. Using the results of this fit, we can characterize the physical properties of the tracked colloid with high precision. Then, using these results we can then fit image with only the position \vec{r}_p as a free parameter.

2.7.3 Radius and optical index characterization

Using 10 000 measurements of a and n_p one can do a 2D histogram, as presented in Fig.2.7.1 here smoothed using a Gaussian Kernel Density Estimator. Doing so, we determine that the radius of the observed particle is $a = 1.514 \pm 0.003 \mu\text{m}$ and its optical index is $n_p = 1.585 \pm 0.002$.

Finally, as explained above, using this measurement of the radius and optical index, we then fit the whole video by removing them from the free parameters. Doing so, we measure the 3D trajectory of the particle as shown in Fig.2.7.2 in tridimension for the particle previously characterized.

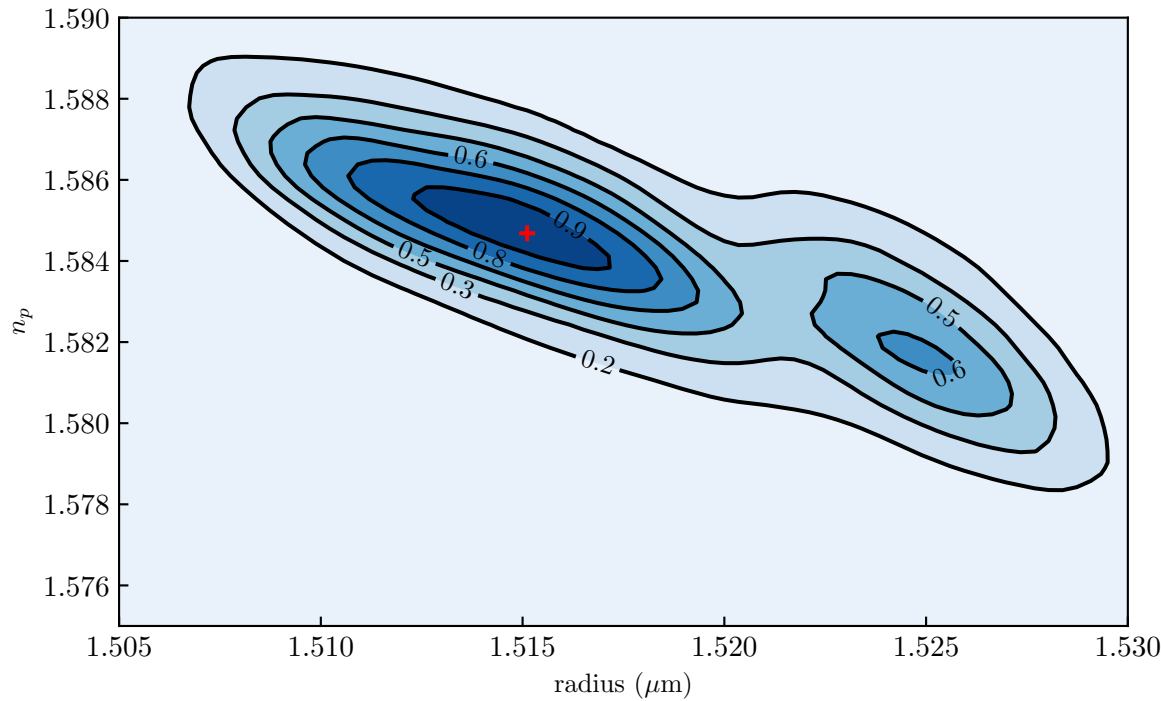


Figure 2.7.1: 2D Probability density function of the measurements of the optical index n_p and radius a . Black lines indicate iso-probability. Taking the 10% top probability, we measure $n_p = 1.585 \pm 0.002$ and $a = 1.514 \pm 0.003 \mu\text{m}$.

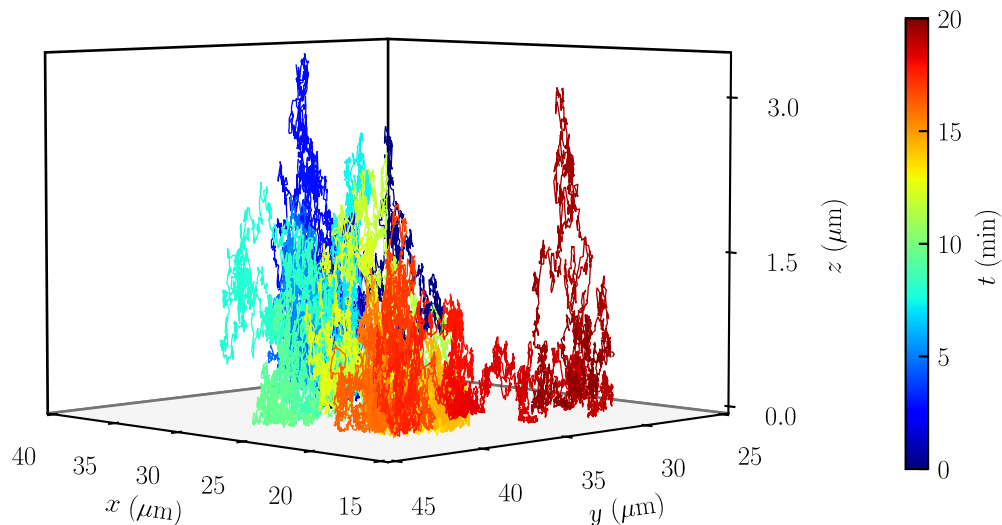


Figure 2.7.2: 3D plot of an experimental trajectory measured in water for a particle of optical index $n_p = 1.585$ and radius $a = 1.514 \mu\text{m}$.

2.7.4 Conclusion

In this chapter, we have covered different techniques that enable the tracking of individual microparticles. Each method has pros and cons. We decided to employ the Lorenz-Mie framework since it requires no calibration. Then, we have shown how we implement it in practice, from the experimental setup to the numerical treatment. An example of the Jupyter notebooks employed for the tracking can be found in appendix ???. We have discussed how to have fast and accurate fits to retrieve the particle trajectory. To do so, we first characterize the particle fully, namely, its radius and optical index, analyzing solely the trajectory over before tracking a whole video.

Now that we have an understanding on the tracking of single colloids, we can use the measured trajectories in order to understand how the Brownian motion is affected in various configurations.

3 Stochastic Inference of Surface-Induced Effects Using Brownian Motion

3.1 Confined Brownian motion theory

By observing the experimental trajectory along the z -axis of a particle of $1.5 \mu\text{m}$ radius as shown in Fig. 3.1.1, one can notice that the particle's height does not get higher than approximately $4 \mu\text{m}$. Indeed, due to gravity, a colloid is confined near the surface. This confinement induces near-wall effects, such as hindered mobility and electrostatic interactions.

In the first part of this chapter, I will detail the theory of confined Brownian motion and how to numerically simulate it. In a second part, I will present how to analyze experimental data. In particular, I will detail a multi-fitting procedure that enables thermal-noise-limited inference of diffusion coefficients spatially resolved at the nanoscale, equilibrium potentials, and forces at the femtonewton resolution.

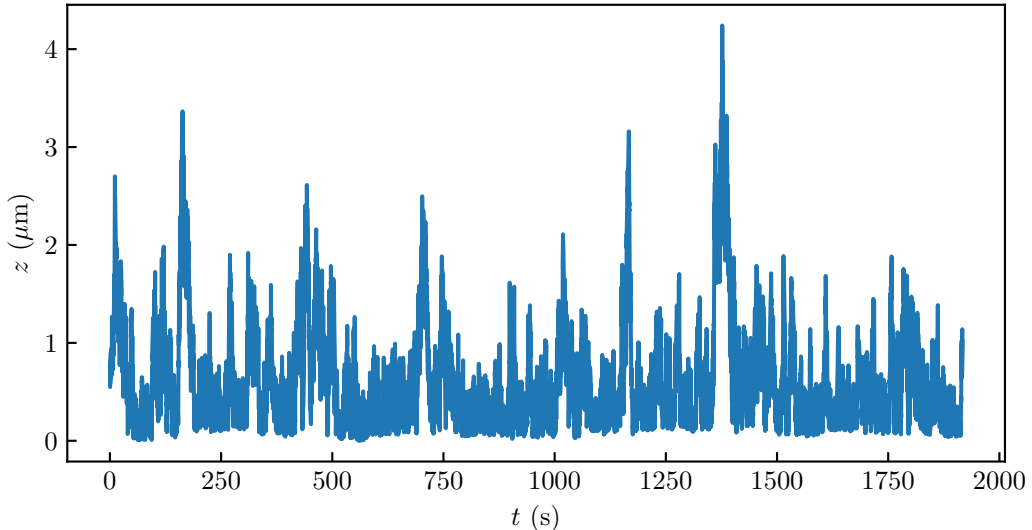


Figure 3.1.1: Experimental trajectory of a polystyrene particle of radius $a = 1.5 \mu\text{m}$ in water near a glass wall ($z = 0$) along the z -axis — *i.e* perpendicular to the wall.

3.1.1 Gravitational potential

The density ρ_p of an observed colloid is different from the medium density ρ_m . In our experiment, we used water whose density is $\rho_m = 1000 \text{ kg.m}^{-3}$. Thus, the particles are

subject to gravitational potential given by:

$$U_g(z) = \Delta m g z = \frac{4}{3} \pi a^3 g \Delta \rho z , \quad (3.1.1)$$

where Δm is the difference between the mass of the particle and that of a fluid sphere of the same size, $\Delta \rho = \rho_m - \rho_p$ is the corresponding density difference, and g is the gravitational acceleration. By invoking the definition of the Boltzmann length:

$$\ell_B = \frac{k_B T}{(4/3)\pi a^3 \Delta \rho g} , \quad (3.1.2)$$

one can rewrite Eq. (3.1.1) as:

$$U_g(z) = \frac{k_B T}{\ell_B} z . \quad (3.1.3)$$

The Boltzmann length ℓ_B corresponds to the spatial extent over which the change of gravitational energy equals thermal energy. This distance was first measured by Perrin [48]. To do so, using a microscope he counted the number of colloidal particles as a function of the height in the sample. Then, he reconstructed the concentration profile of the colloidal suspension that exponentially decays as e^{-z/ℓ_B} . As an example, for a polystyrene particle of radius $a = 1.5 \mu\text{m}$ in water, one has $\ell_B = 580 \text{ nm}$.

For systems with $\ell_B \gg h$, where h is the vertical thickness of the sample, one can consider that the particle does not feel gravity. This is particularly the case when the densities of the colloids and the fluid are equal. In this particular case, one has $\ell_B = \infty$. Thus, density matching can be a way to do gravity-free experiments. In our experiment, we want to measure confinement-induced effects. Therefore, we need gravity for particles to be driven towards the substrate. As particles get larger or denser, ℓ_B decreases and particles are, on average, closer to the substrate.

3.1.2 Sphere-wall interactions

As we have seen, external forces such as gravity act on the particles. As Brownian particles are close to a wall, we can also expect some interactions between the particles and the wall. In our case, we suppose that the Brownian particles do not interact with each other,

as we consider dilute solutions only. Indeed, the studied particles are at least $50 \mu\text{m}$ apart from each other, which corresponds to 10 times their size for the largest beads.

To describe the interaction between a Brownian particle and the wall, we use the DLVO theory, named after Derjaguin, Landau, Verwey, and Overbeek [49]. This theory was first developed to describe the interactions between colloids, and explains the stability of colloidal suspensions. It involves two force components; the Hamaker force which arises from van der Waals interactions between the molecules of the two surfaces and a screened electrostatic force due to a double layer of charges formed near each surface, and involving the ions present in the solution.

3.1.2.1 Double layer interactions

When a surface is immersed in water, it usually acquire charges [49] due to a high water dielectric constant $\epsilon = \epsilon_0\epsilon_r$, where ϵ_0 is the vacuum permittivity and ϵ_r the medium relative permittivity; for water $\epsilon_r = 80$. Commonly, surface charging is done through the ionization of surface groups⁶, or from the binding of ions from the solution — for example, adsorption of $-\text{OH}^-$ onto the water-air interface that charges it negatively. In the bulk, a fluid is electrically neutral; thus the fluid contains as equal number of ions of opposite charges (including the proper stoichiometry due to ionic valencies). However, when a surface is negatively charged, the negative ions are repelled from it, while positive ions are attracted towards it. Therefore, a double-layer charge distribution is formed near the surface, as shown in Fig. 3.1.2. Experimentally, we use glass slides and polystyrene beads that are both negatively charged in water leading to a repulsive interaction between them. This repulsive force prevents the colloids from sticking together, or to the substrate's surface.

The DLVO theory state that the electrostatic potential $\Psi(\vec{r})$ generated by an ion of one given species i at a distance \vec{r} satisfies the Poisson equation [49]:

$$\nabla^2\Psi(\vec{r}) = -\frac{1}{\epsilon_r\epsilon_0}\rho_e(\vec{r}) , \quad (3.1.4)$$

with:

⁶ For example, the dissociation of protons from surface carboxylic groups [49] ($-\text{COOH} \rightarrow -\text{COO}^- + \text{H}^+$) which charges negatively the surface.

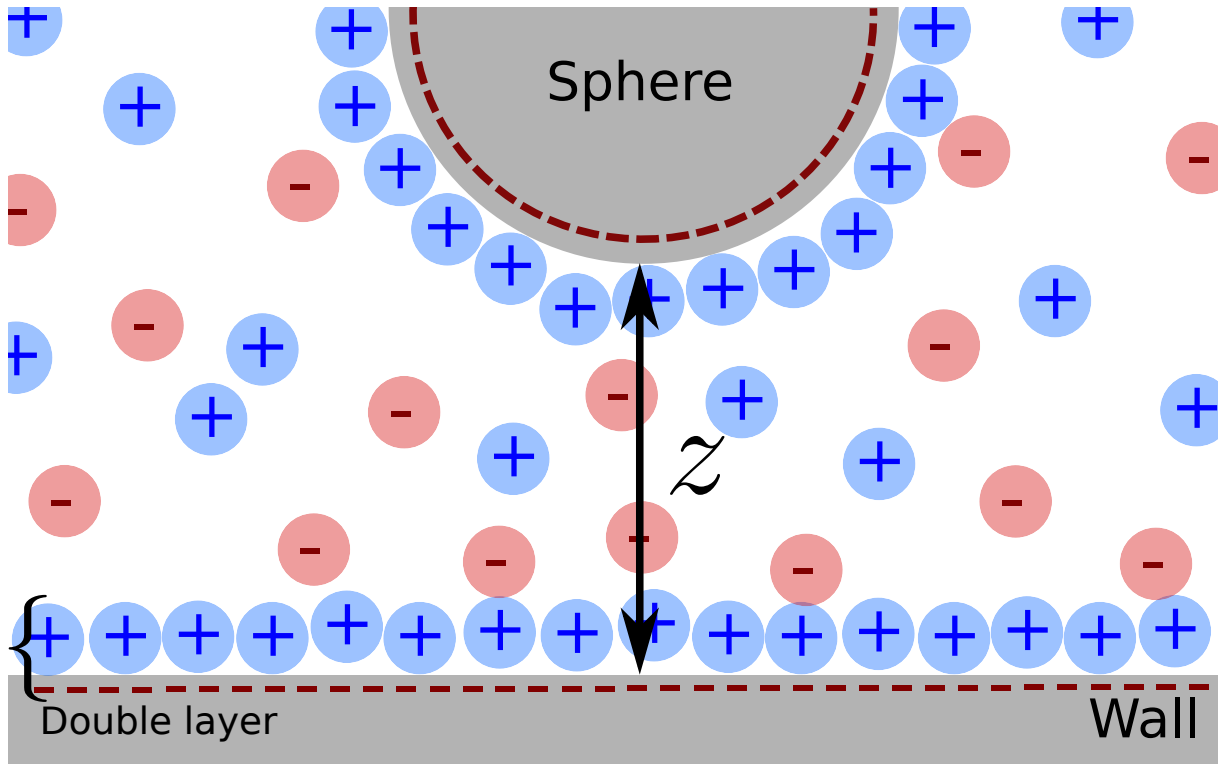


Figure 3.1.2: A colloid diffusing near a wall. Both the wall and colloid surfaces charge negatively. As a consequence, a layer of positively-charged ions is attracted towards each surface, forming a double layer.

$$\rho_e(\vec{r}) = e \sum_i z_i c_i(\vec{r}) , \quad (3.1.5)$$

the local charge density, where e is the elementary charge, and where the index i denotes an ionic species of valence z_i and local ionic concentration c_i (number density). If the solution is at thermodynamic equilibrium, the local ionic density is given by a Gibbs-Boltzmann distribution, as:

$$c_i(\vec{r}) = c_i^0 \exp\left(\frac{-z_i e \Psi(\vec{r})}{k_B T}\right) , \quad (3.1.6)$$

where c_i^0 is the bulk concentration (number density) of the ionic species i . By combining Eqs. (3.1.4), (3.1.5) and (3.1.6), one obtains the Poisson-Boltzmann equation:

$$\nabla^2 \Psi(\vec{r}) + \sum_i \frac{z_i e c_i^0}{\epsilon_0 \epsilon_r} \exp\left(-\frac{z_i e \Psi(\vec{r})}{k_B T}\right) = 0 . \quad (3.1.7)$$

Since Eq. (3.1.7) is nonlinear, it is typically solved numerically. However, for some simple configurations such as uniformly-charged plane or sphere it can be solved analytically. To simplify, let us consider that we have a monovalent electrolyte, meaning that the electrolyte is composed of two ions of valencies both equal to 1 — Na^+ Cl^- for example — and c_i^0 is equal to the bulk electrolytic concentration c_s^0 . In such a case, Eq. (3.1.7) simplifies and becomes:

$$\begin{aligned}\nabla^2\Psi(\vec{r}) + \frac{ec_s^0}{\epsilon_0\epsilon_r} \left[\exp\left(\frac{-e\Psi(\vec{r})}{k_B T}\right) - \exp\left(\frac{+e\Psi(\vec{r})}{k_B T}\right) \right] &= 0 \\ \nabla^2\Psi(\vec{r}) + 2\frac{ec_s^0}{\epsilon_0\epsilon_r} \sinh\left(\frac{e\Psi(\vec{r})}{k_B T}\right) &= 0.\end{aligned}\quad (3.1.8)$$

Another situation leading to analytical results, is when Ψ is small enough such that $e\Psi \ll k_B T$, which is generally the case when using dilute enough solutions, it is possible, through a Taylor expansion at first order to write:

$$\exp\left(-\frac{z_i e \Psi(\vec{r})}{k_B T}\right) \simeq 1 - \frac{z_i e \Psi(\vec{r})}{k_B T}. \quad (3.1.9)$$

In such case, Eq. (3.1.7) becomes:

$$\nabla^2\Psi(\vec{r}) + \sum_i \frac{z_i e c_i^0}{\epsilon_0\epsilon_r} \left(1 - \frac{z_i e \Psi(\vec{r})}{k_B T}\right) = 0. \quad (3.1.10)$$

In addition, a fluid is electrically neutral. Therefore, $\sum_i z_i c_i^0 = 0$. Thus, one can simplify Eq. (3.1.10) to get the Debye-Hückel equation:

$$\nabla^2\Psi(\vec{r}) = \left[\sum_i \frac{z_i^2 e^2 c_i^0}{\epsilon_0\epsilon_r k_B T} \right] \Psi(\vec{r}). \quad (3.1.11)$$

One can identify the term between brackets as the inverse of a length squared. We thus define the Debye length as:

$$\ell_D = \sqrt{\sum_i \frac{\epsilon_0\epsilon_r k_B T}{z_i^2 e^2 c_i^0}}, \quad (3.1.12)$$

which is the characteristic ion-induced screening length of the electrostatic interactions, as we will see below. For a monovalent electrolyte, at 25 °C, the Debye length of an aqueous solution is:

$$\ell_D = \sqrt{\frac{2\epsilon_0\epsilon_r k_B T}{c_s^0 e^2}} = \frac{0.304}{\sqrt{C}} \text{ nm} , \quad (3.1.13)$$

with C the value of the molar concentration in mol.L⁻¹:

$$C = \frac{c_s^0}{N_A} 10^{-3} . \quad (3.1.14)$$

For example, for NaCl salt in water, $\ell_D \approx 100$ nm for a concentration $C = [\text{NaCl}] = 9.2 \mu\text{mol.L}^{-1}$ and $\ell_D \approx 10$ nm for a concentration $[\text{NaCl}] = 9.2 \text{ mmol.L}^{-1}$.

Finally, combining Eqs. (3.1.11) and (3.1.12), the Debye-Hückel equation reads:

$$\nabla^2 \Psi(\vec{r}) = \kappa^2 \Psi(\vec{r}) , \quad (3.1.15)$$

with $\kappa = 1/\ell_D$. Using the latter, one can compute the electrostatic potential around a sphere immersed in an ionic solution. Let us consider a sphere of radius a and charge Qe , *i.e.* a charge density $\sigma = Qe/(4\pi a^2)$, Q being the number of charges on the surface. Since the system has a spherical symmetry, one has $\Psi(\vec{r}) = \Psi(r)$ with $r = |\vec{r}|$. Using the Laplacian operator ∇^2 in spherical coordinates, Eq. (3.1.15) becomes:

$$\frac{1}{r^2} \left[\frac{\partial}{\partial r} \left(r^2 \frac{\partial \Psi(r)}{\partial r} \right) \right] = \kappa^2 \Psi(r) , \quad (3.1.16)$$

which has a general solution:

$$\Psi(r) = C_1 \frac{\exp(\kappa r)}{r} + C_2 \frac{\exp(-\kappa r)}{r} . \quad (3.1.17)$$

The electrostatic potential vanishes at infinity such that $C_1 = 0$. Therfore, the electrostatic potential (and thus the electrostatic energy potential) takes the form of a Yukawa potential:

$$\Psi(r) = C_2 \frac{\exp(-\kappa r)}{r} . \quad (3.1.18)$$

Additionally, invoking the Gauss theorem, at the surface of the charged sphere, the electrostatic potential satisfies:

$$\left. \frac{\partial \Psi(r)}{\partial r} \right|_{r=a} = \frac{-Qe}{4\pi\epsilon_0\epsilon_r a^2} = \frac{-\sigma}{\epsilon_0\epsilon_r} , \quad (3.1.19)$$

where we introduced the surface density of charges σ . By applying the latter boundary condition to Eq. (3.1.18), we find:

$$\Psi(r) = \frac{\sigma a^2}{\epsilon_0\epsilon_r} \frac{\exp(\kappa a)}{1 + \kappa a} \frac{\exp(-\kappa r)}{r} . \quad (3.1.20)$$

This solution can be used to determine the electrostatic potential between two spheres of radii a_1 and a_2 , and surface charge densities σ_1 and σ_2 , respectively. Supposing that the presence of a second sphere does not modify the distribution of ions in the double layer of the other sphere, one can use the superposition approximation to obtain the potential $U_{\text{elec}}^{ss}(z)$ between the two spheres [50]:

$$U_{\text{elec}}^{ss}(z) = \frac{4\pi}{\epsilon_0\epsilon_r} \left(\frac{\sigma_1 a_1^2}{1 + \kappa a_1} \right) \left(\frac{\sigma_2 a_2^2}{1 + \kappa a_2} \right) \frac{\exp(-\kappa z)}{a_1 + a_2 + z} , \quad (3.1.21)$$

with z the gap between the two colloids. From the latter equation, it is possible to write the electrostatic interaction energy U_{elec} between a planar wall of charge density σ_w and a spherical colloid of radius a and surface charge density σ , by setting one of the two radii to infinity. Doing so, one gets:

$$\frac{U_{\text{elec}}(z)}{k_B T} = B e^{-\frac{z}{\ell_D}} , \quad (3.1.22)$$

where:

$$B = \frac{4\pi}{k_B T \epsilon_0 \epsilon_r} \left(\frac{\sigma a^2}{1 + \kappa a} \right) \frac{\sigma_w}{\kappa} . \quad (3.1.23)$$

Let us note that, B is often written as [51]:

$$B = 16\epsilon_r\epsilon_0 a \frac{k_B T}{e^2} \tanh\left(\frac{e\phi}{4k_B T}\right) \tanh\left(\frac{e\phi_w}{4k_B T}\right), \quad (3.1.24)$$

where ϕ and ϕ_w are the Stern potentials of the sphere and wall surface, respectively. Typical values for B range from 1 to 50. In our study, we will use B to characterize the dimensionless magnitude of the electrostatic interaction. Indeed, it is complicated to decouple σ and σ_w when the colloid and wall materials are different [51].

3.1.2.2 van der Waals interactions

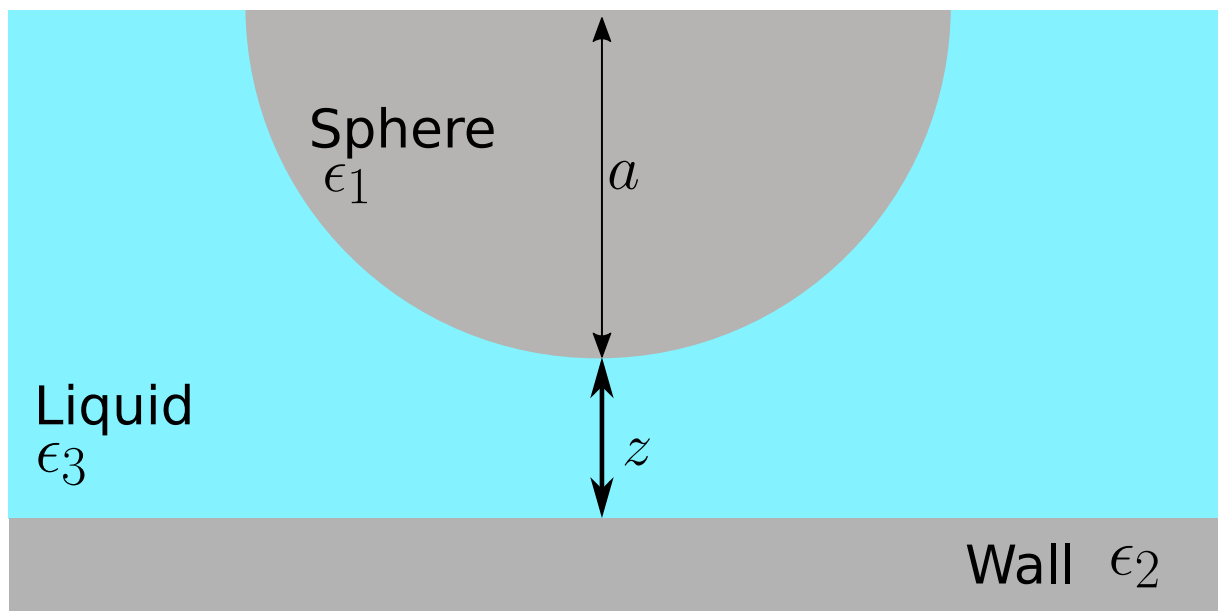


Figure 3.1.3: A colloid of radius a is located at a distance z from the wall. The dielectric constants of the sphere, wall and liquid are respectively ϵ_1 , ϵ_2 , and ϵ_3 .

In the DLVO theory, van der Waals interactions, after integration over all surfaces contribute through a global Hamaker potential energy. This potential is short-ranged and attractive, in our case. The interaction potential reads: [49]:

$$U_{\text{vdW}} = -\frac{Aa}{6z} \quad (3.1.25)$$

where A is the nonretarded Hamaker constant. For our system, where the particle, medium and wall are different media as schematized in Fig. 3.1.3, the Hamaker constant is given by [49]:

$$A = \frac{3}{4}k_B T \left(\frac{\epsilon_1 - \epsilon_3}{\epsilon_1 + \epsilon_3} \right) \left(\frac{\epsilon_2 - \epsilon_3}{\epsilon_2 + \epsilon_3} \right) + \frac{3h}{4\pi} \int_{\nu_1}^{\infty} \left(\frac{\epsilon_1(j\nu) - \epsilon_3(j\nu)}{\epsilon_1(j\nu) + \epsilon_3(j\nu)} \right) \left(\frac{\epsilon_2(j\nu) - \epsilon_3(j\nu)}{\epsilon_2(j\nu) + \epsilon_3(j\nu)} \right) d\nu , \quad (3.1.26)$$

where ϵ_1 , ϵ_2 and ϵ_3 are the static dielectric constants of the three media, $\epsilon_{1,2,3}(j\nu)$ are the dielectric constant at a imaginary frequency $j\nu$. The first term gives the zero-frequency energy of the Van der Waals interaction and the second term the dispersion energy. In the litterature, we found for polystyrene colloids in water near a glass substrate $A \approx k_B T$. Since A is positive, the interaction is attractive, moreover, we estimate that the van der Waals forces play a role only within a few nanometers from the surface ($z < 10$ nm), as commonly observed [46]. In our experiments, the Debye length ℓ_D (> 20 nm) is large enough for the particles to avoid this region. Therefore, in the following, the van der Waals interactions are neglected. It is possible to study the van der Waals interactions with Brownian motion, provided that one adds enough salt to have $\ell_D \simeq 1$ nm. However, with such a short Debye length, all the colloids would stick to the surface and with each others, as a result of van der Waals forces. Interestingly, we have experimentally observed stuck particles. Further work on these events may lead to interesting insights about of the near-wall interactions.

3.1.2.3 Total potential and equilibrium distribution

If we combine the gravitational and electrostatic energy potentials the particles lie into a total energy potential $U(z)$, given by:

$$U(z) = U_g + U_{\text{elec}} . \quad (3.1.27)$$

By combining Eqs. (3.1.3), (3.1.22) and (3.1.27), and adding the condition that a particle cannot go inside the wall, one finally gets:

$$\frac{U(z)}{k_B T} = \begin{cases} B e^{-\frac{z}{\ell_D}} + \frac{z}{\ell_B} , & \text{for } z > 0 \\ +\infty , & \text{for } z < 0 \end{cases} . \quad (3.1.28)$$

From this total potential energy, one can then construct the Gibbs-Boltzmann distribution to write the equilibrium PDF of position $P_{\text{eq}}(z)$:

$$P_{\text{eq}}(z) = A \exp\left(-\frac{U(z)}{k_B T}\right), \quad (3.1.29)$$

where A is a normalization constant such that $\int_0^\infty P_{\text{eq}}(z)dz = 1$. Given an ensemble of heights z_i , one can compute P_{eq} using the following Python function `Peq`, where the A is computed using the `np.trapz` function. Examples of a theoretical energy potential and associated PDF of position can be seen in Fig. 3.1.4 for $\ell_B = 500$ nm, $B = 4$ and $\ell_D = 50$ nm.

```

1 import numpy as np
2
3 def _Peq(z):
4     if z <= 0:
5         return 0
6     else:
7         return np.exp(-(B * np.exp(-z / ld) + z / lb))
8
9
10 def Peq(z):
11     P = np.array([_Peq(zi) for zi in z])
12     return P / np.trapz(P, z)

```

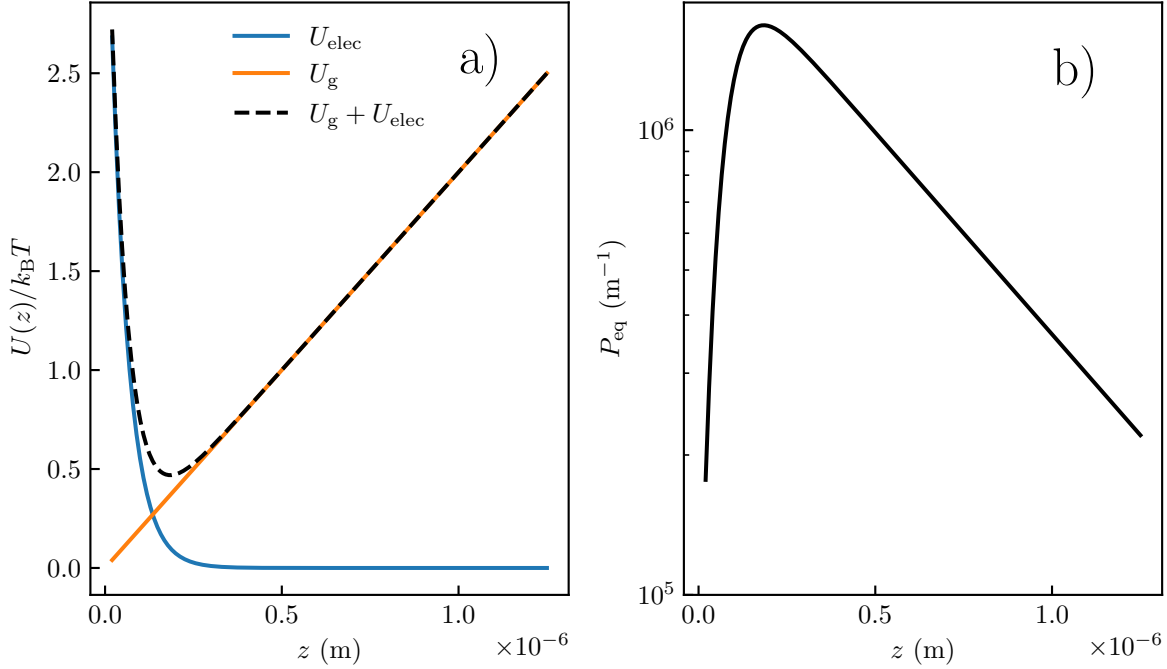


Figure 3.1.4: a) In orange potential energy U_g (see Eq. (3.1.3)) of a colloid with a Boltzmann length $\ell_B = 500$ nm. In blue, the electrostatic potential energy U_{elec} (see Eq. (3.1.22)) is characterized by a dimensionless magnitude $B = 4$ and a Debye length $\ell_D = 50$ nm. The dashed line corresponds to the total potential U , see Eq. (3.1.27). b) Corresponding Gibbs-Boltzmann equilibrium distribution of position calculated using the energy potential of panel a).

3.1.3 Local diffusion coefficient

As we have seen in Chapter 1, for a freely diffusing colloid in the bulk, the diffusion coefficient is given by Eq. (1.2.12) and is a constant. However, when a particle is confined by a rigid wall, the diffusion is hindered. This means that the diffusion coefficient varies with the particle-wall distance and becomes anisotropic. A seminal measurement of this effect was done by Faucheux and Libchaber [52]. As we can see in Fig. 3.1.5, using a microscope, they tracked colloids within a parallelepipedic chamber, and measured the thickness-averaged diffusion coefficients for different values of the confinement parameter $\gamma = \langle z \rangle_t / a$, with $\langle z \rangle_t$ time-averaged particle-wall distance. As experiments reach equilibrium, $\langle z \rangle_t$ is given by the Gibbs-Boltzmann distribution as $\langle z \rangle_t = \int dz P_{\text{eq}}(z)z$. We observe that the diffusion coefficient parallel to the surface decreases as the particle gets closer to the wall, and seems to saturate around $0.3D_0$ at low γ , with D_0 the diffusion coefficient in the bulk (see Eq. 3.1.33).

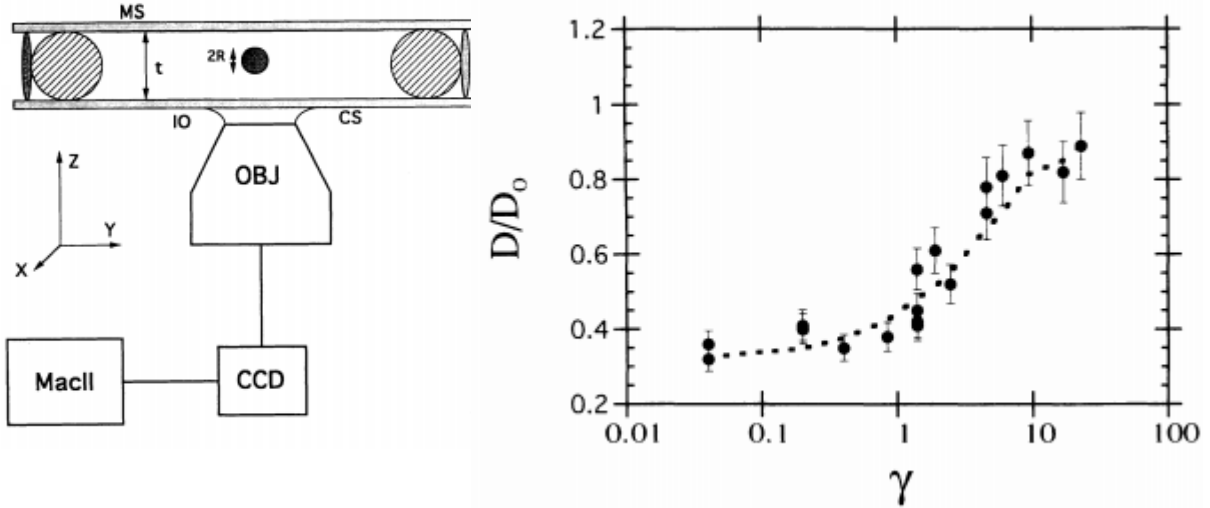


Figure 3.1.5: Figure extracted from [52]. On the left is the experimental setup. It is an inverted microscope used in order to track micrometric particles of diameter $2R$ inside a liquid cell of thickness t . On the right is the final result, where the authors measure the diffusion parallel (*i.e.* along x or y) coefficient D_{\parallel} (see Eqs. (3.1.47) and (3.1.45)), normalized by the bulk diffusion coefficient D_0 , as a function the confinement parameter $\gamma = \langle z \rangle_t / a$, with $\langle z \rangle_t$ time-averaged particle-wall distance.

To understand the reason for this hindered diffusion coefficient, let us start by writing the diffusion coefficient D using the fluctuation dissipation theorem:

$$D = \frac{1}{\gamma} k_B T , \quad (3.1.30)$$

with the mobility defined as:

$$\frac{1}{\gamma} = \left| \frac{v_{\text{sphere}}}{F_{\text{drag}}} \right| , \quad (3.1.31)$$

where v_{sphere} is the terminal velocity to an applied force F_{drag} . For a spherical colloid of radius a moving at a velocity v_{sphere} , the drag force F_{drag}^B is given by the Stokes' law:

$$F_{\text{drag}}^B = -c\pi\eta av_{\text{sphere}} , \quad (3.1.32)$$

where c is a constant that depends on the boundary conditions imposed at the surface

of the colloid. Typically, one has $c = 6$ for a no-slip boundary conditions and $c = 4$ for a full-slip boundary conditions, such as for air bubbles for example. Combining Eqs. (3.1.30), (3.1.31) and (3.1.32) for a freely diffusing no-slip hard sphere in the bulk we retrieve Eq. (1.2.12):

$$D = D_0 = \frac{k_B T}{6\pi\eta a} . \quad (3.1.33)$$

The Stokes' drag force can be computed by solving the Navier-Stokes equation:

$$\rho \left[\frac{\partial \vec{v}}{\partial t} + (\vec{v} \cdot \nabla) \vec{v} \right] + \nabla p = \eta \nabla^2 \vec{v} , \quad (3.1.34)$$

and the continuity equation for incompressible fluids:

$$\nabla \cdot \vec{v} = 0 , \quad (3.1.35)$$

where \vec{v} and p are receptively the velocity and pressure fields, and where ρ is the liquid density. When the Reynolds number $\text{Re} = \rho a v_{\text{sphere}} / \eta \ll 1$, the second inertial term is negligibly small compared to the viscous term $\eta \nabla^2 \vec{v}$. In that case, and at long-enough time for the first inertial term to be negligible, the Eq. (3.1.34) is simplified to the steady Stokes equation:

$$\nabla p = \eta \nabla^2 \vec{v} . \quad (3.1.36)$$

By solving Eqs. (3.1.35) and (3.1.36) with a no-slip boundary condition on the particle surface and the field vanishing at infinity, one can calculate the velocity and the pressure fields in the fluid. By integration of the pressure and viscous stress on the particle surface, one eventually gets the Stokes mobility. However, in the case of a confined particle near a wall there is an additional no-slip condition at the wall surface. At the macro scale, this effect can be seen with a frisbee, indeed, as it gets closer to the ground, hydrodynamic pressure increases due to the increasing air velocity gradient in the gap and one can observe a slowing down of the free fall.

To get some physical insight on this effect, one can use the lubrication theory to make a scaling of the drag force experience by a particle confined near a wall. As schematized in

Fig. 3.1.6, we consider a particle of radius a moving at a velocity V .

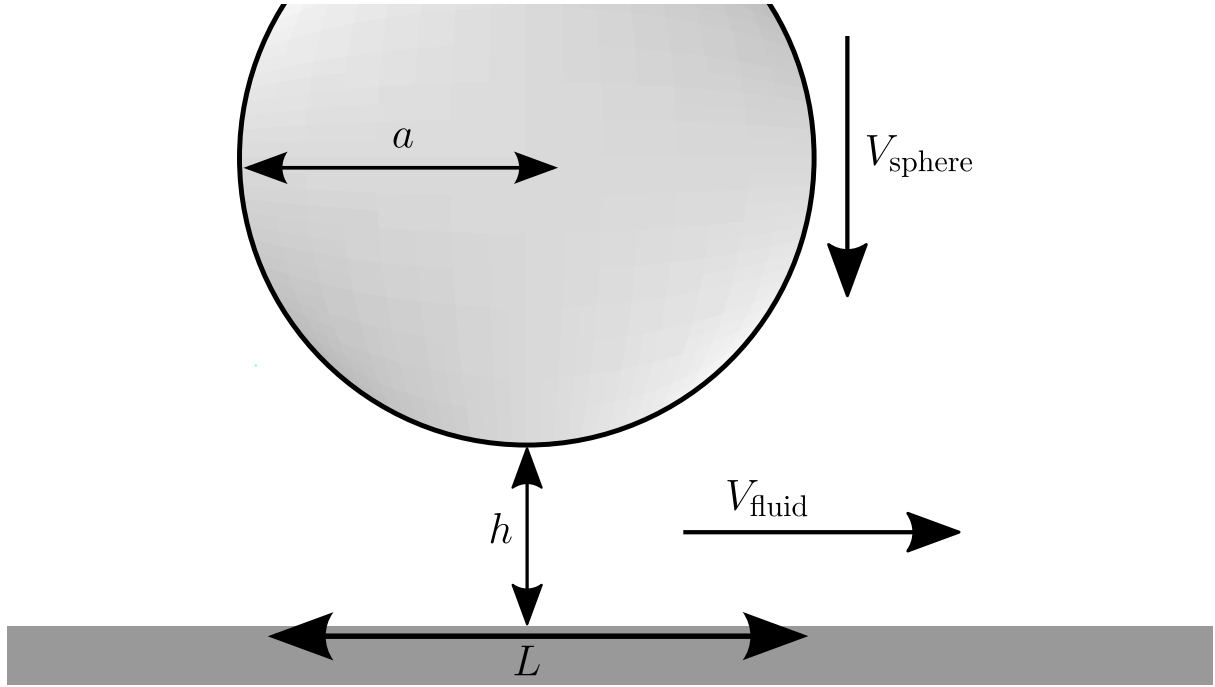


Figure 3.1.6: Schematic representation of a spherical object of radius a moving towards a wall at velocity V_{sphere} and inducing a fluid velocity V_{fluid}

As we are using the lubrication theory, we suppose that the particle is close to the wall such that $h \ll a$. In that condition, we suppose that a particle moving towards a wall (*along the z-axis*) at a velocity V_{sphere} induces a fluid velocity V_{fluid} along the x -axis, we further suppose that the induced velocity along the z -axis is negligible. Moreover, the typical length scale along the z -axis is the particle-wall distance z ; and the distance $L = \sqrt{az}$ (*i.e.* Hertz contact), along the x -axis. In this approximation, velocity terms along the z -axis will be negligible in Eq. (3.1.36), a projection along the z -axis thus gives:

$$\frac{\partial p}{\partial z} = 0 . \quad (3.1.37)$$

On the right-hand side of Eq. 3.1.36, the viscous term simplifies to $\eta \partial_z^2 V_{\text{fluid}}$ as:

$$\frac{\partial^2 V_{\text{fluid}}}{\partial x^2} \approx \frac{V_{\text{fluid}}}{L^2} \ll \frac{V_{\text{fluid}}}{h^2} \approx \frac{\partial^2 V_{\text{fluid}}}{\partial z^2} . \quad (3.1.38)$$

In the lubrication theory, Eq. (3.1.36) is finally simplified to:

$$\frac{\partial p}{\partial x} = \eta \frac{\partial^2 V_{\text{fluid}}}{\partial z^2} . \quad (3.1.39)$$

By replacing the partial derivative by the typical length leads to:

$$p \sim \eta V_{\text{fluid}} \frac{L}{z^2} \quad (3.1.40)$$

To compute the calculate the Stokes mobility, one needs to evaluate the viscous stress σ , in the lubrication theory, it reads:

$$\sigma = \eta \frac{\partial V_{\text{fluid}}}{\partial z} \sim \eta \frac{V_{\text{fluid}}}{h} \quad (3.1.41)$$

When the particle is moving towards the wall we thus have $p \gg \sigma$, we thus only consider the pressure. To evaluate the mobility, we need to write Eq. (3.1.40) as a function of V_{sphere} . Using Eq. (3.1.35) equation one has $V_{\text{fluid}}/h \sim V_{\text{sphere}}/L$, Eq. (3.1.40) thus become:

$$p \sim \eta \frac{L^4}{h^2} \quad (3.1.42)$$

Integrating this pressure over the particle surface (*i.e* over the typical length $L = \sqrt{az}$) leads a scaling of the drag force:

$$F_{\text{drag}}^{z \ll a} \sim \eta V \frac{L^4}{h^2} = \eta V \frac{a^2}{z} \quad (3.1.43)$$

The mobility (see Eq. (3.1.31)) of the displacement perpendicular to the wall thus scale as $\gamma_0^{-1} h/a$, with γ_0^{-1} the bulk mobility. Therefore, the diffusion coefficient of a confined colloid near a wall in the lubrication approximation is hindered and inversely proportional to the particle-wall distance. It is possible to same scaling for the parrallel mobility by supposing that the particle is moving along the x -axis. In that case, one can find that the viscous stress is greater than the pressure and finally find that along the x -axis, the parallel mobility follow the same scaling as in bulk and remain constant.

To recap, a colloid diffusing near a wall thus experience a local drag force that depends on both its distance z to the wall and direction of motion. Thanks to the linearity of the Stokes equation, one can decompose this local drag force in two contributions, for motions parallel and perpendicular to the wall. As the presence of the wall modifies the drag force with a space-dependent multiplicative factor, the confinement effect is often expressed in terms of effective viscosities:

$$\eta_{\perp}(z) = \eta\lambda_{\perp}(z) , \text{ and } \eta_{\parallel}(z) = \eta\lambda_{\parallel}(z) , \quad (3.1.44)$$

where λ_{\perp} and λ_{\parallel} are respectively the perpendicular and parallel correction factors. Taking into account these corrections, the diffusion coefficients for perpendicular and parallel motions relative to the wall read:

$$D_{\perp}(z) = \frac{D_0}{\lambda_{\perp}(z)} , \text{ and } D_{\parallel}(z) = \frac{D_0}{\lambda_{\parallel}(z)} . \quad (3.1.45)$$

For no-slip boundary conditions imposed at both the wall and the surface of the colloid, Brenner [53] obtained for the perpendicular motion:

$$\lambda_{\perp}(z) = \frac{4}{3}\sinh\beta \sum_{n=1}^{\infty} \frac{n(n+1)}{(2n-1)(2n+3)} \left[\frac{2\sinh(2n+1)\beta + (2n+1)\sinh 2\beta}{4\sinh^2(n+1/2)\beta - (2n+1)^2\sinh^2\beta} - 1 \right] , \quad (3.1.46)$$

where $\beta = \cosh^{-1}((z+a)/a)$. For the motion of a sphere parallel to a wall, Faxén found [54]:

$$\lambda_{\parallel}(z) = \left[1 - \frac{9}{16}\xi + \frac{1}{8}\xi^3 - \frac{45}{256}\xi^4 - \frac{1}{16}\xi^5 \right]^{-1} , \quad (3.1.47)$$

where $\xi = a/(z+a)$. Eqs. (3.1.46) and (3.1.47) are exact for all z and shown in Fig. 3.1.7-a). However, the solution for the perpendicular motion can be complex to compute as it is an infinite series. It requires a software that enables arbitrary-precision floating-point arithmetic⁷ — such as Mathematica or the `mpmath` Python’s module, for example. D_{\perp} can be evaluated using the following Python snippet, where the `nsum` function is used to compute the summation:

```

1 from mpmath import nsum
2
3 def Dz(eta, z, a):
4     a = (z + a) / a
5     beta = float(acosh(a))

```

⁷ Arbitrary-precision floating-point arithmetic enables to evaluate mathematical expressions with any precision, *i.e.* any number of digits.

```

6     summ = nsum(
7         lambda n: (n * (n + 1) / ((2 * n - 1) * (2 * n + 3)))
8         *
9         (
10            (2 * sinh((2 * n + 1) * xi) + (2 * n + 1) * sinh(2 * beta))
11            /
12            4 * (sinh((n + 1 / 2) * beta) ** 2)
13            - ((2 * n + 1) ** 2) * (sinh(beta) ** 2)
14        )
15    )
16    - 1
17 ),
18 [0, inf],
19 )
20 summ = float(summ)
21 return kT / (6 * pi * eta * 4 / 3 * float(sinh(beta)) * summ * a)

```

To simplify the computation of λ_{\perp} , Honig [55], and Bevan and Prieve [56] showed that Eq. (3.1.46) can be Padé approximated⁸, giving:

$$\lambda_{\perp} = \frac{6z^2 + 9az + 2a^2}{6z^2 + 2az} . \quad (3.1.48)$$

In the near-wall regime, such that $z \ll a$, it is possible to further approximate λ_{\perp} by its asymptotic expression:

$$\lambda_{\perp} \simeq \frac{a}{z} . \quad (3.1.49)$$

⁸ A Padé approximant is the approximation of a power series by a rational fraction [57].

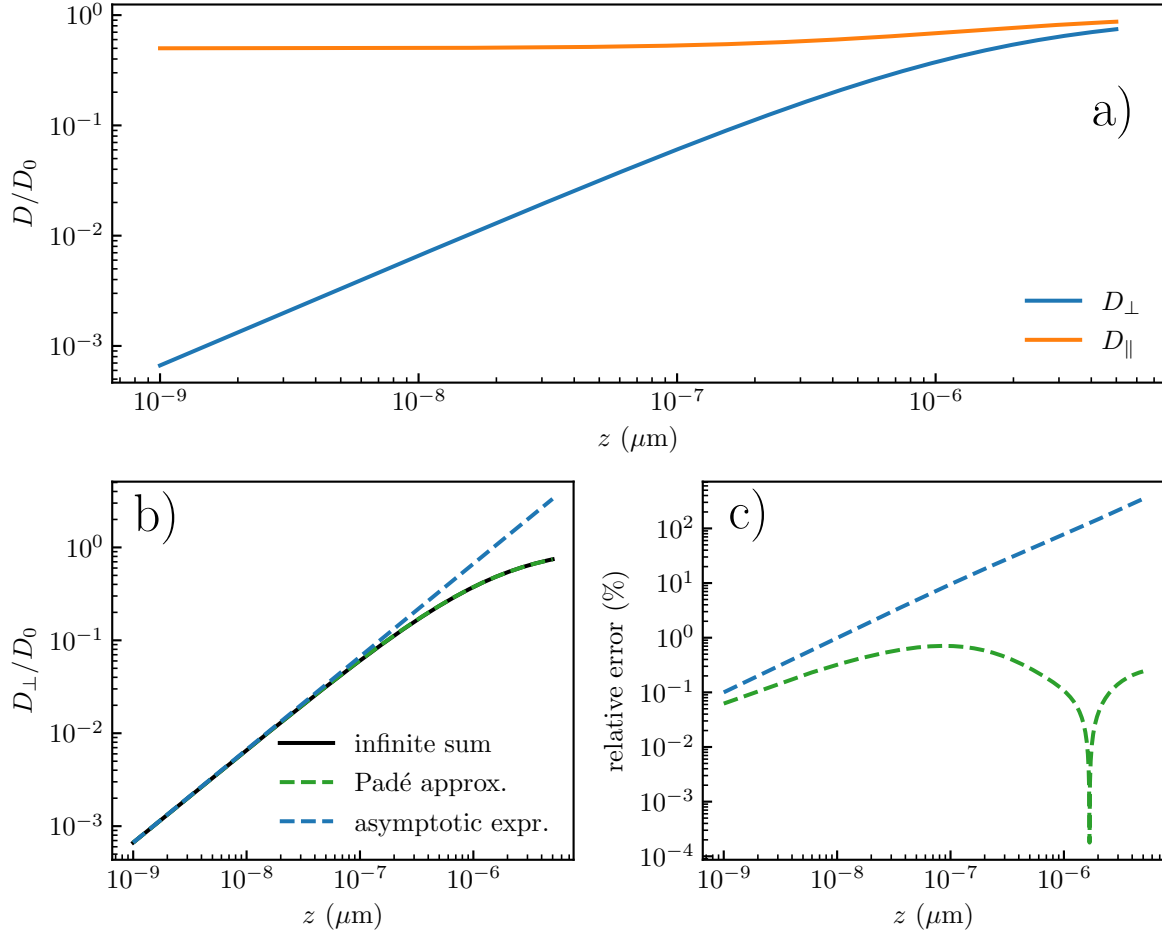


Figure 3.1.7: a) Parallel and perpendicular normalized diffusion coefficients for a colloidal particle of radius $a = 1.5 \mu\text{m}$. b) Perpendicular normalized diffusion coefficient at a distance z from a wall. The solid black line is the exact solution given by the infinite sum of Eq. (3.1.46). The green dashed line is the Padé approximation of Eq. (3.1.48). The blue dashed line is the near-wall asymptotic expression of Eq. (3.1.49). c) Relative errors between the two approximations (dashed lines of panel b), same color code) and the exact result (solid line of panel b)).

The exact result, together with the Padé approximation and the near-wall asymptotic expression for the hindered vertical diffusion are plotted in Fig. 3.1.7-b). The Padé approximation fits well the exact solution, the near-wall asymptotic expression fits well when $z < a/10$ typically. To check how precise both approximations are, we plot the relative error in Fig. 3.1.7-c). The Padé approximation shows precision up to 1%. Thus, in the following, when evaluating perpendicular diffusion coefficients, or equivalently vertical effective viscosities, the Padé approximation will be used.

3.1.4 Langevin equation for confined Brownian motion

Now that the external forces acting on the particle and hindered diffusion coefficients are known, we rewrite the overdamped Langevin (see Eq. (1.3.10)) as:

$$V_t^i dt = -\mu(z) \frac{\partial U(z)}{\partial x_i} dt + \sqrt{2D_i(z)} dB_t , \quad (3.1.50)$$

where $\mu(z) = 1/(6\pi\eta_i(z)a)$, and i denotes one of the three spatial directions, x , y and z , where the previously determined η_{\parallel} or D_{\parallel} corresponds to the x - and y -axes, while η_{\perp} or D_{\perp} corresponds to the z -axis, and dB_t is a Gaussian-distributed satisfying $\langle dB_t \rangle = 0$ and $\langle dB_t^2 \rangle = dt$. As discussed previously, the potential energy U only varies along the z -axis, and thus, the external force only acts on the particle along the z -axis while the particle diffuses freely along the x - and y -axes.

3.1.5 Spurious drift

A key observation is that due to the spatially-varying and direction-varying mobilities of the particle, the magnitude $\sqrt{2D_i(z)}$ of the Langevin forces, depend on the random position and direction of the particle. This is an example of a so-called multiplicative noise and will have some interesting consequences on the dynamical properties of the random motion. To illustrate the effect of the multiplicative noise, one can integrate Eq. (3.1.50) over a time τ in the absence of the external force, which leads to:

$$\Delta x_i = \int_{t_0}^{t_0+\tau} \sqrt{2D_i(z)} dB_t , \quad (3.1.51)$$

where Δx_i is the spatial increment in the i direction. However, the noise term the time (and consequently the position) at which the magnitude $\sqrt{2D_i(z)}$ of the Langevin force is evaluated in the integral of Eq. (3.1.51) needs to be specified. We write $D(z)$ as $D(z + \alpha\Delta x_z)$, with $\alpha \in [0, 1]$. The value of α determines at which time in the interval $[t_0, t_0 + \tau]$ the local diffusion is evaluated. However, α should be taken to have the long-time thermal equilibrium to be consistent with the Boltzmann distribution and. Taking into account α , the Eq. 3.1.51 in the z direction becomes:

$$\Delta z = \sqrt{2D_{\perp}(z + \alpha\Delta z)} dB_t , \quad (3.1.52)$$

where we write $\Delta x_z = \Delta z$ for simplicity. By Taylor-expanding D_\perp at the first order in $\Delta z/z$, one has:

$$D_\perp(z + \alpha\Delta z) \simeq D_\perp(z) + \alpha \frac{dD_\perp(z)}{dz} \Delta z . \quad (3.1.53)$$

Substituting the latter in Eq. (3.1.52) leads to:

$$\begin{aligned} \Delta z &\simeq \sqrt{2D_\perp(z) + 2\alpha \frac{dD_\perp(z)}{dz} \Delta z dB_t} \\ &= \sqrt{2D_\perp(z)} \left[1 + \alpha \frac{dD_\perp(z)}{dz} \frac{\Delta z}{D_\perp(z)} \right]^{1/2} dB_t . \end{aligned} \quad (3.1.54)$$

Additionally, since the last term satisfies:

$$\left| \alpha \frac{dD_\perp(z)}{dz} \frac{\Delta z}{D_\perp(z)} \right| \ll 1 , \quad (3.1.55)$$

one Taylor-expands at first order the right-hand side of Eq. (3.1.54) as:

$$\left[1 + \alpha \frac{dD_\perp(z)}{dz} \frac{\Delta z}{D_\perp(z)} \right]^{1/2} \simeq 1 + \frac{\alpha}{2} \frac{dD_\perp(z)}{dz} \frac{\Delta z}{D_\perp(z)} . \quad (3.1.56)$$

By inserting Eq. (3.1.56) into Eq. (3.1.54), and by using the lowest order of Δz to evaluate the first-order term, we obtain:

$$\begin{aligned} \Delta z &\simeq \sqrt{2D_\perp(z)} \left[1 + \frac{\alpha}{2} \frac{dD_\perp(z)}{dz} \frac{\sqrt{2D_\perp(z)} dB_t}{D_\perp(z)} \right] dB_t \\ &= \sqrt{2D_\perp(z)} dB_t + \alpha \frac{dD_\perp(z)}{dz} [dB_t]^2 \end{aligned} \quad (3.1.57)$$

Taking the average value of Eq. (3.1.57) by discretizing over a time $\tau \ll 1$ such that $\langle [dB_t]^2 \rangle_t = \tau$, gives:

$$\langle \Delta z \rangle_t = \alpha \frac{dD_\perp(z)}{dz} \tau = v_{\text{noise}} \tau , \quad (3.1.58)$$

where v_{noise} represents a noise-induced spurious drift velocity. By putting back the interactions with the wall, the full expression of Eq. 3.1.57 reads[58]:

$$\begin{aligned}\Delta z &= \alpha \frac{dD_{\perp}(z)}{dz} \tau - \frac{1}{\gamma(z)} \frac{dU(z)}{dz} \tau + \sqrt{2D_{\perp}(z)} dB_t \\ &= \left(-\frac{1}{\gamma(z)} \frac{dU(z)}{dz} + \alpha \frac{dD_{\perp}(z)}{dz} \right) \tau + \sqrt{2D_{\perp}(z)} dB_t \\ &= \bar{v}_d \tau + \sqrt{2D_{\perp}(z)} dB_t ,\end{aligned}\quad (3.1.59)$$

where:

$$\bar{v}_d = -\frac{1}{\gamma(z)} \frac{\partial U(z)}{\partial z} + \alpha \frac{dD_{\perp}(z)}{dz} = v_d + v_{\text{noise}} ,\quad (3.1.60)$$

is the total drift velocity of the particle. The first term v_d is the drift velocity due to deterministic forces (electrostatic and gravitational interactions in our case). The spurious drift velocity v_{noise} disappears when the diffusion coefficient is homogeneous, and would also disappear along the x - and y -axes since the diffusion coefficients only depend on the colloid-wall distance z (a derivative with respect to x would replace the one in z in the equivalent of Eq. (3.1.60) for the x direction). Theoretically, α can take any value between 0 and 1. However, three canonical values are usually employed [59]: $\alpha = 0$, in the Itô convention, corresponding to the use of the initial value of $D(z)$; $\alpha = 1/2$, in the Stratonovich convention, corresponding to the mid-point value; and $\alpha = 1$ in the anti-Itô or isothermal convention, corresponding to the use of the final value. Using Eqs. (3.1.45) (3.1.48) and (3.1.60), the deterministic drift velocity reads:

$$v_d = -\frac{k_B T}{\gamma(z)} \left[-\frac{1}{\ell_D} B \exp \left(-\frac{z}{\ell_D} \right) + \frac{1}{\ell_B} \right] ,\quad (3.1.61)$$

and the spurious drift velocity reads:

$$v_{\text{noise}}(z) = 2\alpha D_0 a \frac{2a^2 + 12az + 21z^2}{(2a^2 + 9az + z^2)^2} ,\quad (3.1.62)$$

Finally, one can decompose the Langevin equation for a particle near a wall in two, one equation describing the motion perpendicular (*i.e.* along the z -axis):

$$V_t^z dt = \bar{v}_d dt + \sqrt{2D_{\perp}(z)} dB_t , \quad (3.1.63)$$

and one for the parallel motion (*i.e.* along the x - and y):

$$V_t^{\parallel} dt = \sqrt{2D_{\parallel}(z)} dB_t , \quad (3.1.64)$$

A typical example of drift velocity \bar{v} for a colloidal particle of radius $a = 1.5 \mu\text{m}$ in water, moving near a wall, and interacting with the latter through an electrostatic potential with a Debye length $\ell_D = 50 \text{ nm}$ and a dimensionless magnitude of the interaction $B = 4$, and evolving in a gravity field characterized by a Boltzmann length $\ell_B = 500 \text{ nm}$, is plotted in Fig. 3.1.8. As one can observe, the spurious drift is not negligible.

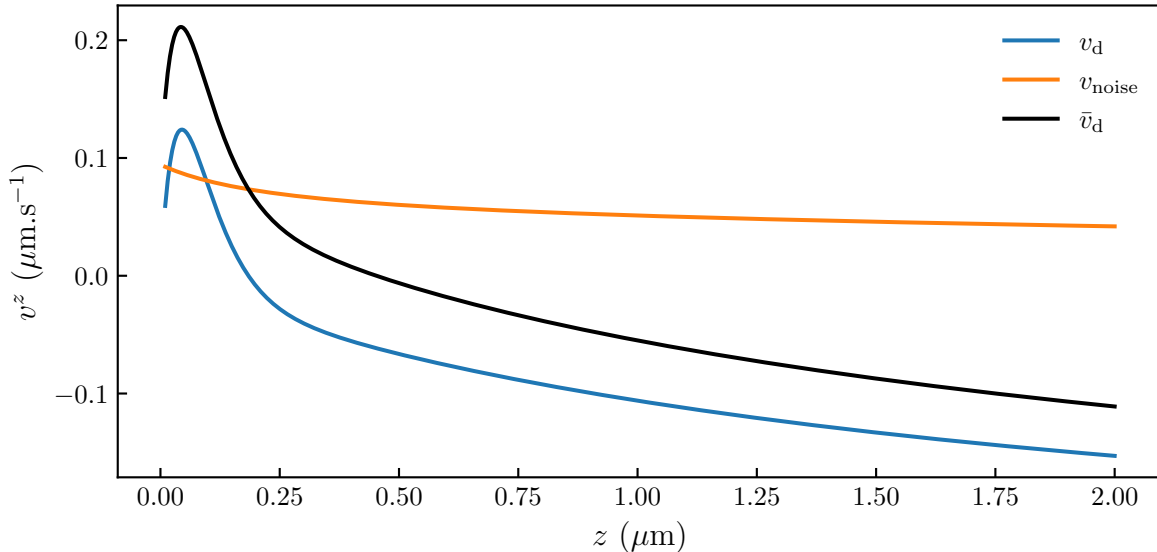


Figure 3.1.8: Theoretical drift velocity for a colloidal particle of radius $a = 1.5 \mu\text{m}$ in water and at a distance z from the wall. The physical parameters $\ell_D = 50 \text{ nm}$, $B = 4 k_B T$ and $\ell_B = 500 \text{ nm}$.

3.1.6 Fokker-Plank equation

The Fokker-Plank equation is an alternative way to describe Brownian motion. Instead of explicitly calculating a Brownian trajectory by solving the Langevin equation, Fokker-Plank equation describes the Probability Density Function $P(X_t, X_0; t)$ imposition, where for simplicity we place ourselves in 1D, with X_t denoting the particle position at a time t and X_0 its initial ($t = 0$) position. To derive the Fokker-Plank equation, let us start by taking a generic Langevin equation in 1D:

$$dX_t = u(X_t)dt + \zeta(X_t)dB_t , \quad (3.1.65)$$

where u is the drift due to external forces and ζ is the magnitude of the random force. Let consider the average value of an arbitrary function $f(X_t)$ for a stochastic process obeying Eq. (3.1.65), which started at position x_0 at time $t = 0$. By definition, this ensemble average reads [60]:

$$\langle f(X_t) \rangle = \int dX_t P(X_t, X_0; t) f(X_t) , \quad (3.1.66)$$

with the initial condition that can be written as:

$$P(X_t, X_0; 0) = \delta(X_t - X_0) . \quad (3.1.67)$$

We now expand f at the first order in the time increment dt as:

$$\begin{aligned} \left\langle \frac{df(X_t)}{dt} \right\rangle_t &\simeq \frac{1}{dt} \left\langle \frac{\partial f(X_t)}{\partial X_t} u(X_t) dt + \frac{\partial f(X_t)}{\partial X_t} \zeta(X_t) dB_t + \frac{1}{2} \frac{\partial^2 f(X_t)}{\partial X_t^2} \zeta^2(X_t) dB_t^2 \right\rangle_t \\ &= \frac{1}{dt} \left(\frac{\partial f(X_t)}{\partial X_t} u(X_t) dt + \frac{1}{2} \frac{\partial^2 f(X_t)}{\partial X_t^2} \zeta^2(X_t) dt \right) \\ &= \frac{\partial f(X_t)}{\partial X_t} u(X_t) + \frac{1}{2} \frac{\partial^2 f(X_t)}{\partial X_t^2} \zeta^2(X_t) . \end{aligned} \quad (3.1.68)$$

By combining Eqs. (3.1.66) and (3.1.68), we get:

$$\begin{aligned} \int dX_t \frac{\partial P(X_t, X_0; t)}{\partial t} f(X_t) &= \frac{\partial f(X_t)}{\partial X_t} u(X_t) + \frac{1}{2} \frac{\partial^2 f(X_t)}{\partial X_t^2} \zeta^2(X_t) \\ &= \int dX_t P(X_t, X_0; t) Gf(X_t) , \end{aligned} \quad (3.1.69)$$

where G is a differential operator called the generator and is defined by its action on a function f as:

$$Gf = \frac{1}{2} \zeta^2(X_t) \frac{\partial^2 f(X_t)}{\partial X_t^2} + u(X_t) \frac{\partial f(X_t)}{\partial X_t} . \quad (3.1.70)$$

Using the definition of the adjoint of G , denoted G^\dagger , one has:

$$\begin{aligned} \int dX_t \frac{\partial P(X_t, X_0; t)}{\partial t} f(X_t) &= \int dX_t P(X_t, X_0; t) Gf(X_t) \\ &= \int dX_t G^\dagger P(X_t, X_0; t) f(X_t) . \end{aligned} \quad (3.1.71)$$

From the latter, we thus have:

$$\frac{\partial P(X_t, X_0; t)}{\partial t} = G^\dagger P(X_t, X_0; t) , \quad (3.1.72)$$

which leads to the Forward Fokker-Planck equation [61]:

$$\frac{\partial P(X_t, X_0; t)}{\partial t} = \frac{\partial^2}{\partial X_t^2} \left[\frac{\zeta^2(X_t)}{2} P(X_t, X_0; t) \right] - \frac{\partial}{\partial X_t} [u(X_t) P(X_t, X_0; t)] . \quad (3.1.73)$$

The latter is called Forward because the partial differential equation is written in terms of the variable X_t , *i.e.* the position of the particle, at time t . For a Brownian motion near a wall, using the previously determined drifts velocity \bar{v}_d along z of Eq. (3.1.60), the Fokker-Plank equation for the motion along the z -axis, perpendicular to the wall reads:

$$\frac{\partial P(z, z_0; t)}{\partial t} = \frac{\partial^2}{\partial z^2} [D_\perp(z) P(z, z_0; t)] - \frac{\partial}{\partial z} [\bar{v}_d P(z, z_0; t)] , \quad (3.1.74)$$

with z the particle position along the z -axis. In particular, the stationary solution of Eq. (3.1.74), *i.e.* for $\partial p / \partial t = 0$, is given by the Gibbs-Boltzmann distribution $P_{\text{eq}}(z)$ (see Eq. (3.1.29)). The solution of Eq. (3.1.72) with the particle starting at position z_0 , at time $t = 0$ reads:

$$\begin{aligned} P(z, z_0; t) &= \exp\{G^\dagger t\} P(z, z_0; 0) \\ &= \exp \left\{ \frac{\partial^2}{\partial z^2} D_\perp(z) t - \frac{\partial}{\partial z} \bar{v}_d t \right\} \delta(z - z_0) . \end{aligned} \quad (3.1.75)$$

3.1.7 Numerical simulations of confined Brownian motion

We previously determined that the simulation of a bulk Brownian motion without external forces can be simulated using Eq. (1.4.9). However, in the case of confined Brownian motion, and without density matching, one needs to take into account the hindered mobility, external forces due to gravity and the double-layer interaction, as well as the confinement-induced spurious drift. Putting all that together leads to a new equation for x_i which reads for the motion parallel to wall (*i.e.* along the x - and y -axes):

$$x_i = x_{i-1} + \sqrt{2D_{\parallel}}w_i , \quad (3.1.76)$$

where we recall that we approximate the continuous position X_t of a particle at a time t by a discrete-time sequence x_i , which is the solution of the equation at a time $t_i = i\tau$. τ being the numerical integration time increment, and w_i is a Faussian-distributed number of mean value $\langle w_i \rangle = 0$ and variance $\langle w_i^2 \rangle = \tau$. For the particle perpendicular motion (along the z -axis), one needs to add the total drift \bar{v}_d of Eq. (3.1.60), such that:

$$z_i = z_{i-1} + \bar{v}_d(z_{i-1})\tau + \sqrt{2D_{\perp}}w_i , \quad (3.1.77)$$

where z_i is the discrete-time position sequence of a particle along the z -axis. Compared to bulk Brownian motion where the time step τ can be chosen only according to the desired precision as shown previously on Fig. 1.4.2, confinement adds another constraint. Indeed, the time step should be short enough for the drift \bar{v}_d and local diffusion coefficients to be relatively constant (as detailed later) in the time period $t_{i+1} - t_i = \tau$ and in the displacement range $\Delta z = z_{i+1} - z_i$, such that:

$$\bar{v}_d(z \in [z_i, z_{i+1}]) \simeq \bar{v}_d(z_i) , \quad (3.1.78)$$

and:

$$D_{\perp,\parallel}(z \in [z_i, z_{i+1}]) \simeq D_{\perp,\parallel}(z_i) . \quad (3.1.79)$$

Since the diffusion coefficient does not vary for the parallel motion, one can consider only the perpendicular motion to determine the optimal simulation time step. Also, as it can

be seen in Fig. 3.1.9 the relative variation of the drift velocity $1/\bar{v}_d \partial_z \bar{v}_d$ reaches higher values than the relative variation of the diffusion coefficient $1/D_\perp \partial_z D_\perp$. Thus, finding τ that satisfies Eq. (3.1.78) is sufficient. Moreover, the vertical drift velocity varies more when the colloid is near the surface, *i.e.* in the region where one can approximate the diffusion coefficient D_\perp using Eqs. (3.1.45) and (3.1.49):

$$D_\perp(z)|_{z \ll a} = D_0 \frac{z}{a}. \quad (3.1.80)$$

In that case, by choosing the isothermal convention ($\alpha = 1$), Eq. (3.1.60) near the surface simplifies to:

$$\begin{aligned} \bar{v}_d &\simeq \frac{k_B T}{\gamma_0} \frac{z}{a} \left[\frac{B}{\ell_D} \exp\left(-\frac{z}{\ell_D}\right) - \frac{1}{\ell_B} \right] + \frac{\partial}{\partial z} D_0 \frac{z}{a} \\ &= \frac{D_0}{a} \left[1 + \frac{Bz}{\ell_D} \exp\left(-\frac{z}{\ell_D}\right) - \frac{1}{\ell_B} \right] \end{aligned} \quad (3.1.81)$$

By expanding the exponential term at the first order in z/ℓ_D , we get:

$$\bar{v}_d = \frac{D_0}{a} \left(1 + \frac{Bz}{\ell_D} - \frac{1}{\ell_B} \right) \quad (3.1.82)$$

To satisfy Eq. (3.1.78), we need to have a small relative change of the vertical drift velocity in an interval $[z, z + \Delta z]$ [62], *i.e.*:

$$\frac{|\bar{v}_d(z + \Delta z) - \bar{v}_d(z)|}{|\bar{v}_d(z)|} \ll 1. \quad (3.1.83)$$

Combining Eqs. (3.1.82) and (3.1.83), we get:

$$|\Delta z| \ll \left[\frac{B}{\ell_D} \right]^{-1} + z. \quad (3.1.84)$$

Besides, invoking the vertical MSD over the time step, as well as Eq. (3.1.80), one gets:

$$\langle \Delta z^2 \rangle(z) = 2D_\perp(z)\tau = 2D_0 \frac{z}{a} \tau. \quad (3.1.85)$$

Combining Eqs. (3.1.84) and (3.1.85) thus leads to:

$$\tau = \frac{a\langle\Delta z^2\rangle}{2D_0z} \ll \frac{a}{2D_0} \frac{\left[\left(\frac{B}{\ell_D} - \frac{1}{\ell_B}\right)^{-1} + z\right]^2}{z} = \tau_{\max}(z) . \quad (3.1.86)$$

At this point, there are two different options for the time step in the simulation: the first one is to do an adaptive time step using a local $\tau(z)$ that satisfies $\tau(z) \ll \tau_{\max}(z)$ for each step of the simulation; the second one is to find the smallest $\tau_{\max}(z)$ and use for all the simulation a time step τ satisfying $\tau \ll \min(\tau_{\max})$. The latter can be evaluated by finding the height z_{\min} , at which the derivative of τ_{\max} nullifies, *i.e.*:

$$\frac{\partial\tau_{\max}}{\partial z}\Bigg|_{z_{\min}} = 0 . \quad (3.1.87)$$

Solving the latter gives,

$$z_{\min} = \left| \left(\frac{B}{\ell_D} - \frac{1}{\ell_B} \right)^{-1} \right| . \quad (3.1.88)$$

which finally gives:

$$\min(\tau_{\max}) = \frac{2a}{D_0} \left| \left(\frac{B}{\ell_D} - \frac{1}{\ell_B} \right)^{-1} \right| . \quad (3.1.89)$$

In Fig. 3.1.9-b) τ_{\max} is plotted as a function of z , for $a = 1.5 \mu\text{m}$, $B = 4$ and ℓ_D varying between 20 and 100 nm. We observe that for this range of values that represents well the experiments that I have performed during my thesis, taking a constant simulation time step $\tau \approx 0.01 \text{ s}$ is satisfactory.

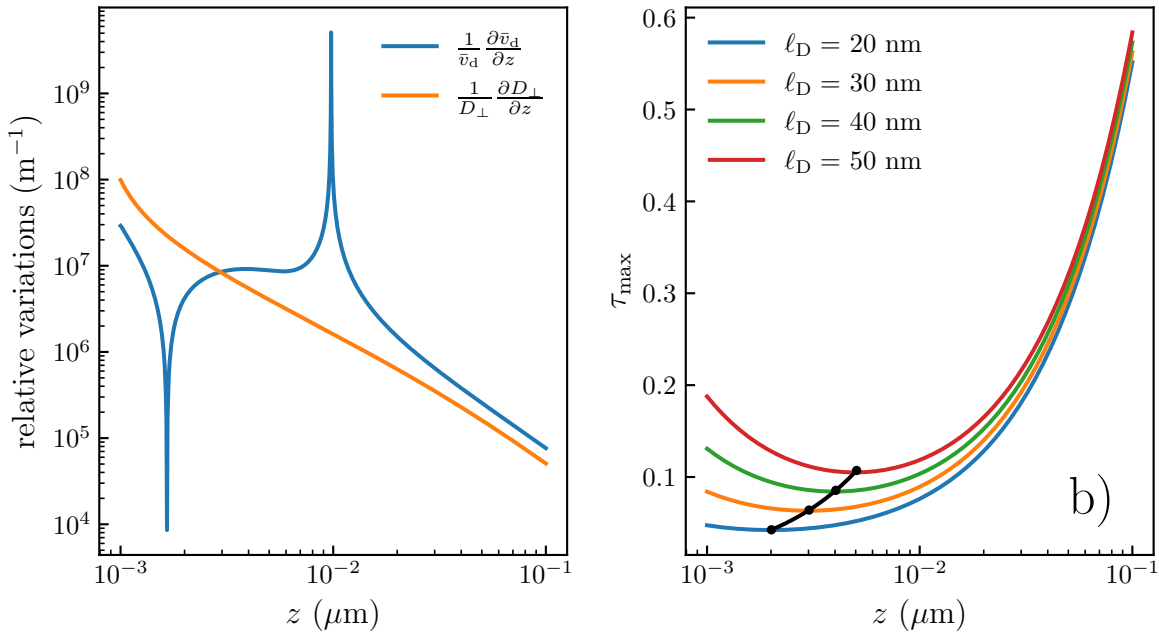


Figure 3.1.9: a) Theoretical computation of the relative variation of the drift velocity \bar{v}_d and perpendicular diffusion coefficient D_\perp as a function particle-wall distance z . The parameters are $\ell_D = 50$, $B = 4$ and $\ell_B = 500$ nm b) Optimal numerical integration time step τ_{\max} as a function of the particle-wall distance z for a particle of radius $a = 1.5$ μm, with $\ell_B = 500$ nm, $B = 4$, and for different Debye lengths as indicated. The black line connects the minima.

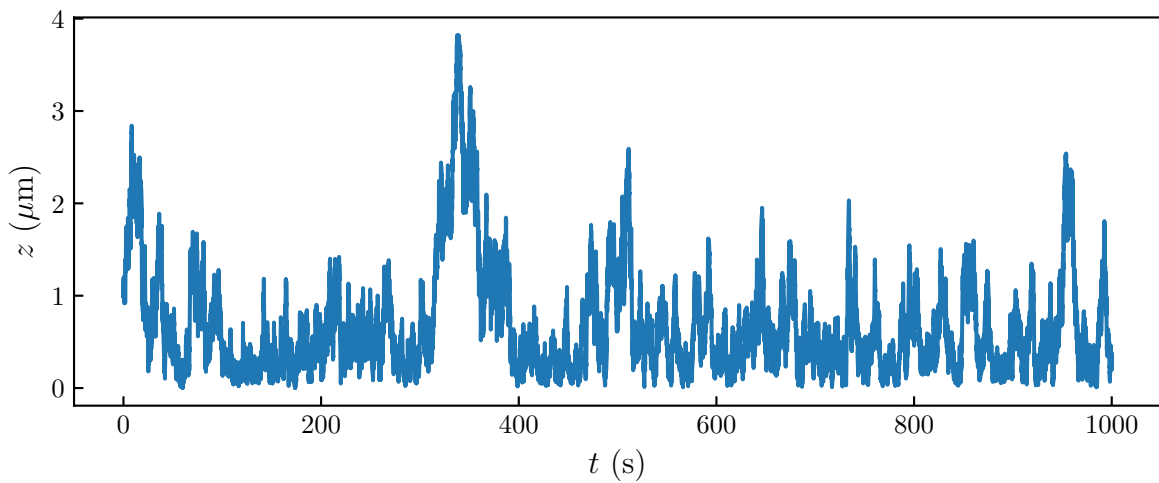


Figure 3.1.10: Simulated trajectory along the direction normal to the wall, using Eq. (3.1.77) with $\alpha = 1$ (isothermal convention), of radius $a = 1.5$ μm, density $\rho_p = 1050$ kg.m⁻³, placed in water near a wall. The particle-wall interaction is characterized by $\ell_D = 50$ nm and $B = 4$.

We have developed the numerical simulation of Eqs. (3.1.76) and (3.1.77) using Python, as part of the Master's internship of Élodie Millan. The interested reader will find more

information on the simulation of confined Brownian motion in complex systems in her forthcoming thesis. A typical trajectory of a water-immersed colloidal particle of radius $a = 1.5 \mu\text{m}$ and density $\rho_p = 1050 \text{ kg.m}^{-3}$, near a wall with which the electrostatic interaction is characterized by $\ell_D = 50 \text{ nm}$ and $B = 4$, is plotted in Fig. 3.1.10. It qualitatively resembles experimental trajectory that was shown in Fig. 3.1.1 as an introduction to the chapter. In this trajectory, the noise-induced lift is taken into account by using the isothermal convention (*i.e.* $\alpha = 1$). To check if the spurious drift is correctly implemented, the constraint we have is that the long-time statistics should satisfy Eq. (3.1.29). To compute an experimental probability density function from a set of points, one can use the following Python snippet.

```

1 def pdf(data, bins=10, density=True):
2
3     pdf, bins_edge = np.histogram(data, bins=bins, density=density)
4     bins_center = (bins_edge[0:-1] + bins_edge[1:]) / 2
5
6     return pdf, bins_center

```

The long-time PDF in position, for $\alpha = 0, 0.5$ and 1 are shown in Fig. 3.1.11. We see that the isothermal convention of the noise gives the correct distribution. In the other two cases, we observe that the particle is more likely to be found closer to the surface, as a result of the missing compensating spurious drift of Eq. (3.1.62). However, defining derivative in other way (*i.e.* Anti-itô or Stratonovich convention) would allow to employ any α values.

3.2 Experimental study

Let us now analyze the experimental data obtain through the Mie tracking (see section 2.3). In the theory, we considered distance z between the wall and the colloidal particle surface. However, it is not the height measured by the Mie tracking, since the latter measures the distance between the objective-lens focal plane and the particle center. To have the correct measured height, we suppose that the particle does approach very closely to the wall. From that assumption, we then a moving-minimum along the trajectory to set the minimal value of the trajectory to zero. The moving minimum can be calculated using the following Python function:

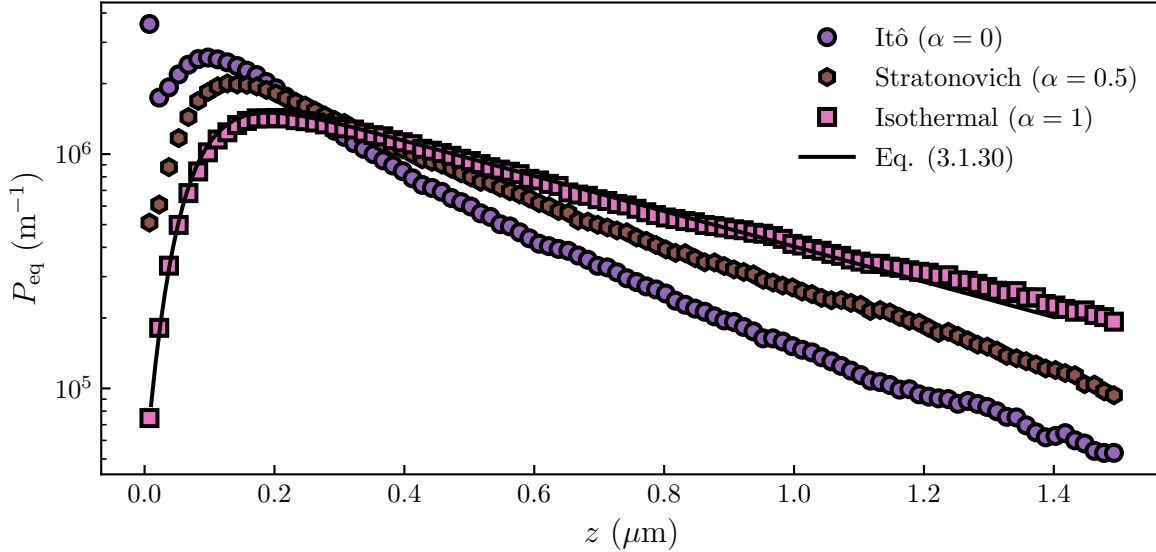


Figure 3.1.11: Simulated, Long-term Probability Density Function of the height of the particle for different convention as indicated. The solid black line represents the expected Gibbs-Boltzmann distribution. The physical parameters are: $a = 1.5 \mu\text{m}$, $\rho_p = 1050 \text{ kg.m}^{-3}$, $\ell_D = 50 \text{ nm}$, $B = 4$ and $\ell_B = 577 \text{ nm}$.

```

1 def movmin(z, window):
2     result = np.empty_like(z)
3     start_pt = 0
4     end_pt = int(np.ceil(window / 2))
5
6     for i in range(len(z)):
7         if i < int(np.ceil(window / 2)):
8             start_pt = 0
9         if i > len(z) - int(np.ceil(window / 2)):
10            end_pt = len(z)
11
12         result[i] = np.min(z[start_pt:end_pt])
13         start_pt += 1
14         end_pt += 1
15     return result

```

In the latter, `window` represent the number of points is used to compute the minimum. As an example, if one chose `window = 10000`, the first value of `result` is the minimum of the first 10000 points of `z`. If there is enough data around the point where the minimum is calculated, the ensemble is centered, with a window of 100, the minimal value at the 100th elements is between the 50th and 150th (*e.g.* `result[100] = np.min(z[50:150])`). The raw and rescaled trajectory are shown Fig. 3.2.1. Of course, that technique is not perfect and we are working on a method that could directly measure the wanted wall-particle

distance, also using Mie. However, subtract the moving minimum has a benefit, indeed it can remove some experimental drift that can be due to the physical movement of the optical pieces of the microscope. Moreover, as the exact location of the $z = 0$ origin is thus *a priori* undetermined we add to the physical parameters B , ℓ_D and ℓ_B a height offset z_{off} that accounts for the correction of the wall position.

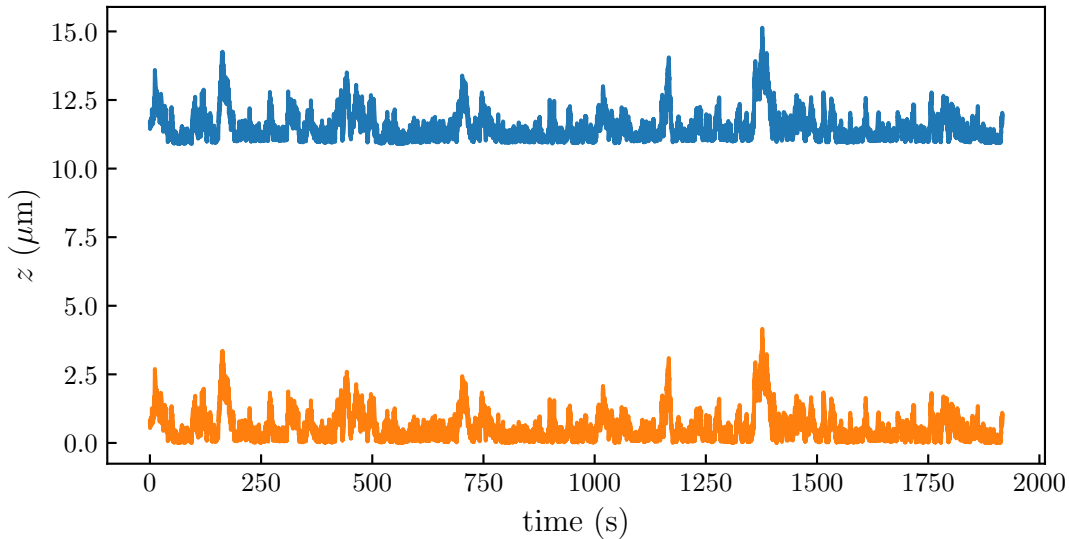


Figure 3.2.1: Raw trajectory measured using the Mie tracking technique, and it's rescaled value using moving minimum algorithm with a window of 10000 points.

3.2.1 Equilibrium distribution

As we have done for the simulated trajectory, one can construct the equilibrium probability density function $P_{\text{eq}}(z)$ of the position of the particle. As seen in Fig. 3.2.2, and explained in section 3.1.1, an exponential tail is observed at large distance, which is identified to the sedimentation contribution in Perrin's experiment [48], but here with the probability density function of a single particle instead of the concentration field. In contrast, near the wall, we observe an abrupt depletion, indicating a repulsive electrostatic contribution. Additionally, we see that the Gibbs-Boltzmann distribution of Eq. (3.1.29) fits the data very well.

Moreover, as shown in Fig. 3.2.3, we recover the Debye relation, *i.e.* $\ell_D = 0.304/\sqrt{[\text{NaCl}]}$ (see Eq. (3.1.13)), with ℓ_D in nm, and where $[\text{NaCl}]$ is the concentration of salt in mol/L, with a prefactor corresponding to a single monovalent salt in water at room temperature [49]. Besides, we have verified, as shown in Fig. 3.2.3, that the dimensionless parameter B related to surface charges is constant in the studied salt-concentration range, thus excluding any nonlinear effect [63, 64] in our case.

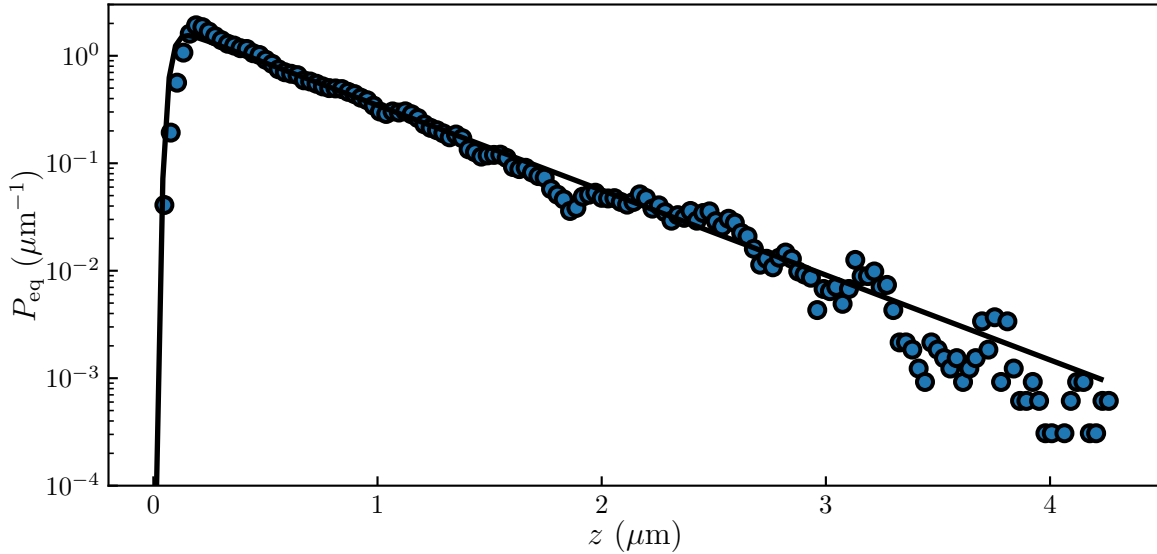


Figure 3.2.2: Measured equilibrium probability density function P_{eq} of the distance z between the particle and the wall. The solid line represents the best fit to the normalized Gibbs-Boltzmann distribution in position, using the total potential energy $U(z)$ of Eq. (3.1.28), with $B = 4.8$, $\ell_D = 21 \text{ nm}$, and $\ell_B = 530 \text{ nm}$.

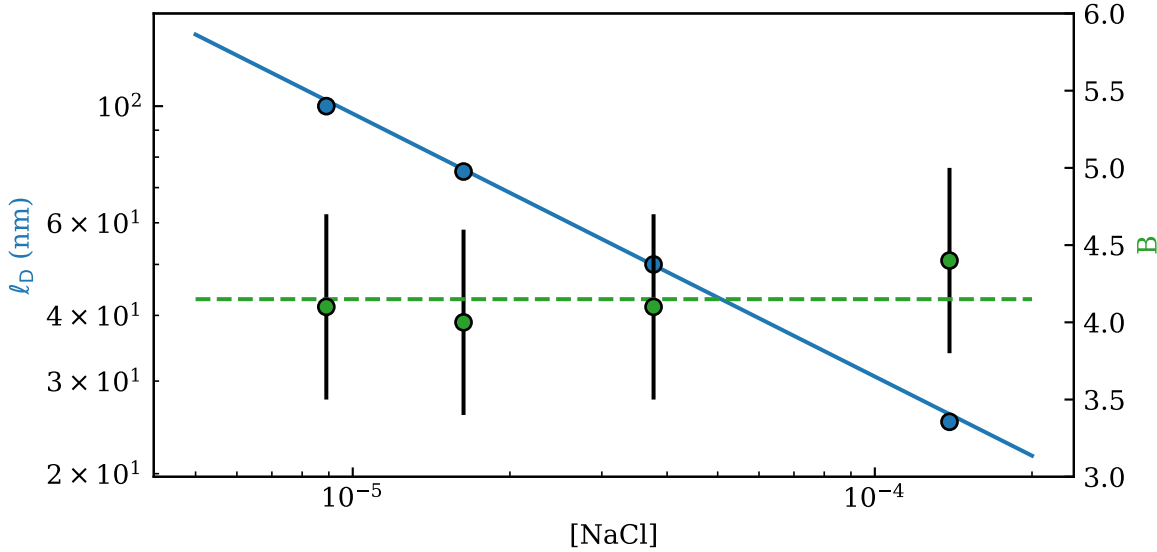


Figure 3.2.3: In blue, left axis, measured Debye length ℓ_D as a function of salt concentration $[\text{NaCl}]$. The solid line is the expected Debye relation $\ell_D = 0.304/\sqrt{[\text{NaCl}]}$, for a single monovalent salt in water at room temperature. In green, right axis, measured B as a function of salt concentration $[\text{NaCl}]$. The dashed line represents the mean value of the measured B values.

3.2.2 Mean Square Displacement

We now turn to dynamical aspects, by considering the mean-squared displacement (MSD). We recall that, for the three spatial directions, indexed by $i = x, y$, and z , corresponding to the coordinates $r_x = x$, $r_y = y$, and $r_z = z$, of the position \vec{r} , and for a given time increment Δt , the MSD is defined as:

$$\langle \Delta r_i(t)^2 \rangle_t = \langle [r_i(t + \Delta t) - r_i(t)]^2 \rangle_t , \quad (3.2.1)$$

where the average $\langle \cdot \rangle_t$ is performed over time t . For a free Brownian motion in the bulk, and in the absence of other forces than the dissipative and random ones, the MSD is linear in time, *i.e.* $\langle \Delta r_i(t)^2 \rangle_t = 2D_0\Delta t$, where D_0 is the bulk diffusion coefficient (see Eq. (3.1.33)) given by the Stokes-Einstein relation [2]. Further including sedimentation restricts the validity of the linearity of the MSD along the z -axis to short times only, *i.e.* for $\Delta t \ll \ell_B^2/D_0$ such that the vertical diffusion is not yet affected by the gravitational drift.

As explained in section 3.1.2.1 The presence of a rigid wall at $z = 0$ adds a repulsive electrostatic force along z . It also decreases the mobilities nearby through hydrodynamic interactions (see section 3.1.3), where we recall that it leads to effective viscosities $\eta_{\parallel}(z) = \eta_x(z) = \eta_y(z)$, and $\eta_{\perp}(z) = \eta_z(z)$ (see Eq. 3.1.45). Interestingly, despite the previous modifications, the temporal linearity of the MSD is not altered by the presence of the wall [46, 65] for x and y , as well as at short times for z . In such cases, the MSD reads:

$$\langle \Delta r_i(t)^2 \rangle_t = 2\langle D_i \rangle \Delta t , \quad (3.2.2)$$

where we introduced and the average of the local diffusion coefficient:

$$\langle D_i(z) \rangle = \int_0^\infty dz D_i(z) P_{\text{eq}}(z) , \quad (3.2.3)$$

against the Gibbs-Boltzmann distribution in position. As shown in Fig. 3.2.4, the MSD measured along x or y is indeed linear in time. By fitting the data to Eq. (3.2.2), using Eqs. (3.1.28) and (3.1.47), we extract an average transverse diffusion coefficient $\langle D_{\parallel} \rangle = \langle D_x \rangle = \langle D_y \rangle = 0.52 D_0$. In contrast, along z , we identify two different regimes: one at short times, where the MSD is still linear in time, with a similarly-obtained best-fit value of $\langle D_z \rangle = 0.24 D_0$; and one at long times, where the MSD saturates to a plateau. This latter behavior indicates that the equilibrium regime has been reached, with the particle having

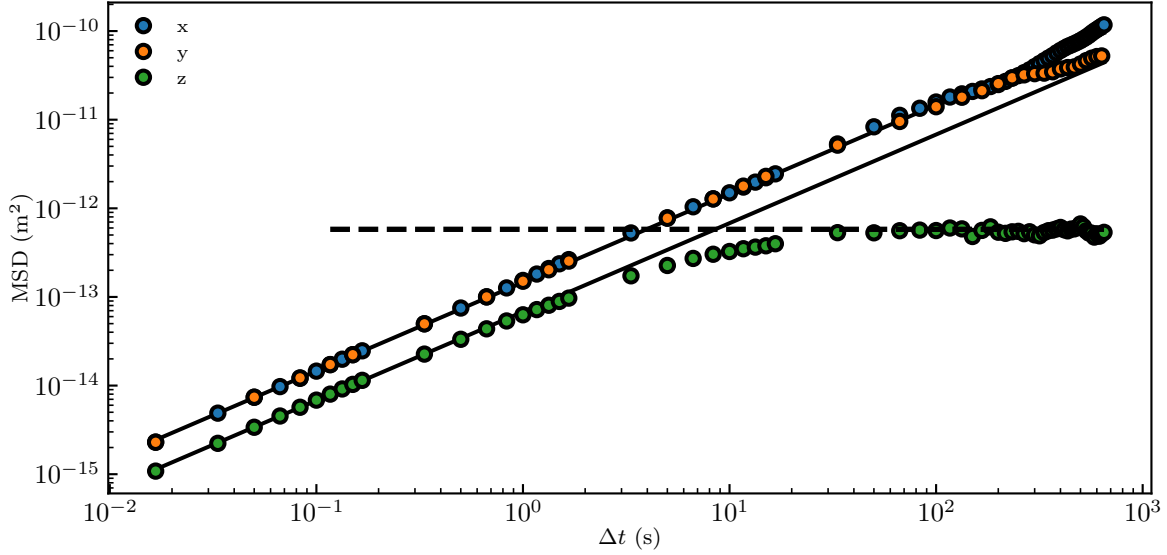


Figure 3.2.4: Measured mean-squared displacements (MSD, see Eq. (3.2.1)) as functions of the time increment Δt , for the three spatial directions, x , y , and z . The solid lines are best fits to Eq. (3.2.2), using Eqs. (3.1.28), (3.1.46) and (3.1.47), with $B = 4.8$, $\ell_D = 21$ nm, and $\ell_B = 530$ nm, providing the average diffusion coefficients $\langle D_{\parallel} \rangle = \langle D_x \rangle = \langle D_y \rangle = 0.52 D_0$ and $\langle D_z \rangle = 0.24 D_0$. The dashed line is the best fit to Eq. (3.2.9), using Eq. (3.1.28), with $B = 4.8$, $\ell_D = 21$ nm, and $\ell_B = 530$ nm.

essentially explored all the relevant positions given by the Gibbs-Boltzmann distribution.

3.2.3 Non-Gaussian dynamics - displacement distribution

Having focused on the MSD, *i.e.* on the second moment only, we now turn to the full Probability Density Function P_i of the displacement Δr_i . Since the diffusion coefficient $D_i(z)$ varies as a result of the variation of z along the particle trajectory, P_i exhibits a non-Gaussian behavior, as seen in Figs. 3.2.5-a,b,c,d). We even resolve the onset of a non-Gaussian behavior in P_x , by zooming on the large- $|\Delta x|$ wings. At short times, the diffusion coefficient D_i and the drift velocity \bar{v}_d , can be considered constant. By writing the initial condition of the particle-wall distance $\delta(z - z_0)$, the solution of Eq. (3.1.75) becomes:

$$\begin{aligned} P_z(z, z_0, \Delta t) &= \exp \left[\frac{\partial^2}{\partial z^2} D_{\perp}(z_0) \Delta t - \frac{\partial}{\partial z} \bar{v}_d(z_0) \Delta t \right] \frac{1}{2\pi} \int_{-\infty}^{\infty} du \exp(ju(z - z_0)) \\ &= \frac{1}{2\pi} \int_{-\infty}^{\infty} du \exp \left[-u^2 D_{\perp}(z_0) \Delta t + ju(z - z_0) - ju \bar{v}_d(z_0) \Delta t \right]. \end{aligned} \quad (3.2.4)$$

The latter can be reduced to [62, 66]:

$$P_z(\Delta z, z_0, \Delta t) = \frac{1}{\sqrt{4\pi D_i(z_0)\Delta t}} \exp\left[-\frac{(\Delta r_i - \bar{v}_d \Delta t)^2}{4D_i(z_0)\Delta t}\right], \quad (3.2.5)$$

which is a Gaussian distribution with a mean value $\langle \Delta z \rangle = \bar{v}_d \Delta t$. The same calculus can be done for the x - and y -axes, by setting the drift velocity to zero and using D_{\perp} . Additionally, it has a standard deviation $\sigma_i(z_0) = \sqrt{2D_i(z_0)\Delta t}$. From Eq. (3.2.5), we can observe than the total drift \bar{v}_d induces an asymmetry on the displacement along the z -axis. However, in our experiment, as we have access to long-enough trajectories to reach equilibrium, we are conditioned by the initial position but by the Gibbs-Boltzmann distribution of Eq. (3.1.29). At short times, P_i can thus be modeled by the averaged diffusion Green's function [67, 68]:

$$\begin{aligned} P_i(\Delta r_i, \Delta t) &= \int_0^\infty dz P_{\text{eq}}(z) P(\Delta r_i, z, \Delta t) \\ &= \int_0^\infty dz P_{\text{eq}}(z) \frac{1}{\sqrt{4\pi D_i(z)\Delta t}} e^{-\frac{\Delta r_i^2}{4D_i(z)\Delta t}}, \end{aligned} \quad (3.2.6)$$

against the Gibbs-Boltzmann distribution. Thee latter equation can alternatively be written as an integral over the diffusion coefficient such that:

$$P_i(\Delta r_i, \Delta t) = \int_0^\infty dD_i P(D_i) \frac{1}{\sqrt{4\pi D_i \Delta t}} e^{-\frac{\Delta r_i^2}{4D_i \Delta t}} \quad (3.2.7)$$

This equation can be evaluated using the following Python snippet.

```

1 def P_D(B, ld, lb):
2     # Computing the D PDF.
3     z = np.linspace(1e-9, 15e-6, 1000)
4     P_D = Dz(z) * P_b_off(z, offset, B, ld, lb)
5     P_D = P_D / np.trapz(P_D, z)  # extra step to ensure PDF normalization
6     return Dz, P_D
7
8
9 def _P_Dz_short_time(Dz, Dt, B, ld, lb):
10    # Using the D PDF to compute P()
11    D_z, P_D = P_D(B, ld, lb)
12    P = P_D / np.sqrt(4 * np.pi * D_z * Dt) * np.exp(-(Dz ** 2) / (4 * D_z * Dt))
13    P = np.trapz(P, D_z)
14    return P
15
16

```

```

17      # Creating a handy function for easier use with Dz numpy arrays
18 def P_Dz_short_time(Dz, Dt, B, ld, lb):
19     P = np.array([_P_Dz_short_time(i, Dt, B, ld, lb) for i in Dz])
20     P = P / np.trapz(P, Dz) # extra step to ensure PDF normalization
21     return P

```

In this snippet, the evaluation is done for Δz . However, when computing $P_x(\Delta x)$ one should just change the $Dz(z)$ function to D_{\parallel} . Since P is a PDF, it should be normalized such that $\int P = 1$. We added an extra step to ensure PDF normalization along the evaluation. At long time enough, since we have reached equilibrium, the averaged particle's drift should be equal to zero thus leading to a mean value $\langle \Delta r_i \rangle_t = 0$. As shown in Figs.3.2.5-a,c,b,d) Eq. (3.2.6) captures the early data very well. At long times, Eq. (3.2.6) remains valid only for P_x and P_y . Nevertheless, the equilibrium regime being reached, P_z only depends on the Gibbs-Boltzmann distribution. Indeed, in this regime P_z can be written as a convolution of two Gibbs-Boltzmann distribution as in a displacement $\Delta z = z(t + \Delta t) - z(t)$, $z(t + \Delta t)$ and $z(t)$ comes from independent draw from the Gibbs-Boltzmann distribution:

$$\lim_{\Delta t \rightarrow \infty} P_z(\Delta z, \Delta t) = \int_0^{\infty} dz P_{\text{eq}}(z + \Delta z) P_{\text{eq}}(z), \quad (3.2.8)$$

which contains in particular the second moment:

$$\lim_{\Delta t \rightarrow \infty} \langle \Delta z^2 \rangle = \int_{-\infty}^{+\infty} d\Delta z \Delta z^2 \int_0^{\infty} dz P_{\text{eq}}(z + \Delta z) P_{\text{eq}}(z). \quad (3.2.9)$$

As shown in Fig. 3.2.5-e), Eq. (3.2.8) captures the long-term data along z very well. Additionally, Eq. (3.2.9) permits to fit the long-term plateau of the MSD shown in Fig. 3.2.4. Eq. (3.2.8) can be evaluated using the following Python function:

```

1 def _Pdeltaz_long(DZ, B, ld, lb):
2     z = np.linspace(0, 20e-6, 1000)
3     dP = P_eq(z, B, ld, lb) * P_eq(z + DZ, B, ld, lb)
4     P = trapz(dP,z)
5     return P
6
7 def Pdeltaz_long(DZ, B, ld, lb):
8     pdf = np.array([_Pdeltaz_long(i,B, ld, lb) for i in DZ])
9     pdf = pdf / trapz(pdf,DZ)
10    return pdf
11

```

Wwere the P_{eq} function has been described in section 3.1.2.

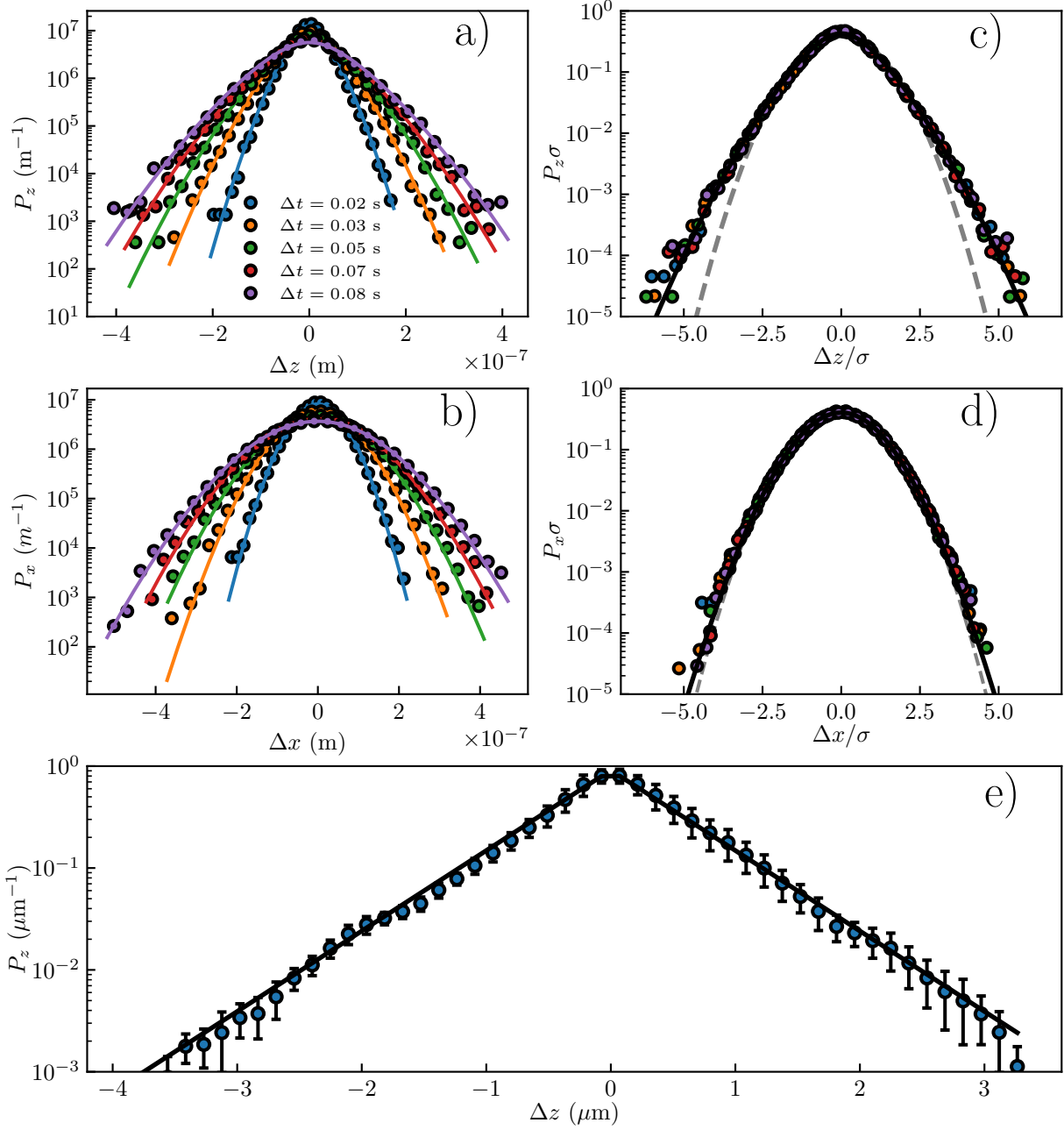


Figure 3.2.5: a, b) Probability density functions P_i of the displacements Δx and Δz , at short times. The solid lines are the best fits to Eq. (3.2.6), using Eqs. (3.1.29), (3.1.46), and (3.1.47), with $B = 4.8$, $\ell_D = 21 \text{ nm}$, and $\ell_B = 530 \text{ nm}$. c,d) Normalized probability density functions $P_i \sigma$ of the normalized displacements $\Delta x / \sigma$ and $\Delta z / \sigma$, at short times, with σ^2 the corresponding MSD (see Fig. 3.2.4), for different time increments Δt ranging from 0.0167 s to 0.083 s, as indicated with different colors. The solid lines are the best fits to Eq. (3.2.6), using Eqs. (3.1.28), (3.1.46), and (3.1.47), with $B = 4.8$, $\ell_D = 21 \text{ nm}$, and $\ell_B = 530 \text{ nm}$. For comparison, the gray dashed lines are normalized Gaussian distributions, with zero means and unit variances. d) Probability density function P_z of the displacement Δz , at long times, averaged over several values of Δt ranging between 25 s and 30 s. The solid line is the best fit to Eq. (3.2.8), using Eq. (3.1.28), with $B = 4.8$, $\ell_D = 21 \text{ nm}$, and $\ell_B = 530 \text{ nm}$.

3.2.4 Local diffusion coefficient inference

We now wish to go beyond the previous average $\langle D_i \rangle$ of Eq. (3.2.2), and resolve the local diffusion coefficient $D_i(z)$. To measure local viscosity from experimental trajectories, a binning method is generally employed [69]. This method consists of constructing the displacement PDF conditioned on the particle height, a measure the distribution's variance $\sigma_i(z_0) = \sqrt{2D_i(z_0)\Delta t}$ as in Eq. (3.2.5).

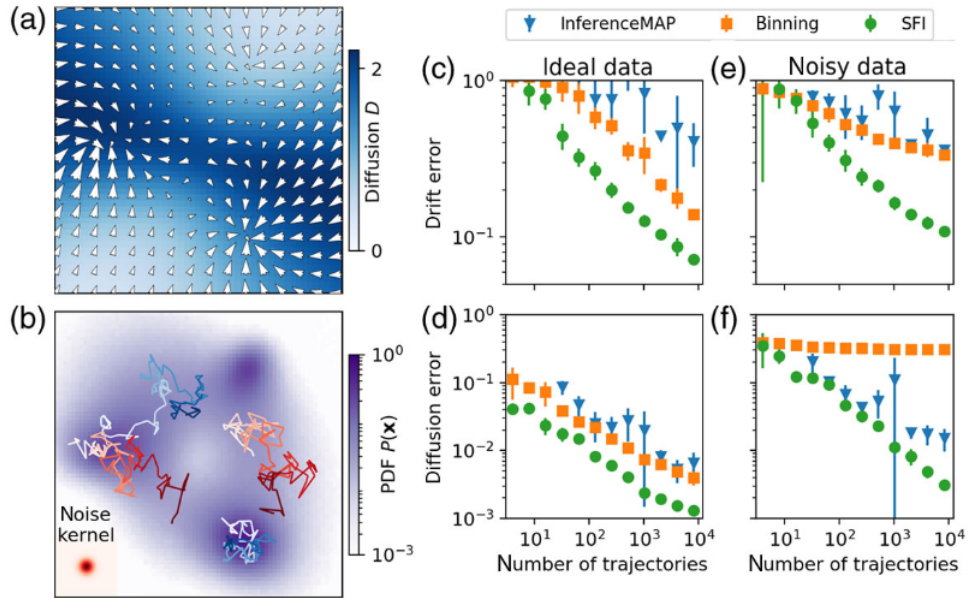


Figure 3.2.6: Figure from [70]. Quantitative comparison of Surface Force Inference (SFI) with other methods on a simulated system mimicking 2D single-molecule trajectories in a complex environment with space-dependent isotropic diffusion. a) The diffusion field (blue gradient) and drift field (white arrows). b) The steady-state distribution function (PDF) of the process. The traces are representative trajectories of 100 time steps. c-f) Comparison of the performance of SFI and two widely used inference methods: InferenceMAP, a method for single-molecule inference (blue triangles) [71], and grid-based binning with maximum-likelihood estimation [69, 72] (orange squares). They evaluated the performance of these methods on the approximation of the drift field (c,e)) and diffusion field (d,f)) as a function of the number N of single-molecule trajectories (similar to the ones in panel b)) used. With ideal data (c,d)) and in the presence of measurement noise(e,f)). The performance is evaluated as the average mean-squared error on the reconstructed field along trajectories. SFI outperforms both other methods in all cases. More information about the parameters of their simulation and analysis can be found in their work [70].

Although the binning method is well suited for drift measurements, it suffers from a lack of convergence and precision when second moments or local diffusion coefficients have to be extracted. In particular, the binning method did not allow us to measure specifically the local diffusion coefficient in the key interfacial region corresponding to

$z < 100$ nm. Indeed, as we can observe in the Fig. 3.2.6-f) the diffusion error on noisy (such as experimental) data does saturate of the binning method is outperformed by a robust developed method recently developed by Frishman and Ronceray [70]. This method uses Stochastic Force Inference (SFI), in order to evaluate spatially varying force fields and diffusion coefficients, from the information contained within the trajectories.

In practice SFI can reconstruct force and diffusion fields and measure entropy production from Brownian trajectories. SFI is based on the communication-theory notion of capacity which is an information-theoretic bound, when the system is viewed as a communication channel, that limit at which rate information about the fields can be extracted from a Brownian trajectory. To explain the method, let us consider a Brownian particle that obey to the equation similar to Eq. (3.1.63), using μ to denotes the x -, y - and z -axis:

$$\dot{x}_\mu = F_\mu(x) + \partial_\nu D(x)_{\mu\nu} + \sqrt{2D(x)}_{\mu\nu} dB_t , \quad (3.2.10)$$

where the Einstein summation is used over repeated indices, and the force field $F_\mu(x)$ and the diffusion tensor $D_{\mu\nu}$ are assumed to be time-independent. This method is built to measure the entire diffusion matrix, which for a particle diffusing above a wall has non-zero the diagonal term (*i.e.* D_{xx} , D_{yy} and D_{zz}). However, for more complex environment such as cellular environment as shown in Fig. 3.2.6-a), non-diagonal terms exist leading to correlations between the displacement axis. As an example, it has been observed in elastohydrodynamics [73] that the parallel movement near a soft wall can induce perpendicular forces, hence leading in that peculiar case, to correlation between the x and z movement. The SFI idea is to approximate the diffusion field as a linear combination of a basis of n_b known functions $b = b_\alpha(x)_{\alpha=1,\dots,n_b}$. For the diffusion of spherical spheres near a wall where the diffusion coefficient is given by the Eqs. (3.1.46) and (3.1.47) we got robust results using their built-in polynomial basis:

$$b = \{b_\alpha(x)\}_{\alpha=1,\dots,n_b} = \{1, x_\mu, x_\mu x_\nu, \dots\} \text{ (up to the order } n_b \text{).} \quad (3.2.11)$$

They perform this approximation by projecting the diffusion field onto the space spanned by $b_\alpha(x)$ using the position PDF, P_{eq} (see Eq. (3.1.28)) as a measure. This corresponds to a least-squares fit of the diffusion field by linear combinations of the b_α 's. To do this fit, they define a projector:

$$c_\alpha(x) = B_{\alpha\beta}^{1/2} b_\beta(x) , \quad (3.2.12)$$

where $B_{\alpha\beta}^{1/2}$ is an orthonormalization matrix such that $\int c_\alpha c_\beta P_{\text{eq}}(x)dx = \delta_{\alpha\beta}$. They then approximate $D_{\mu\nu}$ by its projection as a linear combination of known functions:

$$D_{\mu\nu}(x) \simeq D_{\mu\nu\alpha} c_\alpha(x) , \quad (3.2.13)$$

with,

$$D_{\mu\nu\alpha} = \int D_{\mu\nu}(x) c_\alpha(x) P_{\text{eq}} dx . \quad (3.2.14)$$

As the equation here are over a whole trajectory which is long enough to satisfy P_{eq} , the empirical projector \hat{c}_α can be approximated using the trajectory averages. To measure the local diffusion they construct a local estimator $\hat{d}_{\mu\nu} = \Delta x_\mu(t_i)\Delta x_\nu(t_i)/2\Delta t$, so that $D_{\mu\nu\alpha}$ now reads:

$$\hat{D}_{\mu\nu\alpha} = \frac{1}{\tau} \sum_i \hat{d}_{\mu\nu}(t_i) \hat{c}_\alpha(x(t_i)) \Delta t . \quad (3.2.15)$$

The latter equation corresponds to a linear regression of $\hat{d}_{\mu\nu}(t_i)$, and permits to project the diffusion tensor onto a finite set of basis functions. We implemented this method, using fourth-order polynomials in our case. to simplify the use of their method with our data, I developed a simple Python function around their method **Q** which can infer the local diffusion coefficient by only one function call:

¹ `Dx, Dy, Dz, z_D = Compute_diffusion(pos)`

Where in the latter `pos`, is the 3D trajectory of a Brownian colloid. It allowed us to infer the local diffusion coefficients $D_i(z)$, down to $z = 10$ nm, as shown in Fig. 3.2.7. The results are in excellent agreement with the theoretical predictions, $D_{\parallel}(z)$ and $D_z(z)$, using Eqs. (3.1.46) and (3.1.46), thus validating the method.

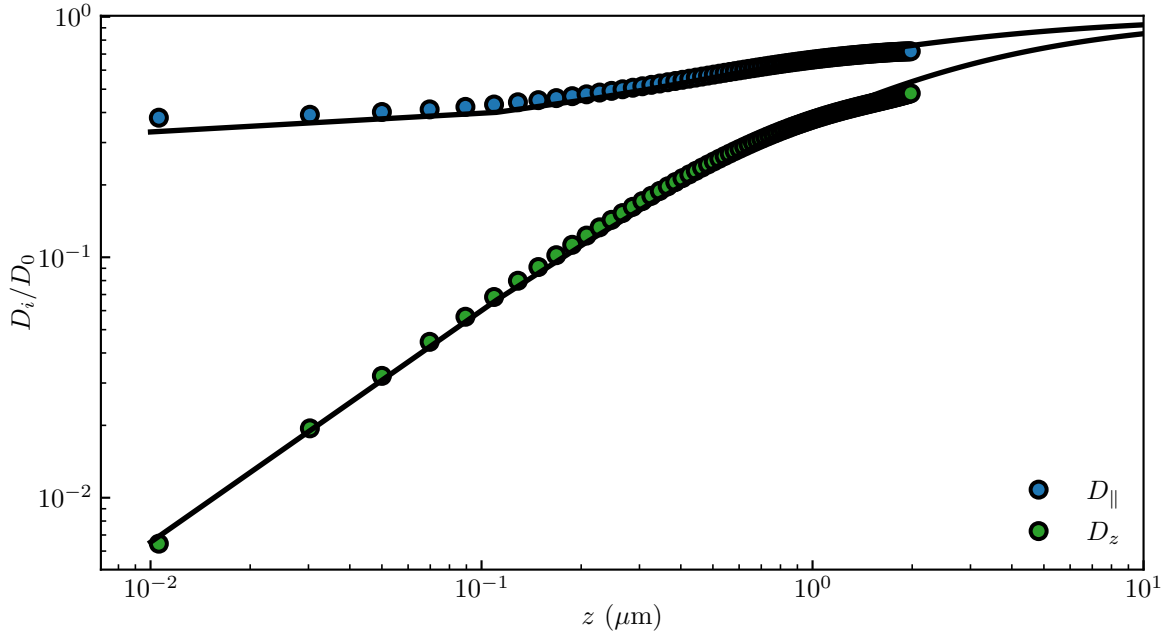


Figure 3.2.7: Measured local short-term diffusion coefficients D_i of the microparticle, normalized by the bulk value D_0 , as functions of the distance z to the wall, along both a transverse direction x or y ($D_i = D_{\parallel} = D_x = D_y$, blue) and the normal direction z ($D_i = D_z$, green) to the wall. The solid lines are the theoretical predictions, $D_{\parallel}(z) = D_0 \eta_{\parallel}(z)/\eta(z)$ and $D_z(z) = D_0 \eta_{\perp}(z)/\eta(z)$, using the local effective viscosities $\eta_{\perp}(z)$ and $\eta_{\parallel}(z)$ of Eqs. (3.1.46) and (3.1.46), respectively.

3.2.5 Precise potential inference using multi-fitting technique

So far, through Figs. 3.2.2-3.2.7, we have successively presented the various measured statistical quantities of interest, as well as their fits to corresponding theoretical models. Therein, we have essentially three free physical parameters, B , ℓ_B , ℓ_D , describing the particle and its environment, as well as the *a priori* undetermined location of the $z = 0$ origin. These four parameters are actually redundant among the various theoretical models. Therefore, in order to measure them accurately, we in fact perform all the fits simultaneously, using a Broyden-Fletcher-Goldfarb-Shanno (BFGS) algorithm that is well suited for unconstrained nonlinear optimization [74]. To do so, we construct a global minimizer:

$$\chi^2 = \sum_{n=1}^N \chi_n^2, \quad (3.2.16)$$

where we introduce the minimizer χ_n^2 of each set n among the N sets of data, defined as:

$$\chi_n^2 = \sum_{i=1}^{M_n} \frac{[y_{ni} - f_n(x_{ni}, \mathbf{b})]^2}{f_n(x_{ni}, \mathbf{b})^2}, \quad (3.2.17)$$

with $\{x_{ni}, y_{ni}\}$ the experimental data of set n , M_n the number of experimental data points for set n , f_n the model for set n , and $\mathbf{b} = (b_1, b_2, \dots, b_p)$ the p free parameters. In our case, $p = 4$, and $\{x_{ni}, y_{ni}\}$ represent all the experimental data shown in Figs.3.2.2-3.2.7.

Due to strong dependence of the normal diffusion coefficient D_z with z , it is possible to find the wall position with a 10 nm resolution, thus overcoming a drawback of the Lorenz-Mie technique which only provides the axial distance relative to the focus of the objective lens. Besides, the three physical parameters globally extracted from the multifitting procedure are: $B = 4.8 \pm 0.6$, $\ell_D = 21 \pm 1$ nm, and $\ell_B = 530 \pm 2$ nm. Using the particle radius $a = 1.518 \pm 0.006$ μm calibrated from the preliminary fits of the interference patterns to the Lorenz-Mie scattering function (see section 2.7.3), and the $\rho_p = 1050$ kg.m^{-3} tabulated bulk density of polystyrene, we would have expected $\ell_B = 559$ nm instead, which corresponds to less than 2 % error, and might be attributed to nanometric offsets, such as *e.g.* the particle and/or wall rugosity.

3.2.6 Measuring external forces using the local drifts

Finally, we investigate the total conservative force $F_z(z)$ acting on the particle along z . The first way to measure it is to calculate the gradient of the potential U which is experimentally measured from the position PDF giving:

$$F_z^{\text{eq}} = -\nabla U = k_B T \frac{d}{dz} \ln(P_{\text{eq}}) , \quad (3.2.18)$$

where one can use the experimentally measured P_{eq} (see Fig. 3.2.2). The results of this method are shown in Fig. 3.2.8. However, it can be interesting to measure the forces using the local drifts as for more complex systems, some non-conservative forces could arise. As the Eq. (3.2.18) takes only into account to the potential U , only conservative forces can be extracted from the measurement of P_{eq} . Non-conservative forces could be measured by the difference between forces obtained through P_{eq} and the local drifts.

By averaging the overdamped Langevin equation over a fine-enough z -binning grid and short enough time interval Δt , one gets in the Itô convention (corresponding to our definition of Δz):

$$F_z(z) = 6\pi\eta_z(z)a \frac{\langle \Delta z \rangle}{\Delta t} - k_B T \frac{D'_z(z)}{D_z(z)} , \quad (3.2.19)$$

where the last term corresponds to the additional contribution due to the non-trivial integration of the multiplicative noise [75–78], with the prime denoting the derivative with

respect to z . From the averaged measured vertical drifts $\langle \Delta z \rangle$, and invoking Eq. (3.1.48), one can reconstruct $F_z(z)$ from Eq. (3.2.19), as shown in Fig. 3.2.8. We stress that the statistical error on the force measurement is comparable to the thermal-noise limit [79]:

$$\Delta F = \sqrt{24\pi k_B T \eta_z(z) a / \tau_{\text{box}}(z)} , \quad (3.2.20)$$

where $\tau_{\text{box}}(z)$ is the total time spent by the particle in the corresponding box of the z -binning grid. To corroborate these measurements, we invoke Eq. (3.1.28) and express the total conservative force $F_z(z) = -U'(z)$ acting on the particle along z :

$$F_z(z) = k_B T \left(\frac{B}{\ell_D} e^{-\frac{z}{\ell_D}} - \frac{1}{\ell_B} \right) . \quad (3.2.21)$$

Using the physical parameters extracted from the above multifitting procedure, we plot Eq. (3.2.21) in Fig. 3.2.8. The agreement with the data is excellent, thus showing the robustness of the force measurement. In particular, we can measure forces down to a distance of 40 nm from the surface. Besides, far from the wall, we are able to resolve the actual buoyant weight $F_g = -7 \pm 4$ fN of the particle. This demonstrates that we reach the femtoNewton resolution, and that this resolution is solely limited by thermal noise.

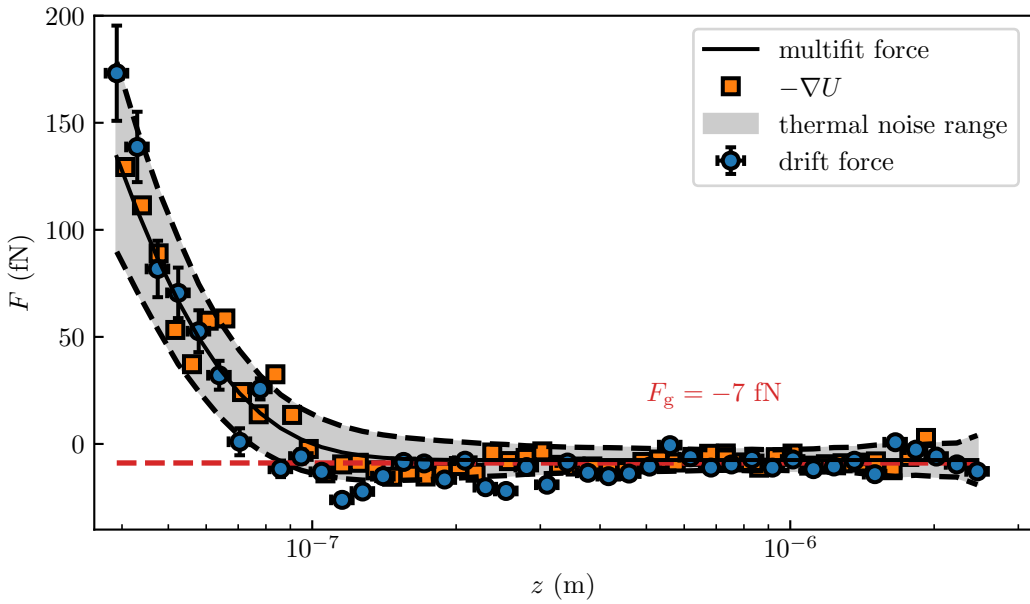


Figure 3.2.8: Total normal conservative force F_z exerted on the particle as a function of the distance z to the wall, reconstructed from Eq. (3.2.19), using Eq. (3.1.48) in circles and using Eq. (3.2.18) in squares. The solid line corresponds to Eq. (3.2.21), with $B = 4.8$, $\ell_D = 21$ nm and $\ell_B = 530$ nm. The black dashed lines and gray area indicate the amplitude of the thermal noise computed from Eq. (3.2.20). The horizontal red dashed line indicates the buoyant weight $F_g = -7$ fN of the particle.

3.3 Conclusion

To conclude, we have successfully built a multi-scale statistical analysis for the problem of freely diffusing individual colloids near a rigid wall. Combining the equilibrium distribution in position, time-dependent non-Gaussian statistics for the spatial displacements, a novel method to infer local diffusion coefficients, and a multifitting procedure, allowed us to reduce drastically the measurement uncertainties and reach the nanoscale and thermal-noise-limited femtoNewton spatial and force resolutions, respectively. The ability to measure tiny surface forces, locally, and at equilibrium, as well the possible extension of the method to non-conservative forces and out-of-equilibrium settings [80, 81], opens fascinating perspectives for nanophysics and biophysics.

4 Work in progress and observations

In this section, I will present some of the work that has been started but not finished yet, and observations made during the experiments.

4.1 Elastohydrodynamic lift at soft wall

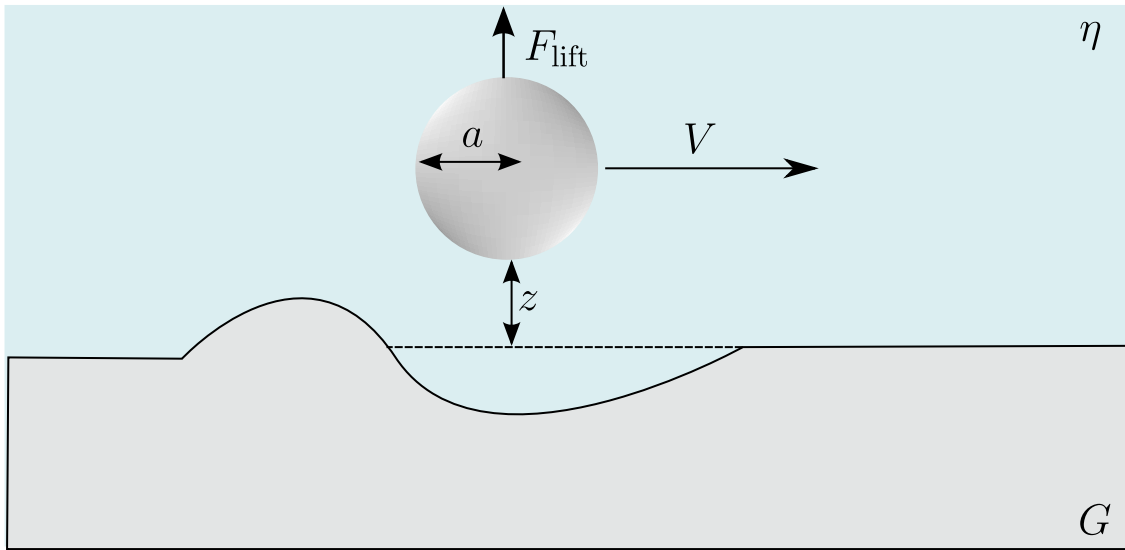


Figure 4.1.1: Schema of a spherical colloid of radius a immersed in a fluid of viscosity η sliding at a velocity V above an incompressible and linear-elastic substrate of shear elastic modulus G . From the elastohydrodynamic interactions between the particle and the soft wall arises a net lift force F_{lift} (see Eq. (4.1.1)).

Elastohydrodynamic (EHD) is the branch in physics that permits modeling the interaction between elasticity and hydrodynamic. We will here focus particularly focus to EHD in lubrication, which permits to model the physics of sliding motion between objects with a fluid-lubricated contact. Lubrication EHD is present in many length scales and time scales, including for example, landslides [82], roller bearings [83] or blood cells motion in microfluidic devices [84–86]. It is recently, in 2015, that the problem of a free particle that can sediment, slide or roll near a soft surface has been treated [87]. As the particle slides near the surface, they moved fluid deforms the soft wall surface. One of the main results of [87] is that sliding induced a symmetry breaking of the deformation; hence, a net force is applied to the sliding object. They further show that this force is oriented towards the particle, and, thus act EHD lift force. If a particle is sliding due to its own weight, this lift force can be self-sustained. The first experimental proof of this force has been done at the macro scale using negatively buoyant centimetric cylinders immersed in

a viscous fluid sliding down a tilted wall that is coated with an elastic layer. They show that the self-sustained EHD lift reduces the friction by nearly an order of magnitude and suggests that this EHD force could partially explain phenomena such as reduced wear in animal joints and long-runout landslides. The EHD lift force has also recently been measured at the micro-scale, using micron-sized colloidal spheres in micro channels in a shear flow. However, all of this experiment uses a system which is out of equilibrium, and, we would like to test if Brownian motion could trigger such an effect. In the soft lubrication theory, and taking a sphere of radius a moving at constant velocity V , in a solvent of viscosity η , at a distance z for a thick (with respect to the particle radius), incompressible, linear-elastic substrate of shears elastic modulus G , the lift force F_{lift} reads [88]:

$$F_{\text{lift}} \simeq \frac{\eta^2 V^2}{G} \frac{a^{5/2}}{z^{5/2}} . \quad (4.1.1)$$

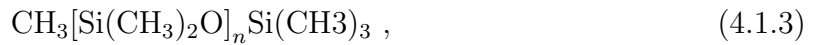
To incorporate fluctuations into this deterministic picture, an idea is to replace the velocity V in Eq. (4.1.1) by the typical Brownian velocity obtain through the Maxwell-Boltzmann distribution $\sqrt{k_B T/m}$, leading the following estimate of the Brownian EHD lift force:

$$F_{\text{lift,Brown}} \simeq \frac{\eta^2 k_B T}{G \rho_p a^{1/2} z^{5/2}} . \quad (4.1.2)$$

From this equation, we can observe a counterintuitive effect, as the particle radius decreases (the surface of contact), the larger the EHD force $F_{\text{lift,Brown}}$ is. Taking typical biophysics value such as $G \simeq 10$ kPa, $\rho_p = 1350$ kg.m⁻³ and $a = 100$ nm, the EHD force reaches the picoNewton order of magnitude. The latter means that microscopic entities in biology and nanoscience may spontaneously trigger large Brownian EHD couplings, drastically affecting their dynamics. However, it is important to note that it is a simple estimate and, contains a high risk of conceptual failure associated, for example, to the lack of compensating drift at equilibrium as we have with a hard wall (see Eq. (3.1.62)). To do the soft coating experimentally, we use Polydimethylsiloxane (PDMS).

4.1.1 PDMS

PDMS is a silicone-based organic polymer which is widely used due to its versatility and ease of use [89]. Its chemical formula is:



where n is the number of $\text{Si}(\text{CH}_3)_2\text{O}$ dimethyl groups. By mixing a solution of PDMS chains with curring agent containing, for example hydrosilane groups (SiH), bonds, or crosslink between different PDMS chains are appearing as shown in Fig. 4.1.2.

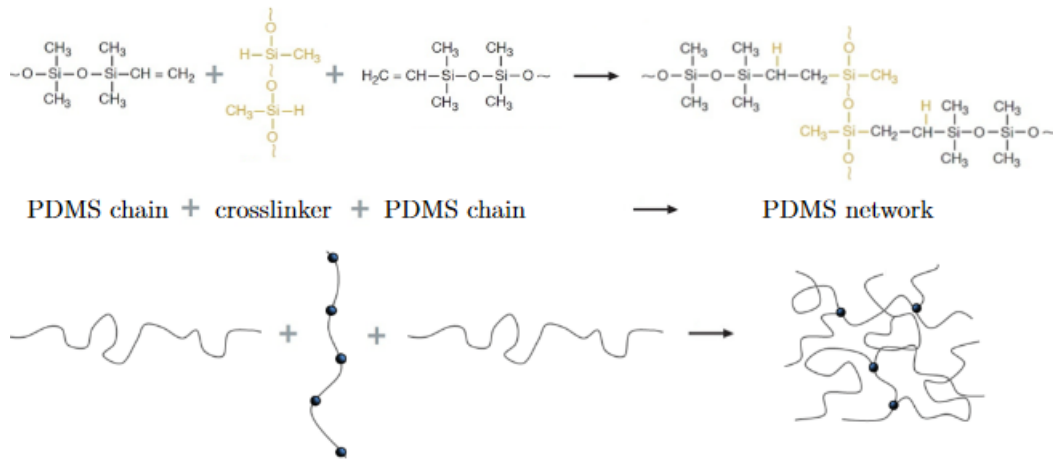


Figure 4.1.2: Figure taken from [90]. Examples of crosslinking reaction between the PDMS chains and a curing agent containing hydrosilane groups.

Due to this crosslink, the PDMS turns into an incomprehensible and linear-elastic solid. Some of its characteristics are to be hydrophobic and to exhibit strong gas permeability [91]. The elasticity modulus G of the crosslinked PDMS can be tuned by changing the mixing ratio of base polymer solutions and curing agent. For example, for one of the most used PDMS Sylgard 184, a mixing ratio of 10 : 1 leads to an elastic modulus $G = 1.5 \text{ MPa}$ and $G \simeq 100 \text{ kPa}$ for a 35 : 1 ratio [92]. To prepare experimental samples, it is possible to spin coat the microscope slides with the base:agent mix before it is cured in order to have a thick soft surface coating onto the slides. However, for simplicity and check if we can observe any forces with our experiment we first decided to use already prepared samples sold by Ibidi, these came as soft coated dishes with a coverslip on the bottom that we can directly fit onto our microscope.

4.1.2 Measuring non-conservative forces

To measure the non-conservative forces that a felt by a Brownian particle diffusing on top of a soft surface, we do the exact same experiment and data analysis as developed in the section 3.2. As the EHD force do not derive from a potential, we need to extract the

non-conservative forces F_{NC} at a distance of 100 nm from the wall, to do so, by combining Eqs. (3.2.18) and (3.2.21), the non-conservative force reads:

$$F_{NC} = F_z(z) - F_z^{\text{eq}}(z) \quad (4.1.4)$$

As seen in Fig. 4.1.3 the measured F_{NC} for two different elastic moduli $G = 15$ and 28 kPa, only gets out of the noise for $F_{NC} > 10$ fN, as the plot is in logarithmic scale negative values do not show. These first experiment shows that the particle seems to trigger some non-conservative forces. However, this first experiment is not sufficient to tell if it is the EHD lift force but give some support to continue the experiment.

In the forthcoming experiment, we will vary three parameters, η , G and a to check if we can prove the existence of a universal plot, and show the $F_{\text{lift},\text{Brown}}$ correctly varies as a function of $\frac{\eta^2}{Ga^{1/2}}$ as shown in Fig. 4.1.4 with the first experiments.

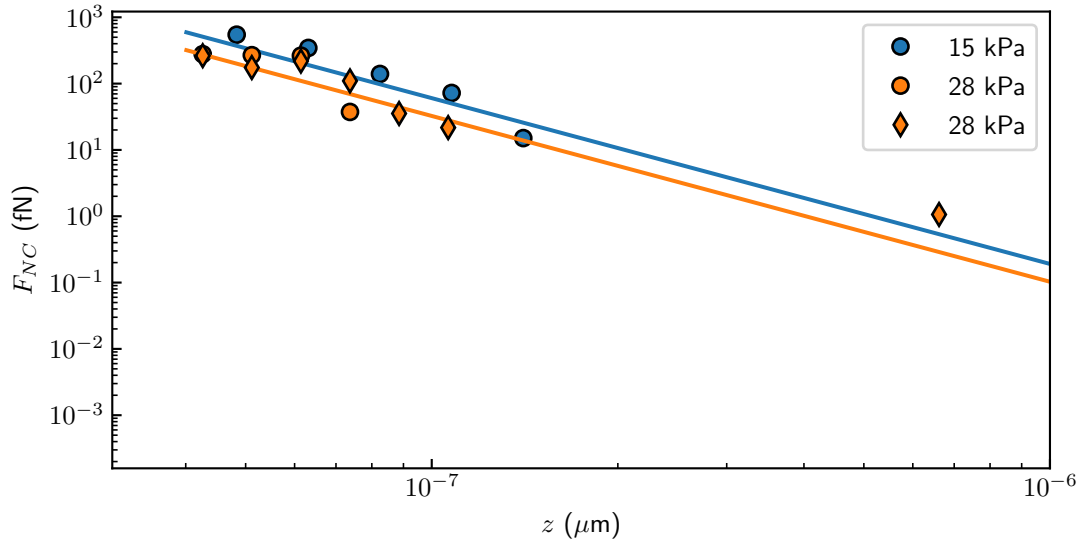


Figure 4.1.3: Non-conservative forces measured experimentally for colloidal particles of radius $a = 1.5 \mu\text{m}$ diffusing above an incompressible and linear-elastic substrate of shear elastic modulus $G = 15$ and 28 kPa. Plain line corresponds to the Brownian model of the EHD lift force $F_{\text{lift},\text{Brown}}$ (see Eq. (4.1.2)) with an added noise-level of 10 fN.

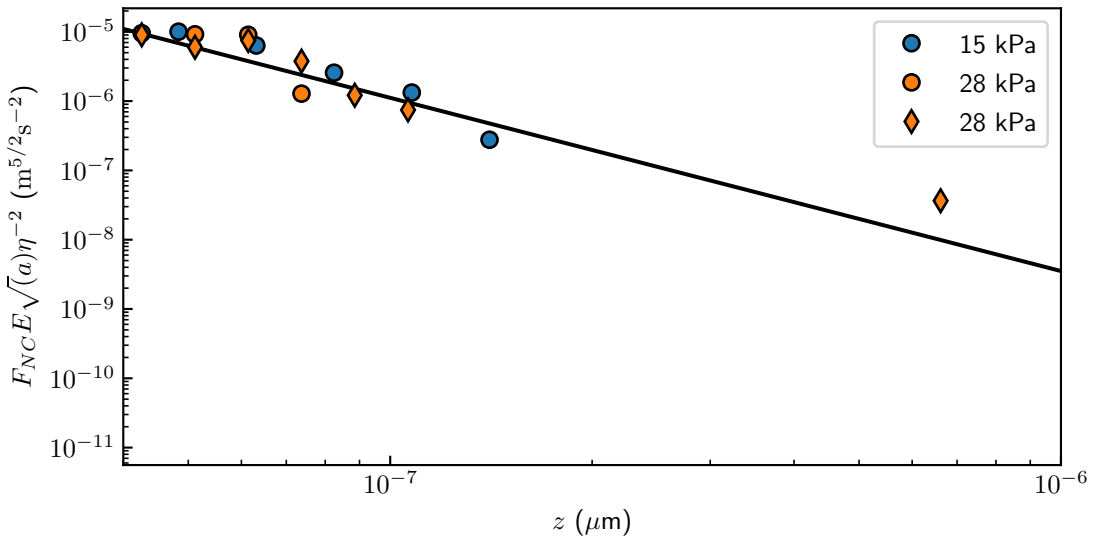


Figure 4.1.4: Non-conservative forces normalized $G\sqrt{a}$ by measured experimentally for colloidal particles of radius $a = 1.5 \mu\text{m}$ diffusing above an incompressible and linear-elastic substrate of shear elastic modulus $G = 15$ and 28 kPa . Plain line corresponds to the Brownian model of the EHD lift force $F_{\text{lift},\text{Brown}}$ (see Eq. (4.1.2)) with an added noise-level of 10 fN .

4.2 Close wall stuck motion

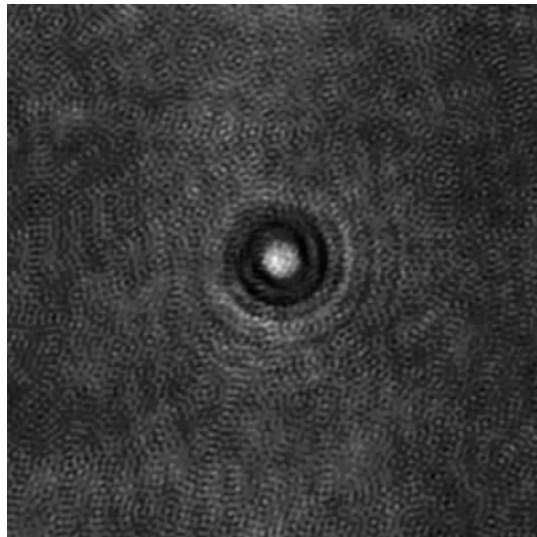


Figure 4.2.1: Median image of a stuck particle. The median is calculated over 120 images taken every 30 s.

As we have done the experiments to measure the Debye length ℓ_D as a function of the concentration of NaCl, we observed that some particle was stuck at the surface. As we

first expected, we were not observing any movement from the stuck particle. However, surprisingly we observe that some particle was slightly diffusing. This slight diffusion can be observed directly from the raw data, by looking at the median of the video, as shown Fig. 4.2.1, one can observe the “ghost” of the particle due to its movement in time. Moreover, as we cannot properly have the background in this experiment since the particle do not diffuse enough, the statistical error of the tracking is increased. The measured trajectory is shown Fig.4.2.2, we observe that mechanical drift happened during the experiment, this could be due to a drift of the sample or the objective, for example. This drift is of the order of magnitude of $2 \mu\text{m.h}^{-1}$ along the x - and y -axis and $6 \mu\text{m.h}^{-1}$, in the following we look at the short time dynamics ($t < 1 \text{ s}$), since the drift at this time scale is of the order of the nm it is not necessary to remove the drift from the trajectory.

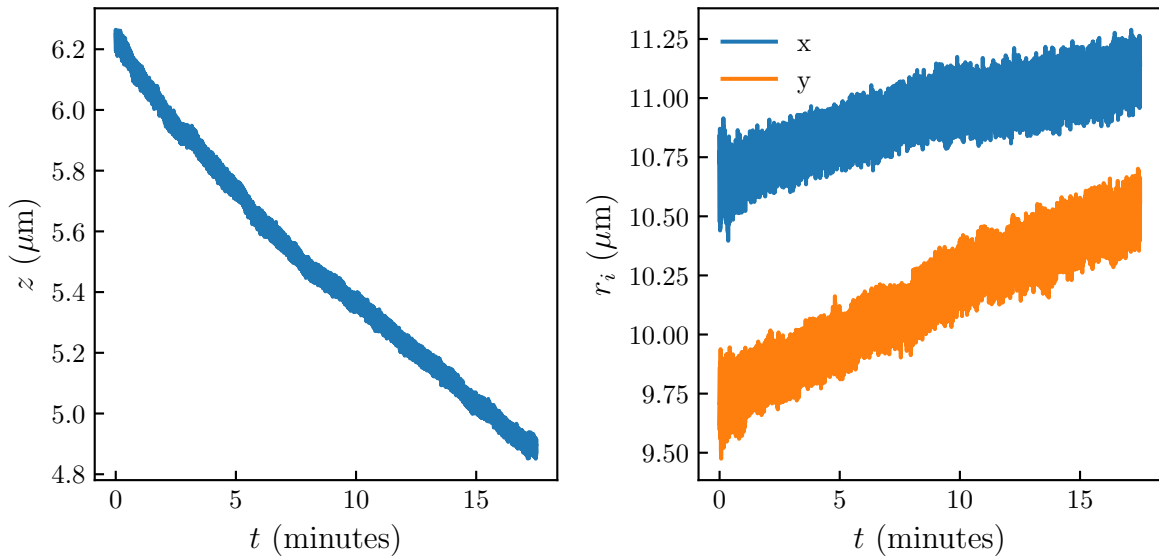


Figure 4.2.2: Raw trajectory measured using the Mie tracking technique for the x -, y - and z - axis of a particle of radius $a = 1.5 \mu\text{m}$. The time between each frame is $1/200 \text{ s}$.

Let's focus directly on the dynamics of the system, the MSD along the x -, y - and z -axis is shown in Fig. 4.2.3. We observe that the MSD along the z - axis is a constant, it can be the case because it moves less than the statistical error tracking, the experiment could thus be bound by the experimental precision, or, a diffusion regime could be at a shorter time. As we here can't observe any diffusion regime on the z -axis, we can't determine if we are bound the tracking; hence, I will not physically comment the results obtained along the z -axis. However, on the x -axis, interestingly we can observe two regimes as had for the z before meaning that the particle is diffusing in a potential which isotropic along the x - and y -axis, as if the particle was rolling on the surface due to the rugosity for example (NEED TO ASK YACINE FOR REF). The diffusive regime, at a short time, is linear with Δt showing a normal diffusion with average diffusion coefficients (see Eq. (3.2.2))

$\langle D_{\parallel} \rangle = \langle D_x \rangle = \langle D_y \rangle = 0.14 D_0$. This diffusion coefficient is lower than what is obtainable using the previous defined equation of D_{\parallel} , Eq. (3.1.47), which we do not explain.

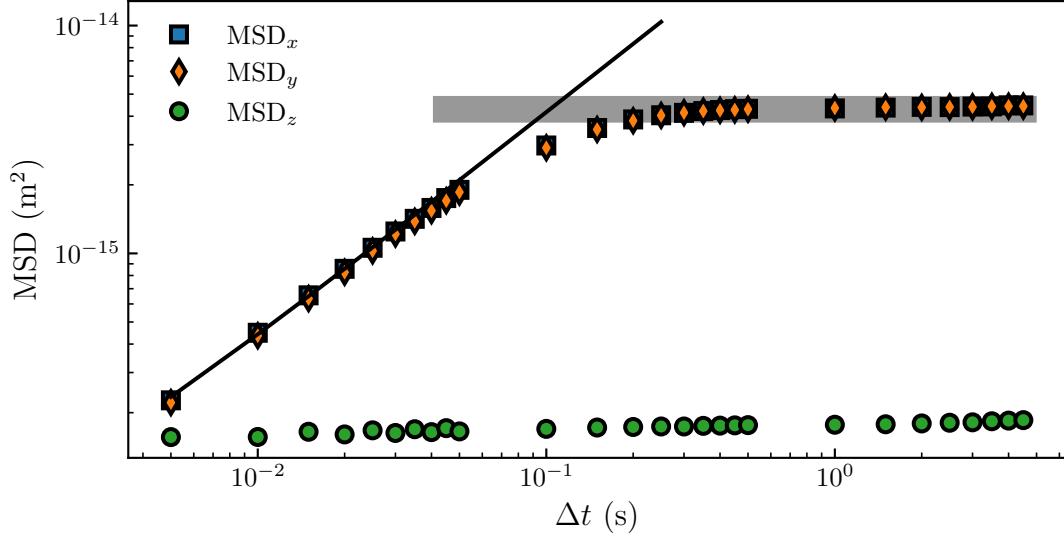


Figure 4.2.3: Measured mean-squared displacements of a stuck particle (MSD, see Eq. (3.2.1)) as functions of the time increment Δt , for the three spatial directions, x , y , and z . The solid line is the best fit to Eq. (3.2.2), having $\langle D_i \rangle$ as a free parameter, providing the average diffusion coefficient $\langle D_{\parallel} \rangle = \langle D_x \rangle = \langle D_y \rangle = 0.14 D_0$. The plain gray line is the average value of the plateau of the MSD along the x - and y -axis, providing $\lim_{\Delta t \rightarrow \infty} \langle \Delta x^2 \rangle = 4.3 \times 10^{-15} \text{ m}^2$.

The plateau of the MSD along the x and y gives a value of $\lim_{\Delta t \rightarrow \infty} \langle \Delta x^2 \rangle = 4.3 \times 10^{-15} \text{ m}^2$. By supposing that the particle is in a harmonic oscillator potential, we can make an estimate of the spring constant k_H , using the relation:

$$k_H = \frac{2k_B T}{\lim_{\Delta t \rightarrow \infty} \langle \Delta x^2 \rangle} = \frac{8 \times 10^{-21}}{4.3 \times 10^{-15}} \simeq 2 \mu\text{N.m}^{-1}. \quad (4.2.1)$$

An idea we have is to try to observe the same phenomenon using a soft surface and see if we can observe a change of k_H as a function of the elastic modulus G . If the latter assumption is possible, this experiment could lead to local determination of elastic modulus using Brownian probes. Additionally, we can look at displacement PDF P_i as shown on the Fig. 4.2.4. Contrary to the result we had for a free diffusing particle (See Fig. 3.2.5) we do not observe non-Gaussianity. Moreover, distribution P_z seems to corroborate with the fact that we are bound to the fit error on the fit along the z -axis. Indeed, if the particle is at equilibrium, which should be the case with a MSD being constant, P_z should be given by exponential as shown in Fig. 3.2.5-e). Here P_z looks like

a Gaussian distribution of the fit statistical error.

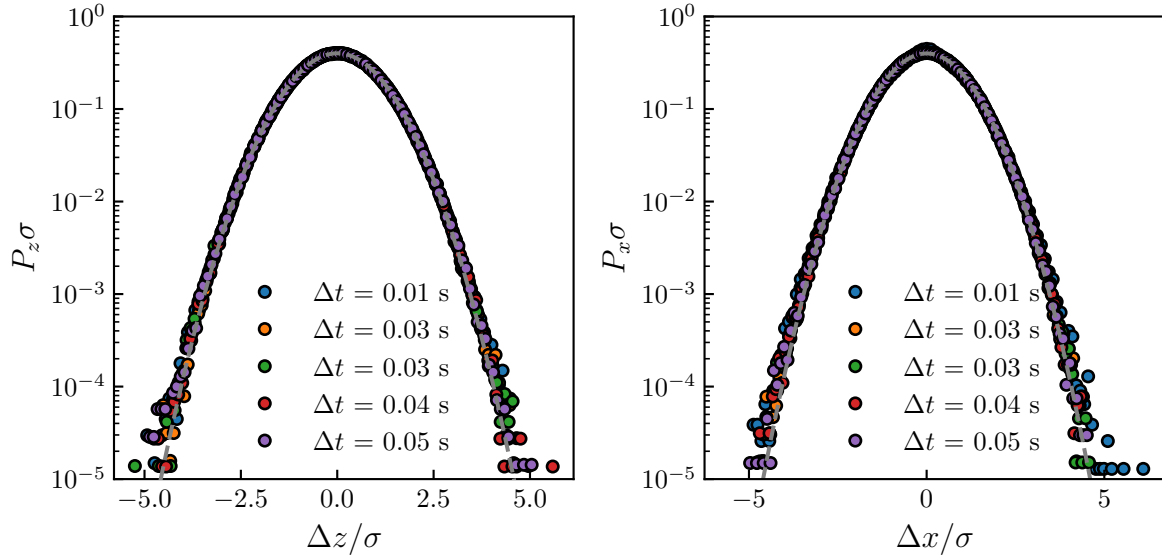


Figure 4.2.4: Normalized probability density functions $P_i \sigma$ of the normalized displacements $\Delta x/\sigma$ and $\Delta z/\sigma$, at short times, with σ^2 the corresponding MSD (see Fig. 4.2.3), for different time increments Δt ranging from 0.01 s to 0.05 s, as indicated with different colors. The gray dashed lines are normalized Gaussian distributions, with zero means and unit variances.

4.3 Direct relative distance measurement using Mie

One of the effects that is not taken into account in the Mie theory presented in the section 2.3 is the presence of the glass slide. Indeed the focal plane, where the holograms are recorded is in the glass slides. Thus, the holograms should be refracted at the glass interface. However, it is not a problem, for they realized fit, indeed, to have faster fit, we use only the few maxima leading to radial distance of $\simeq 5 \mu\text{m}$ for a height $z \simeq 15 \mu\text{m}$, leading to a maximal angle of incidence $\theta = \tan^{-1}(5/15) \simeq 18.5^\circ$. As we are working with small angles, we can suppose that for the first maxima, there is not refracted.

However, the small angle approximation does not hold for higher order maxima, thus as the refraction angle depends on the wall-particle distance, adding it to the Mie theory could lead to a direct measurement of the particle height. Moreover, the Mie fitting would even more robust since a mechanical drift of the sample or the objective would not change the refractive angle of the particle. However, the main difficulty is to be able to have a more stable imaging device to detect with a high accuracy the highest order maxima which are less intense.

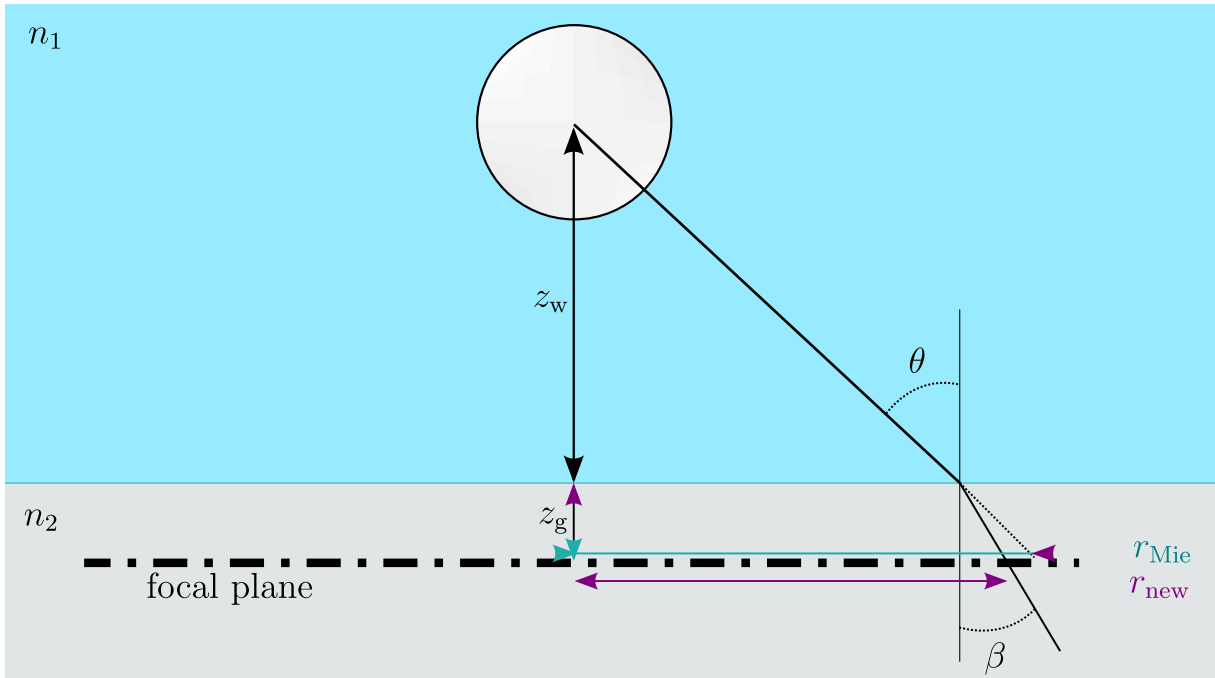


Figure 4.3.1: Scheme of a particle immersed in a fluid of index n_1 above a glass substrate of optical index n_2 . The particle is at a distance z_w above the glass substrate, and the objective focal plane z_g below the interface. Due to the Snell-Descartes's law, light with an incident angle θ_1 is refracted with an angle β .

Let us build a simple model using the Snell-Descartes's law to take into account the refraction at the glass interface, the system is schematized in Fig. 4.3.1. We decompose the height of the particle z in two parts such that:

$$z = z_w + z_g , \quad (4.3.1)$$

where z_g is the interface-focal plane interface and z_w the interface-particle distance, the latter being the distance we want to measure. We want to write the radial intensity of the hologram I , taking into account the refraction, let us write I_{Mie} the Mie solution without the refraction and I_{new} the modified theory. An incident ray coming from the particle with an angle θ is refracted with an angle β , as shown in Fig. 4.3.1. Using trigonometry and the Snell-Descartes's law ($n_1 \sin(\theta) = n_2 \sin(\beta)$), those angles writes:

$$\theta = \tan^{-1} \left(\frac{r_{\text{Mie}}}{z_w + z_g} \right) , \quad (4.3.2)$$

and,

$$\beta = \sin^{-1} \left(\frac{n_1 \sin(\theta)}{n_2} \right) . \quad (4.3.3)$$

Without refraction, the light arrives at the focal plane at a distance r_{Mie} as shown in Fig. 4.3.1, due to the refraction this distance is modified to r_{new} :

$$r_{\text{new}} = r_{\text{Mie}} + z_g (\tan(\beta) - \tan(\theta)) . \quad (4.3.4)$$

Due to the change of optical path, the Mie scattering field (see Eq. (2.3.2)) undergoes a phase difference $\Delta\varphi_w$ in the fluid and $\Delta\varphi_g$ in the glass substrate:

$$\Delta\varphi_w = \frac{2\pi}{\lambda} n_1 z \tan(\theta') , \quad (4.3.5)$$

and,

$$\Delta\varphi_g = \frac{2\pi}{\lambda} n_2 z \tan(\beta') , \quad (4.3.6)$$

where θ' and β' are given by:

$$\theta' = \tan^{-1} \left(\frac{r_{\text{new}}}{z_w + z_g} \right) , \quad (4.3.7)$$

and,

$$\beta' = \sin^{-1} \left(\frac{n_1 \sin(\theta')}{n_2} \right) . \quad (4.3.8)$$

Moreover, a part of the light is reflected onto the surface, thus attenuating the scattering field by a factor $T = (n_1 + n_2)/2n_2$. Finally, taking the phase difference, the corrected scattered field E_s^{new} writes:

$$E_s^{\text{new}} = T E_s \exp(-j(\Delta\varphi_w - \Delta\varphi_g)) , \quad (4.3.9)$$

with the hologram normalized radial intensity given by:

$$\frac{I(r)}{I_0(r)} = \frac{|E_s^{\text{new}}(r) + E_0(r)|}{E_0(r)} \quad (4.3.10)$$

We are currently working on this project with Mathias Perrin, a specialist of the numerical simulation of Mie system. We need to simulation of the exact modification of the holograms when due to the glass interface. The simulation results will then be compared to the model Eq. (4.3.10) to verify if it correctly captures the physics.

4.4 Long time 4th cumulent

In this subsection we consider the cumulent of higher order than 2 (MSD). The 4th order cumulent writes:

$$C_4(\Delta t) = \frac{1}{4!} \left(\langle [x_i(t + \Delta t) - x_i(t)]^4 \rangle_t - 3 \langle [x_i(t + \Delta t) - x_i(t)]^2 \rangle_t^2 \right). \quad (4.4.1)$$

For a Gaussian distributed variable x as Brownian motion in bulk, C_4 is a constant as $\langle \Delta x^2 \rangle_t^2 = \langle x^4 \rangle_t$. Therefore, the literature often overlooks the higher moments as it rarely gives additional informations. However, as it has been shown along this manuscript, confined Brownian motion exhibit non-Gaussian statistical properties as shown in Fig. 3.2.5. Thus, it could be interesting to study the 4th cumulent of confined Brownian particles. We work on this project with David Dean and Arthur Alexandre who are specialized in Brownian theory. They found interesting behavior for the 4th cumulent along parallel displacement to the wall, for which the Langevin equation is given by:

$$dX_t = \sqrt{2D_{\parallel}(z_t)} dB_t \quad (4.4.2)$$

After combining Eqs. (4.4.1) and (4.4.2) and some mathematical manipulation, the 4th order cumulent writes:

$$C_4(\Delta t) = \int_{-L}^L dz \int_{-L}^L dz' D_{\parallel}(z) D_{\parallel}(z') p_0(z') \sum_{\lambda > 0} \psi_{\lambda,R}(z) \psi_{\lambda,L}(z') \left(\frac{\Delta}{\lambda} - \frac{1 - \exp(-\lambda \Delta t)}{\lambda^2}, \right) \quad (4.4.3)$$

where the Forward Fokker Plank has been decomposed on the set of eigenfunctions $\psi_{\lambda,R}$, the right eigenfunctions of the Generator G such that:

$$G\psi_{\lambda,R} = \lambda\psi_{\lambda,R} . \quad (4.4.4)$$

For $\lambda = 0$, we have: $\psi_{0,R} = p_0$ and $\psi_{\lambda,L} = 1$. Using this decomposition, the density of probability p writes:

$$p(z, \Delta t | z') = \sum_{\lambda} e^{-\lambda \Delta t} \psi_{\lambda,R}(z) \psi_{\lambda,L}(z') . \quad (4.4.5)$$

Despite the complicated form of Eq. (4.4.3) it gives nice approximations at short and long times, in the limit $\Delta \rightarrow 0$, we have:

$$\lim_{\Delta t \rightarrow 0} C_4(\Delta t) = \frac{\Delta t^2}{2} (\langle D_{\parallel}^2 \rangle - \langle D_{\parallel} \rangle^2) , \quad (4.4.6)$$

where the averages are done over the equilibrium distribution P_{eq} and thus vary as a function of Δt^2 at a short time. Eq. (4.4.3) can also be approximated, in the limit $\Delta t \rightarrow +\infty$ where we have:

$$\lim_{\Delta t \rightarrow \infty} C_4(\Delta t) = C_4^0 \Delta t - C_4^1 , \quad (4.4.7)$$

Where C_4^0 and C_4^1 are constants that depends on the equilibrium distribution P_{eq} , and could be written as a function of B , ℓ_D , and ℓ_B . Unlike the first and second moment of the parallel displacement (the displacement distribution $P_x(\Delta x)$ and the MSD $\langle \Delta x^2 \rangle_t$ respectively), the 4th cumulant a peculiar regime when the particle reach equilibrium. This result is thus interesting as it gives a new observable of the equilibrium properties on the parallel displacement. If this theory is verified, it could be added to our inference method (see section 3.2) in order to gain precision and robustness.

As we are only interested in the x - and y -axis displacement to show this result, we do not need 3D tracking. Thus, we only need to find the holograms centroid, and therefore use faster algorithms than the Mie framework. To do so we use the Trackpy package  [93] which implements the Crocker–Grier algorithm [94] which permits tracking the centroid of hundreds of colloids quite rapidly. Trajectories thus tracked are shown in Fig. 4.4.1.

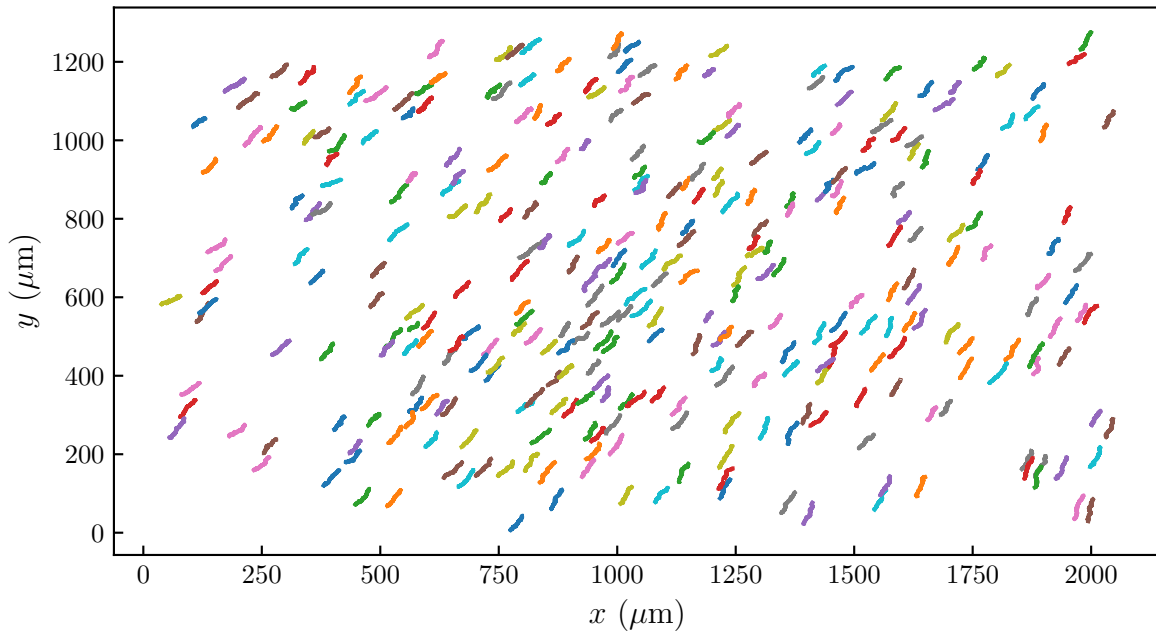


Figure 4.4.1: Trajectory of 300 particles of commercial radius $a = 2.5 \mu\text{m}$. The trajectories are composed of 10000 points with a time step $\tau = 0.05 \text{ s}$.

From the data retrieve, we can compute the 4th cumulent using Eq. (4.4.1) and we do observe a linear regime as shown in Fig. 4.4.2. However, this experiment as only been done once, it is thus preliminary results that encourage continuing in this way.

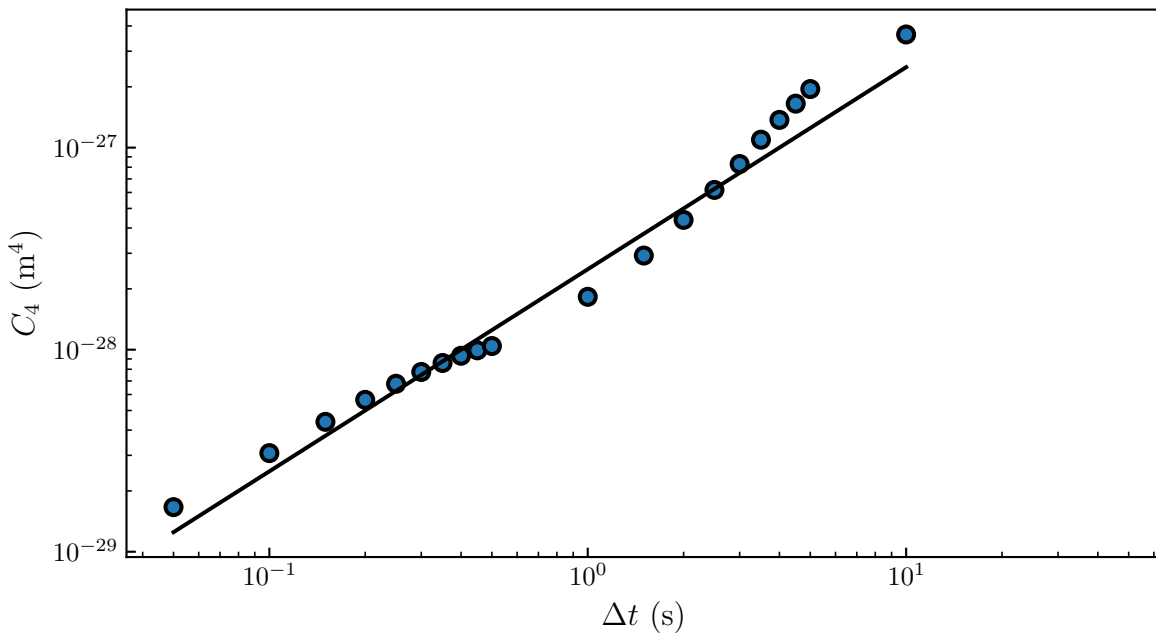


Figure 4.4.2: Bullets corresponds to the experimentally measured 4th cumulent, see Eq. (4.4.2). The plain line is a linear regime indicator. The images are $45 \mu\text{m}$ wide and $50 \mu\text{m}$ tall.

4.5 Sample ageing

While doing the experiment on the soft surfaces, we observed that the image was becoming blurry with time, as a diffusive layer was added in the microscope's optical path. An example is shown in Fig. 4.5.1 where we can see microscope images separated by three hours.

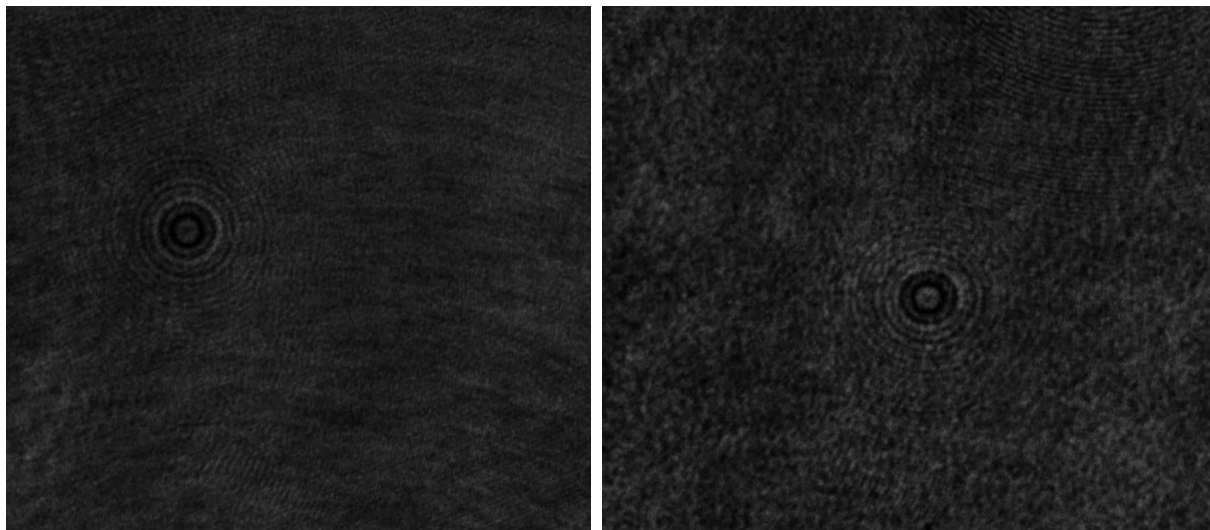


Figure 4.5.1: Image of a particle diffusing above a soft surface ($G = 1.5 \text{ kPa}$). The image on the right has been taken 3 hours after the one on the left. The images are $45 \mu\text{m}$ wide and $50 \mu\text{m}$ tall.

Trying to find the origin of this effect, we focused on the interface between the soft PDMS layer and glass. Doing so, we observe a structure that looks like bubbles, as shown in Fig.4.5.2. We observe that this effect happens faster as the PDMS is softer (lower modulus) and the bubble seems to be also bigger. One of the ideas we have to explain this phenomenon comes from the high gas permeability of PDMS that could lead to a gas accumulation between the PDMS and glass. The origin of this gas would come from the naturally present gas inside the colloid suspension.

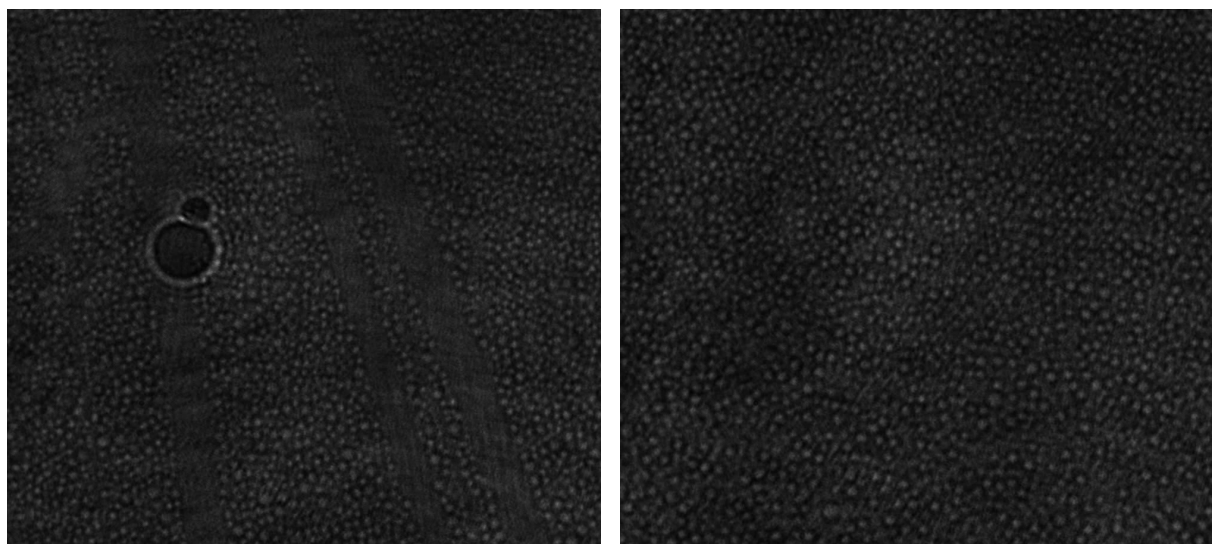


Figure 4.5.2: Image of the glass-PDMS ($G = 1.5 \text{ kPa}$) interface, three hours after that water has been introduced in the sample. The images are $45 \mu\text{m}$ wide and $50 \mu\text{m}$ tall.

5 Conclusion

In this manuscript, we have covered a broad spectrum of the Brownian motion. We started by its history by presenting its first observation in the 19th by Robert Brown and its mathematical description, and numerical simulation. We have then described different techniques that permits tracking of individual microparticles. We mainly focused on the Lorenz-Mie framework since as we used it to study the free confined Brownian motion. We indeed focused on the Lorenz-Mie framzork as it requieres no calibration by measuring the radius and optical index of each tracked particles. We then showed the experimental setup, which is a custom made inverted microscope that we optized over the years to capture Lorenz-Mie holograms. To retrieve the trajectory from the captured holograms we mainly used the tool developped at the Grier's Lab under the name of Pylorenzmie  and a custom version, Wraplorenzmie to automate the tracking across whole movies and simplify the use of MP4 files . An example of the Jupyter notebooks employed for the tracking can be found in appendix ??.

The particles thus tracked and the trajcetories retrieve, we focused on the analyse of the confined Brownian motion. We first detailed how the physics changes starting from the DLVO interactions between the surface and the particles and hindered diffusion. Due to this hindered diffusion, a spurious drift appears while using the overdamped Langevin equation which needs to be taken into account while doing simulations, and later the force measurements.

Once the underlying theory has been explained, we described the experimental results and how the trajcetories are analized. Starting from static observables such as equilibrium distributions to dynamic observables with the Mean Squared Displacements and displacement distribution. In particular, the MSD exhibit a normal distribution at short time, and a equilibrium regime for the movement perpendicular to the wall. As to short time displacement distribution, it shows non-Gaussian properties despite the normal distribution indicated by the MSD.

The statistical properties of a confined particle understood and correctly measured, we then focused on measuring the hindered diffusion. This measure was done using a novel method devellopped by Frishman and Ronceray [70] using information theory to infer the the diffusion onto a basis of function, leading to high accuracy near the surface where there is less data.

All the experimental data, from the equilibrium distribution to the hindered diffusion can all be given by the parameters of the system B , ℓ_D and ℓ_B . We thus built a multi-

fitting method, that permits to infer precisely those parameters by taking into account all the observable at the same time. From this measurement, we measured precisely the equilibrium potential from which we can compute the conservative force which permitted to verify that we correctly measure the force measured though the local drifts.

Starting from the construction of the microscope to numerical analysis, built a multi-scale statistical analysis for the problem of freely diffusing individual colloids near a rigid wall. By combining all the observables, we are able to reach thermal-noise-limited femtoNewton spatial and force resolutions at the nanoscale. This work has finally been published in Physical Review Research and is in appendix ??.

As shown in the last chapter, we are currently using our multi-scale statistical analysis in order to inspect soft lubrication theory applied to Brownian motion. Particularly, if the a Brownian particle can trigger elastohydrodynamic lift which is a non-conservative forces. Also we are working on pushing the limit of our resolution to measure fine effects on high order cumulents to experimentaly verify a theoritical model, that exhibit correlation between the perpendicular and parallel displacement of a free diffusing particle, which can be counterintuitive and has not yet been measured. Finally, we believe that the ability to measure tiny surface forces, locally, and at equilibrium, as well the possible extension of the method to non-conservative forces and out-of-equilibrium settings, opens fascinating perspectives for nanophysics and biophysics.

6 Conclusion en français

Dans ce manuscrit, nous avons couvert un large spectre du mouvement brownien. Nous avons commencé par son histoire en présentant sa première observation au 19ème siècle par Robert Brown, sa description mathématique ainsi que comment le simuler numériquement. Nous avons ensuite décrit les différentes techniques qui permettent de localiser des microparticules individuelles. Nous nous sommes principalement concentrés sur la théorie de Lorenz-Mie puisque nous l'avons utilisé pour étudier expérimentalement le mouvement brownien libre confiné. Nous nous sommes en effet concentrés la théorie de Lorenz-Mie car elle ne nécessite aucune calibration, en mesurant le rayon et l'indice optique de chaque particule localisée. Nous avons ensuite expliqué le dispositif expérimental, qui est un microscope inversé fait sur mesure, que nous avons optimisé au fil des ans pour capturer des hologrammes de Lorenz-Mie. Pour récupérer la trajectoire des hologrammes capturés, nous avons principalement utilisé l'outil développé au laboratoire de Grier sous le nom de Pylorenzmie  et une version personnalisée, Wraplorenzmie pour automatiser la locali-

sation sur des films entiers et simplifier l'utilisation des fichiers MP4 . Un exemple des *Jupyter Notebook* utilisés pour la localisation se trouve en annexe ??.

Les particules ainsi localisées et les trajetories récupérées, nous nous sommes concentrés sur l'analyse du mouvement brownien confiné. Nous avons d'abord détaillé comment la physique change à partir des interactions DLVO entre la surface et les particules, et la diffusion locale. En raison de cette diffusion locale, un *spurious drift* apparaît lors de la résolution de l'équation de Langevin suramortie qui doit être prise en compte lors des simulations, et plus tard lors des mesures de force.

Une fois la théorie sous-jacente expliquée, nous avons décrit les résultats expérimentaux et la manière dont les trajetories sont analysées. En partant des observables statiques comme les distributions d'équilibre jusqu'aux observables dynamiques avec les déplacements quadratiques moyens et la distribution des déplacements. En particulier, les MSD présentent une distribution normale aux temps courts, et un régime d'équilibre pour le mouvement perpendiculaire au mur. Quant à la distribution des déplacements à court terme, elle présente des propriétés non gaussiennes malgré la distribution normale indiquée par les MSD.

Les propriétés statistiques d'une particule confinée étant comprises et correctement mesurées, nous nous sommes ensuite attachés à mesurer la diffusion locale. Cette mesure a été effectuée à l'aide d'une nouvelle méthode développée par Frishman et Ronceray [70] utilisant la théorie de l'information pour inférer la diffusion sur une base de fonction, conduisant à une grande précision près de la surface où il y a moins de données.

Toutes les données expérimentales, de la distribution à l'équilibre à la diffusion locale, peuvent toutes être données par les paramètres du système B , ℓ_D et ℓ_B . Nous avons donc construit une méthode *multi-fitting*, qui permet de déduire précisément ces paramètres en prenant en compte tous les observables en même temps. A partir de cette mesure, nous avons mesuré précisément le potentiel d'équilibre à partir duquel nous pouvons calculer la force conservative qui a permis de vérifier que nous mesurons correctement la force mesurée par les dérives locales.

De la construction du microscope à l'analyse numérique, nous avons construit une analyse statistique multi-échelle pour le problème de colloïdes individuels diffusant librement près d'une paroi rigide. En combinant toutes les observables, nous sommes capables d'atteindre des résolutions spatiales et de force de l'ordre du femtoNewton à l'échelle nanométrique, limitées par le bruit thermique. Ce travail a finalement fait l'objet d'une publication dans le journal *Physical Review Research*, disponible en annexe ??.

Comme indiqué dans le dernier chapitre, nous utilisons actuellement notre analyse statistique multi-échelle pour examiner la théorie de la lubrification douce appliquée au mouvement brownien. En particulier, si une particule brownienne peut déclencher un soulèvement élastohydrodynamique, qui est une force non conservative. Nous travaillons également à pousser la limite de notre résolution pour mesurer les effets fins sur les cumulents d'ordre élevé afin de vérifier expérimentalement un modèle théorique, qui présente une corrélation entre le déplacement perpendiculaire et parallèle d'une particule diffusant librement, ce qui peut être contre-intuitif et n'a pas encore été mesuré. Enfin, nous pensons que la capacité de mesurer de minuscules forces de surface, localement et à l'équilibre, ainsi que l'extension possible de la méthode aux forces non-conservatives et aux situations hors équilibre, ouvre des perspectives fascinantes pour la nanophysique et la biophysique.

References

- [1] B. Robert, “XXVII. a brief account of microscopical observations made in the months of june, july and august 1827, on the particles contained in the pollen of plants; and on the general existence of active molecules in organic and inorganic bodies”, *The Philosophical Magazine* **4**, Taylor & Francis, 161–173 (1828).
- [2] A. Einstein, “Über die von der molekularkinetischen Theorie der Wärme geforderte Bewegung von in ruhenden Flüssigkeiten suspendierten Teilchen”, *Annalen der Physik* **vol. 4, t. 17** (1905).
- [3] S. Peter, “Brownian motion”, **Brownian motion**.
- [4] J. Perrin, “Mouvement brownien et molécules”, *J. Phys. Theor. Appl.* **9**, 5–39 (1910).
- [5] A. Genthon, “The concept of velocity in the history of brownian motion”, *The European Physical Journal H* **45**, 49–105 (2020).
- [6] P. Langevin, “Sur la théorie du mouvement brownien”, *C. R. Acad. Sci. (Paris)* 146, 530–533 **65**, 1079–1081 (1908).
- [7] R. Durrett, *Probability: theory and examples*, 5th ed., Cambridge Series in Statistical and Probabilistic Mathematics (Cambridge University Press, Cambridge, 2019).
- [8] D. Freedman and P. Diaconis, “On the histogram as a density estimator: l₂ theory”, *Zeitschrift für Wahrscheinlichkeitstheorie und Verwandte Gebiete* **57**, 453–476 (1981).
- [9] E. Ampomah, E. Mensah, and A. Gilbert, “Qualitative assessment of compiled, interpreted and hybrid programming languages”, *Communications on Applied Electronics* **7**, 8–13 (2017).
- [10] C. Fabry and A. Pérot, “Théorie et application d’une nouvelle méthode de spectroscopie interferentielle.”, *Ann. Chim. Phys.*, **7** (1899).
- [11] A. Perot and C. Fabry, “On the application of interference phenomena to the solution of various problems of spectroscopy and metrology”, *The Astrophysical Journal* **9**, 87 (1899).
- [12] A. A. Michelson and E. W. Morley, “On the relative motion of the earth and the luminiferous ether”, *American Journal of Science* **s3-34**, Publisher: American Journal of Science Section: Extraterrestrial geology, 333–345 (1887).

- [13] LIGO Scientific Collaboration and Virgo Collaboration et al, “GW151226: observation of gravitational waves from a 22-solar-mass binary black hole coalescence”, Physical Review Letters **116**, in collab. with B. P. Abbott, Publisher: American Physical Society, 241103 (2016).
- [14] A. S. Curtis, “The mechanism of adhesion of cells to glass. a study by interference reflection microscopy”, The Journal of Cell Biology **20**, 199–215 (1964).
- [15] T. J. Filler and E. T. Peuker, “Reflection contrast microscopy (RCM): a forgotten technique?”, The Journal of Pathology **190**, 635–638 (2000).
- [16] P. A. Siver and J. Hinsch, “The use of interference reflection contrast in the examination of diatom valves”, Journal of Phycology **36**, 616–620 (2000).
- [17] I. Weber, “[2] reflection interference contrast microscopy”, in *Methods in enzymology*, Vol. 361, Biophotonics, Part B (Academic Press, Jan. 1, 2003), pp. 34–47.
- [18] L. Limozin and K. Sengupta, “Quantitative reflection interference contrast microscopy (RICM) in soft matter and cell adhesion”, Chemphyschem: A European Journal of Chemical Physics and Physical Chemistry **10**, 2752–2768 (2009).
- [19] F. Nadal, A. Dazzi, F. Argoul, and B. Pouliquen, “Probing the confined dynamics of a spherical colloid close to a surface by combined optical trapping and reflection interference contrast microscopy”, Applied Physics Letters **79**, 3887–3889 (2002).
- [20] J. Raedler and E. Sackmann, “On the measurement of weak repulsive and frictional colloidal forces by reflection interference contrast microscopy”, Langmuir **8**, 848–853 (1992).
- [21] H. S. Davies, D. Débarre, N. El Amri, C. Verdier, R. P. Richter, and L. Bureau, “Elastohydrodynamic lift at a soft wall”, Physical Review Letters **120**, 198001 (2018).
- [22] C. F. Bohren and D. R. Huffman, *Absorption and scattering of light by small particles* (Wiley, Apr. 1998).
- [23] H. J. W. Strutt, “LVIII. on the scattering of light by small particles”, The London, Edinburgh, and Dublin Philosophical Magazine and Journal of Science **41**, Publisher: Taylor & Francis _eprint: <https://doi.org/10.1080/14786447108640507>, 447–454 (1871).
- [24] L. Lorenz, *Lysbevægelsen i og uden for en af plane Lysbølger belyst Kugle*, Google-Books-ID: hnE7QwAACAAJ (1890), 62 pp.

- [25] G. Mie, “Beiträge zur optik trüber medien, speziell kolloidaler metallösungen”, *Annalen der Physik* **330**, eprint: <https://onlinelibrary.wiley.com/doi/pdf/10.1002/andp.19083300302> 377–445 (1908).
- [26] B. Ovryn and S. H. Izen, “Imaging of transparent spheres through a planar interface using a high-numerical-aperture optical microscope”, *JOSA A* **17**, Publisher: Optical Society of America, 1202–1213 (2000).
- [27] S.-H. Lee, Y. Roichman, G.-R. Yi, S.-H. Kim, S.-M. Yang, A. v. Blaaderen, P. v. Oostrum, and D. G. Grier, “Characterizing and tracking single colloidal particles with video holographic microscopy”, *Optics Express* **15**, Publisher: Optical Society of America, 18275–18282 (2007).
- [28] J. Katz and J. Sheng, “Applications of holography in fluid mechanics and particle dynamics”, *Annual Review of Fluid Mechanics* **42**, eprint: <https://doi.org/10.1146/annurev-fluid-121108-145508>, 531–555 (2010).
- [29] P. Gregory, *Bayesian logical data analysis for the physical sciences: a comparative approach with mathematica® support*, Google-Books-ID: idkLAQAAQBAJ (Cambridge University Press, Apr. 14, 2005), 496 pp.
- [30] T. G. Dimiduk and V. N. Manoharan, “Bayesian approach to analyzing holograms of colloidal particles”, *Optics Express* **24**, Publisher: Optical Society of America, 24045–24060 (2016).
- [31] W. J. Lentz, “Generating bessel functions in mie scattering calculations using continued fractions”, *Applied Optics* **15**, Publisher: Optical Society of America, 668–671 (1976).
- [32] J. Fung and V. N. Manoharan, “Holographic measurements of anisotropic three-dimensional diffusion of colloidal clusters”, *Physical Review E* **88**, 020302 (2013).
- [33] A. Wang, T. G. Dimiduk, J. Fung, S. Razavi, I. Kretzschmar, K. Chaudhary, and V. N. Manoharan, “Using the discrete dipole approximation and holographic microscopy to measure rotational dynamics of non-spherical colloidal particles”, *Journal of Quantitative Spectroscopy and Radiative Transfer* **146**, 499–509 (2014).
- [34] R. W. Perry, G. Meng, T. G. Dimiduk, J. Fung, and V. N. Manoharan, “Real-space studies of the structure and dynamics of self-assembled colloidal clusters”, *Faraday Discussions* **159**, Publisher: The Royal Society of Chemistry, 211–234 (2013).

- [35] T. G. Dimiduk, R. W. Perry, J. Fung, and V. N. Manoharan, “Random-subset fitting of digital holograms for fast three-dimensional particle tracking”, *Applied Optics* **53**, G177 (2014).
- [36] A. Yevick, M. Hannel, and D. G. Grier, “Machine-learning approach to holographic particle characterization”, *Optics Express* **22**, 26884 (2014).
- [37] M. D. Hannel, A. Abdulali, M. O’Brien, and D. G. Grier, “Machine-learning techniques for fast and accurate feature localization in holograms of colloidal particles”, *Optics Express* **26**, Publisher: Optical Society of America, 15221–15231 (2018).
- [38] L. E. Altman and D. G. Grier, “CATCH: characterizing and tracking colloids holographically using deep neural networks”, *The Journal of Physical Chemistry B* **124**, Publisher: American Chemical Society, 1602–1610 (2020).
- [39] L. Wilson and R. Zhang, “3d localization of weak scatterers in digital holographic microscopy using rayleigh-sommerfeld back-propagation”, *Optics Express* **20**, 16735 (2012).
- [40] J. W. Goodman, *Introduction to fourier optics*, Google-Books-ID: ow5xs_Rtt9AC (Roberts and Company Publishers, 2005), 520 pp.
- [41] F. C. Cheong, B. J. Krishnatreya, and D. G. Grier, “Strategies for three-dimensional particle tracking with holographic video microscopy”, *Optics Express* **18**, Publisher: Optical Society of America, 13563–13573 (2010).
- [42] G. C. Sherman, “Application of the convolution theorem to rayleigh’s integral formulas”, *JOSA* **57**, Publisher: Optical Society of America, 546–547 (1967).
- [43] U. Schnars and W. P. Jüptner, “Digital recording and reconstruction of holograms in hologram interferometry and shearography”, *Applied Optics* **33**, 4373–4377 (1994).
- [44] T. M. Kreis, “Frequency analysis of digital holography with reconstruction by convolution”, *Optical Engineering* **41**, Publisher: International Society for Optics and Photonics, 1829–1839 (2002).
- [45] X. Zhang, J. Qiu, J. Qiu, J. Qiu, X. Li, X. Li, J. Zhao, J. Zhao, L. Liu, and L. Liu, “Complex refractive indices measurements of polymers in visible and near-infrared bands”, *Applied Optics* **59**, Publisher: Optical Society of America, 2337–2344 (2020).
- [46] D. C. Prieve, “Measurement of colloidal forces with TIRM”, *Advances in Colloid and Interface Science* **82**, 93–125 (1999).

- [47] J. J. Moré, “The levenberg-marquardt algorithm: implementation and theory”, in Numerical analysis, edited by G. A. Watson, Lecture Notes in Mathematics (1978), pp. 105–116.
- [48] J. Perrin, *Les Atomes*, Google-Books-ID: A0ltBQAAQBAJ (CNRS Editions, Nov. 14, 2014), 199 pp.
- [49] J. N. Israelachvili, *Intermolecular and surface forces*, Google-Books-ID: MVbWB-hubrgIC (Academic Press, May 29, 2015), 706 pp.
- [50] G. M. Bell, S. Levine, and L. N. McCartney, “Approximate methods of determining the double-layer free energy of interaction between two charged colloidal spheres”, *Journal of Colloid and Interface Science* **33**, 335–359 (1970).
- [51] S. H. Behrens and D. G. Grier, “The charge of glass and silica surfaces”, *The Journal of Chemical Physics* **115**, 6716–6721 (2001).
- [52] L. P. Faucheux and A. J. Libchaber, “Confined brownian motion”, *Physical Review E* **49**, 5158–5163 (1994).
- [53] H. Brenner, “The slow motion of a sphere through a viscous fluid towards a plane surface”, *Chemical Engineering Science* **16**, 242–251 (1961).
- [54] H. Faxen, “Fredholm integral equations of hydrodynamics of liquids i”, *Ark. Mat., Astron. Fys* **18**, 29–32 (1924).
- [55] E. P. Honig, G. J. Roebersen, and P. H. Wiersema, “Effect of hydrodynamic interaction on the coagulation rate of hydrophobic colloids”, *Journal of Colloid and Interface Science* **36**, 97–109 (1971).
- [56] M. A. Bevan and D. C. Prieve, “Hindered diffusion of colloidal particles very near to a wall: revisited”, *The Journal of Chemical Physics* **113**, Publisher: American Institute of Physics, 1228–1236 (2000).
- [57] G. A. Baker, G. A. B. Jr, P. Graves-Morris, G. Baker (A.), and S. S. Baker, *Pade approximants: encyclopedia of mathematics and it's applications, vol. 59 george a. baker, jr., peter graves-morris*, Google-Books-ID: Vkk4JNLKbLoC (Cambridge University Press, Jan. 26, 1996), 762 pp.
- [58] N. Ikeda and S. Watanabe, *Stochastic differential equations and diffusion processes*, Google-Books-ID: QZbOBQAAQBAJ (Elsevier, June 28, 2014), 572 pp.

- [59] G. Volpe and J. Wehr, “Effective drifts in dynamical systems with multiplicative noise: a review of recent progress”, *Reports on Progress in Physics* **79**, 053901 (2016).
- [60] M. Le Bellac, F. Mortessagne, and G. G. Batrouni, *Equilibrium and non-equilibrium statistical thermodynamics* (Cambridge University Press, Cambridge, 2004).
- [61] P. Del Moral and N. G. Hadjiconstantinou, “An introduction to probabilistic methods with applications”, *ESAIM: Mathematical Modelling and Numerical Analysis* **44**, 805–829 (2010).
- [62] M. Matse, “State-dependent diffusion of brownian particles near a boundary wall”, 84.
- [63] W. Wang, J. S. Guasto, and P. Huang, “Measurement bias in evanescent wave nano-velocimetry due to tracer size variations”, 10.1007/S00348-011-1188-X (2011).
- [64] M. R. Oberholzer, N. J. Wagner, and A. M. Lenhoff, “Grand canonical brownian dynamics simulation of colloidal adsorption”, *The Journal of Chemical Physics* **107**, Publisher: American Institute of Physics, 9157–9167 (1997).
- [65] M. V. Chubynsky and G. W. Slater, “Diffusing diffusivity: a model for anomalous, yet brownian, diffusion”, *Physical Review Letters* **113**, 098302 (2014).
- [66] H. Risken, *Fokker-planck equation: methods of solution and applications*. OCLC: 968506197 (Springer, Place of publication not identified, 2012).
- [67] M. Matse, M. V. Chubynsky, and J. Bechhoefer, “Test of the diffusing-diffusivity mechanism using near-wall colloidal dynamics”, *Physical Review E* **96**, 042604 (2017).
- [68] S. Hapca, J. W. Crawford, and I. M. Young, “Anomalous diffusion of heterogeneous populations characterized by normal diffusion at the individual level”, *Journal of The Royal Society Interface* **6**, 111–122 (2009).
- [69] R. Friedrich, J. Peinke, M. Sahimi, and M. Reza Rahimi Tabar, “Approaching complexity by stochastic methods: from biological systems to turbulence”, *Physics Reports* **506**, 87–162 (2011).
- [70] A. Frishman and P. Ronceray, “Learning force fields from stochastic trajectories”, *Physical Review X* **10**, 021009 (2020).
- [71] M. E. Beheiry, M. Dahan, and J.-B. Masson, “InferenceMAP: mapping of single-molecule dynamics with bayesian inference”, *Nature Methods* **12**, Bandiera_abtest: a Cg_type: Nature Research Journals Number: 7 Primary_atype: Correspondence

- Publisher: Nature Publishing Group Subject_term: Computational biophysics;Image processing;Single-molecule biophysics;Software Subject_term_id: computational-biophysics;image-processing;single-molecule-biophysics;software, 594–595 (2015).
- [72] N. Hoze, D. Nair, E. Hosy, C. Sieben, S. Manley, A. Herrmann, J.-B. Sibarita, D. Choquet, and D. Holcman, “Heterogeneity of AMPA receptor trafficking and molecular interactions revealed by superresolution analysis of live cell imaging”, *Proceedings of the National Academy of Sciences* **109**, Publisher: National Academy of Sciences Section: Biological Sciences, 17052–17057 (2012).
- [73] B. Saintyves, T. Jules, T. Salez, and L. Mahadevan, “Self-sustained lift and low friction via soft lubrication”, *Proceedings of the National Academy of Sciences* **113**, 5847–5849 (2016).
- [74] Y.-H. Dai, “Convergence properties of the BFGS algorithm”, *SIAM Journal on Optimization* **13**, Publisher: Society for Industrial and Applied Mathematics, 693–701 (2002).
- [75] G. Volpe, L. Helden, T. Brettschneider, J. Wehr, and C. Bechinger, “Influence of noise on force measurements”, *Physical Review Letters* **104**, 170602 (2010).
- [76] R. Mannella and P. V. E. McClintock, “Comment on “influence of noise on force measurements””, *Physical Review Letters* **107**, 078901 (2011).
- [77] R. Mannella and P. V. E. McClintock, “Itô versus stratonovich: 30 years later”, *Fluctuation and Noise Letters* **11**, Publisher: World Scientific Publishing Co., 1240010 (2012).
- [78] J. M. Sancho, “Brownian colloidal particles: ito, stratonovich, or a different stochastic interpretation”, *Physical Review E* **84**, Publisher: American Physical Society, 062102 (2011).
- [79] L. Liu, S. Kheifets, V. Ginis, and F. Capasso, “Subfemtonewton force spectroscopy at the thermal limit in liquids”, *Physical Review Letters* **116**, Publisher: American Physical Society, 228001 (2016).
- [80] Y. Amarouchene, M. Mangeat, B. V. Montes, L. Ondic, T. Guérin, D. S. Dean, and Y. Louyer, “Nonequilibrium dynamics induced by scattering forces for optically trapped nanoparticles in strongly inertial regimes”, *Physical Review Letters* **122**, Publisher: American Physical Society, 183901 (2019).

- [81] M. Mangeat, Y. Amarouchene, Y. Louyer, T. Guérin, and D. S. Dean, “Role of non-conservative scattering forces and damping on brownian particles in optical traps”, *Physical Review E* **99**, Publisher: American Physical Society, 052107 (2019).
- [82] C. S. Campbell, “Self-lubrication for long runout landslides”, *The Journal of Geology* **97**, Publisher: The University of Chicago Press, 653–665 (1989).
- [83] B. J. Hamrock, S. R. Schmid, and B. O. Jacobson, *Fundamentals of fluid film lubrication*, 2nd ed. (CRC Press, Boca Raton, Mar. 15, 2004), 728 pp.
- [84] S. Byun, S. Son, D. Amodei, N. Cermak, J. Shaw, J. H. Kang, V. C. Hecht, M. M. Winslow, T. Jacks, P. Mallick, and S. R. Manalis, “Characterizing deformability and surface friction of cancer cells”, *Proceedings of the National Academy of Sciences* **110**, 7580–7585 (2013).
- [85] J. M. Higgins, D. T. Eddington, S. N. Bhatia, and L. Mahadevan, “Sickle cell vasoconstriction and rescue in a microfluidic device”, *Proceedings of the National Academy of Sciences of the United States of America* **104**, 20496–20500 (2007).
- [86] S. I. A. Cohen and L. Mahadevan, “Hydrodynamics of hemostasis in sickle-cell disease”, *Physical Review Letters* **110**, 138104 (2013).
- [87] T. Salez and L. Mahadevan, “Elastohydrodynamics of a sliding, spinning and sedimenting cylinder near a soft wall”, *Journal of Fluid Mechanics* **779**, Publisher: Cambridge University Press, 181–196 (2015).
- [88] J. M. Skotheim and L. Mahadevan, “Soft lubrication”, *Physical Review Letters* **92**, 245509 (2004).
- [89] M. P. Wolf, G. B. Salieb-Beugelaar, and P. Hunziker, “PDMS with designer functionalities—properties, modifications strategies, and applications”, *Progress in Polymer Science* **83**, 97–134 (2018).
- [90] N. Tucher, “Analysis of photonic structures for silicon solar cells”, PhD thesis (Dec. 14, 2016).
- [91] Y. Xia and G. M. Whitesides, “Soft lithography”, *Annual Review of Materials Science* **28**, 153–184 (1998).
- [92] Z. Wang, A. A. Volinsky, and N. D. Gallant, “Crosslinking effect on polydimethylsiloxane elastic modulus measured by custom-built compression instrument”, *Journal of Applied Polymer Science* **131**, n/a–n/a (2014).

- [93] D. B. Allan, T. Caswell, N. C. Keim, C. M. van der Wel, and R. W. Verweij, *Soft-matter/trackpy: trackpy v0.5.0*, Apr. 13, 2021.
- [94] J. C. Crocker and D. G. Grier, “Methods of digital video microscopy for colloidal studies”, *Journal of Colloid and Interface Science* **179**, 298–310 (1996).